THE UNIVERSITY OF CALGARY

Automatic Control of an Aircraft Employing Outboard Horizontal Stabilizers

by

Jason Mukherjee

A DISSERTATION

SUBMITTED TO THE FACULTY OF GRADUATE STUDIES

IN PARTIAL FULFILLMENT OF THE REQUIREMENTS FOR THE

DEGREE OF DOCTOR OF PHILOSOPHY

DEPARTMENT OF MECHANICAL AND MANUFACTURING ENGINEERING

CALGARY, ALBERTA

March, 2000

Abstract

This dissertation concerns the study of radio-operated control of an aircraft using fixed gain and adaptive controllers. The real-time feedback control system is developed to enhance the flying qualities of an experimental model aircraft. The non-conventional flight dynamics of the Outboard Horizontal Stabilizer (OHS) aircraft cause significant differences in the piloting of the aircraft. The control system was added to augment stability as well as to adjust the flight characteristics so that the OHS aircraft handles similar to a conventional aircraft.

The control system design process, as applied to recent innovations in aircraft design, is followed. The Outboard Horizontal Stabilizer concept is a non-conventional aircraft, designed to take advantage of the normally wasted energy developed by the wing tip vortices.

The research is based on a remotely-controlled OHS aircraft fitted with various sensors and telemetry as part of a real time feedback control system. Fixed gain Linear Quadratic controllers are first applied to the aircraft and result in a dramatic increase in performance at a nominal operating condition. Non-linearities in the OHS aircraft behavior and a wide operating range demanded the development of a variable gain adaptive controller utilizing a parameter estimation scheme to model the plant. The adaptive LQR gain-scheduled controller that emerged gave good performance over a wide flight envelope.

Dedication

To my mother and father for their continued support and encouragement

Acknowledgments

I would like to acknowledge the following people for contributing in some way to the completion of this work: supervisor Dr. Jeff Pieper, fellow graduate students: Shane Edmonds, Blaine Shepit, Willie Pitstra P.Eng, Eric Clavelle, Dr. Michael Trentini, Technicians: Mike Johnson, David Genge, Arthur Mohrley, Ben Sanders, Christian Bagg, Greg East, Pilots: Peter Thannhauser, Scott Rollefstad, other professors: Dr. John Kentfield, Dr. Rod Fauvel, electronics expertise: Dick Smit P.Eng and Steve Brown P.Eng.

Table of Contents

List of Tables

List of Figures

List of Symbols

A_f	Frontal area
A, B, C, D	Continuous time state space system matrices
a	Slope of lift coefficient curve
a_n, b_n	Polynomial coefficients
AR	Aspect ratio
C_D	Drag coefficient
C_L	Lift coefficient
c	chord
D	Drag
e	Oswald efficiency factor
g	Acceleration due to gravity
$\bar{h}$	Nominal altitude
H_2, H_∞	H two control, H infinity control
I	Measured moment of inertia
i	angle of incidence
J	Cost function
K	Controller gain
L	Kalman filter gain, lift
l	C of G to tail center of pressure distance
M_{ac}, M_{cg}	Pitching moment about aerodynamic center and c of g
Q	State weighting matrix
q	dynamic pressure, discrete time shift operator
R	Control weighting matrix
S	Wing span, planform area
t	(subscript) tail
u	Control input
V	Velocity
w	(subscript) wing
x	State vector
y	Output vector
α	Angle of attack
ε	Upwash angle
$\theta, \dot{\theta}$	Pitch, Pitch rate
ρ	Air Density
ω_d	Damped natural Frequency
Γ, Φ	Discrete time system matrices

List of Abbreviations

A/D	Analog to Digital
cc	cubic centimeter
C of G	Center of Gravity
D/A	Digital to Analog
DAQ	Data Acquisition
DC	Direct Current
IC	Integrated Circuit
IFPC	Integrated Flight & Propulsion Control
LSB	Least Significant Bit
LQR	Linear Quadratic Regulator
LQOC	Linear Quadratic Optimal Control
MSB	Most Significant Bit
MOSFET	Metal oxide semiconductor field effect transistor
NASA	National Aerospace Agency
OHS	Outboard Horizontal Stabilizer
PD	Proportional plus Derivative
PWM	Pulse Width Modulation
RAM	Random Access Memory
RC	Remote Controlled
RF	Radio Frequency
RLS	Recursive Least Squares
ROM	Read Only Memory
RPV	Remotely Piloted Vehicle
SAE	Society of Automotive Engineers
SISO	Single-Input, Single-Output
STOVL	Short Take-Off Vertical Landing
UAV	Unmanned Air Vehicle
VAAC	Vectored thrust Advanced Aircraft Control

Chapter 1
Introduction

Fly-by-wire systems are becoming more and more common in the aircraft industry. Military jet aircraft initially employed mechanical actuators and later this new form of control to enhance flight capabilities. Most fighter aircraft are curently being designed unstable and with fast dynamics so that they were uncontrollable by a human pilot requiring the use of a computer control system. The commercial airline industry recently joined this technology by introducing fly-by-wire systems in their newer aircraft. These systems allow the flight computer to assume some of the normal responsibilities of the pilot. Also, the advance of autonomous aircraft for use as high altitude environmental research platforms and for aerial surveillance urge the continued study of aircraft control systems.

In 1995, control systems research began on a remote controlled (RC) model airplane at the University of Calgary to study the use of a tele-operated system to improve flying qualities. In order to carry out these various control system experiments, the aircraft system needed to be fitted with various inertial and aerodynamic sensors and electronics. To measure and record the sensor signals, a radio link was required between the aircraft sensors and the ground based station. This telemetry configuration allowed for ground based monitoring during the flight experiments as well as real-time feedback control.

An innovative aircraft configuration, the Outboard Horizontal Stabilizer (OHS) airplane was developed in the early 1990's at the University of Calgary [18]. The unique design incorporates twin bifurcated tails located downstream and outboard of each wing tip. The positioning of the tails in the upwash of the wing tip vortices results in efficient lifting surfaces. The increased Lift/Drag ratio of the OHS airplane reduces the airspeed and thrust required relative to an equivalent (gross weight) conventional design [19]. As a result, an OHS research aircraft will allow longer and higher flights, and an OHS commuter airplane will operate with higher fuel efficiency [20].

1.1 Motivation

Microprocessors and Control systems are an integral part in most recently and newly developed machines. Aircraft control is required to achieve closed loop stability of unstable and marginally stable aircraft or improve the performance, or maneuverability of fighter aircraft. Flight controllers also reduce the work load and control complexity on the pilot, that is, they adjust the flight characteristics of a complex or hard to fly aircraft to behave like a simpler easy to fly aircraft.

The OHS aircraft configuration has great potential in numerous aircraft applications, including its present development for high altitude research platforms, for atmospheric studies. In order to advance and aid the future development of this aircraft, it is necessary to conduct modeling, dynamic analysis, and control system work on this particular configuration.

Telemetry is a major component in control systems. The telemetry system conveys flight data to the computer controller and closes the feedback loop. Design, and implementation of the telemetry system and accompanying electronics was a major development task which resulted in a fully operational real-time feedback control system.

The non-linear dynamics associated with the OHS aircraft design promotes the development of a variable gain controller structure. The sensitivity of the aircraft pitching moment to changes in airspeed demands the adjustability in control gains. The adaptive gain scheduled controller, developed in this work was the result of the need for a self adjusting control scheme capable of providing enhanced flying characteristics over a broad range of the flight envelope.

The non-conventional aspects of the OHS aircraft alters the handling of the aircraft with respect to a conventional design. A flight controller could transform these handling qualities to conform with the control attributes of a conventional aircraft.

1.2 Control System Design

There are several steps in the control system design process. Designing control systems is somewhat of an art; A "feel" for what is going on from past experience usually results in a more eloquent solution. Note that some steps involve several iterations or trial and error to complete. In some cases, one must return to the first step and redefine the problem if a solution is not feasible with the current problem statement.

The first step is to define the problem and control objectives. In this case, there is a non-conventional model aircraft with unknown flight characteristics. The problem is to

design a control system to ensure good flying qualities within the entire flight envelope: take off, climb out, cruise, slow and high speed flight maneuvers, and landing. Also, what kind of sensors and actuators are available and how do they fit into the control scheme?

The next step is to model the plant. There are several methods in use to model physical systems such as analytical modelling, and parameter estimation. Analytical models are developed from physical laws including Newton's laws applied to force and moment systems, Coulomb's law for electromagnetic systems, or Bernoulli's equations in fluid flow systems, etc. Parameter estimation is a modelling technique requiring experimental data from the system. The plant is stimulated with an input signal while the resulting output signal is measured. The plant model is generated by fitting the input and output data to a desired function and then solving for the coefficients using an error minimizing technique.

Once the system is modelled, the performance specifications must be set. The response times, disturbance rejection, bandwidth and robustness are defined.

Following the performance specifications step, the type of controller must be chosen. There are a number of control strategies available having particular goals and purposes. The control types range from simple proportional feedback, to the more complex H_∞ control; fixed gain controllers to variable gain adaptive controllers. The problem is to choose a suitable control scheme to meet the control objectives. This is one of the most difficult steps in the control system design process and usually involves a trial and error methodology. Once the controller type is defined, a controller will be designed to meet the performance specifications.

The plant model and controller are then combined and typically simulated on a computer. This step helps to validate both the plant model and the controller. The simulation is performed to see if the control objectives are met; if not a new controller, model or even a new control objective may have to be formulated. If the simulation is successful, one can implement the controller on the physical system.

The last step in the control design process is the implementation of the controller on the physical plant. The controller and plant are tested to verify that the control objective is achievable. The process of implementation is not necessarily the final step in the control system design process. If the control objectives are not met, one may need to go back to a previous step and make some adjustments.

1.3 OHS Aircraft

The OHS configuration originated at the University of Calgary by Kentfield [18]. Continued development has been carried out by the author and colleagues at the University of Calgary as part of the SAE Heavy Lift Competition [37]. The OHS configuration is receiving attention by others in the field of aeronautics. Recently, Scaled Composites [44], in a joint effort with NASA, started developing a high altitude unmanned autonomous vehicle (UAV) utilizing the innovative OHS aircraft configuration. However, due to budget cuts in NASA, the project has been shelved.

The RC aircraft, shown in Figure 1.1, was used as the control system platform for this research. It was originally designed and built by the author and colleague W.C. Pitstra as the University of Calgary entry in the 1995 SAE Heavy Lift competition [37].

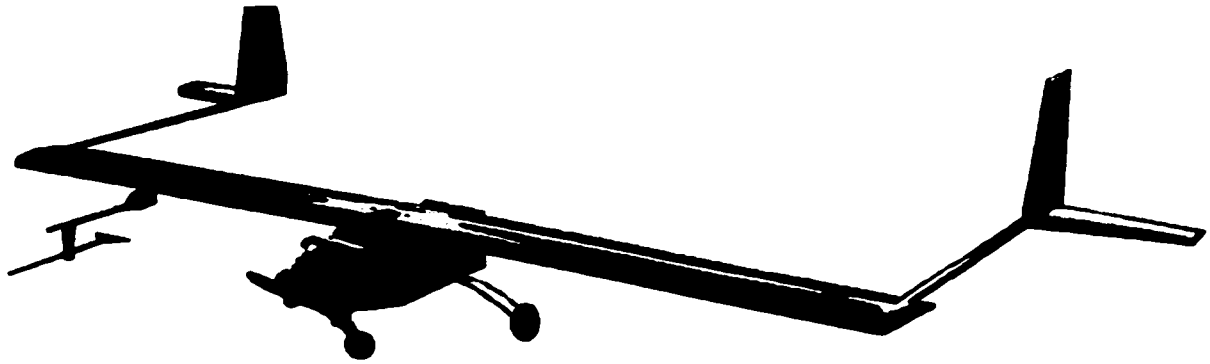

Figure 1.1 OHS aircraft

The experimental flying model has a wingspan of 2.34 m and the length from nose to tail is 1.27 m. The total mass of the aircraft, including the telemetry package and fuel is 6.1 kg. The model airplane cruises at a velocity of 11 m/s and the experiments were conducted at a nominal operating altitude of roughly 40 m above ground.

The lift/drag ratio of the OHS aircraft is larger than a conventional aircraft because the tail surfaces are positioned in the upward flow from the wing tip vortices. The horizontal tail surfaces are able to generate lift with low to negative angles of incidence, while the vertical tail surfaces, because of their position in the wing tip vortices, are effectively drag free [18]. Theoretical analysis along with wind tunnel tests show an increase in lift/drag by up to 30 % [19].

An analytical study of the aerodynamic and gravitational structural loadings was carried out by Kentfield [21]. At first glance, the torsional and bending stresses would appear to be much higher in the OHS configuration than in a conventional aircraft. However, a comparison of the OHS design and a conventional aircraft of equal gross weight results in

lower wing root bending and torsional stresses and slightly higher wing tip torsional loading in flight for the OHS aircraft. Note that the conventional aircraft of equal gross weight has an increased wing planform area of 18 % to compensate for the negative lifting force applied by a conventional tail [21].

1.4 Physical System Overview

The physical system composed of the RC aircraft and onboard electronics, data acquisition (DAQ) system and laptop computer, and flight control transmitter was designed to give real-time feedback control with two controlled inputs and up to five measured outputs. The sampling frequency is hardware limited to 25 Hz. The control inputs were elevator to control the longitudinal dynamics and aileron to control roll. The throttle was found to be ineffective as a control input due to low gain in every axis except forward velocity. The main concern in this dissertation is longitudinal motion but the aileron control provides a wing leveling effect eliminating any stick inputs from the pilot during execution of the test maneuvers.

There are several aerodynamic and inertial sensors onboard the aircraft to measure the outputs: a downwind pivoted vane measures angle of attack, an anemometer measures the airspeed, a multi-axis solid state angular rate sensor gives pitch rate and roll rate and respectively pitch and roll after integrating the signals, and a steady state accelerometer gives vertical displacement after a double integration on the output signal. The accelerometer was used in place of a conventional pressure type altimeter to achieve greater resolution. The measurement signals are relayed to the ground via a telemetry transmitter to a ground

based receiver and DAQ. The data is then transferred to the control computer where it is processed. The feedback data is used in the controller resulting in the two control signals of elevator and aileron. These control signals are sent to the flight control transmitter via the DAQ system. The inputs are then sent to the aircraft receiver and subsequently to the control surface servo motors completing the closed loop control system.

1.5 Contributions

This dissertation provides a method for designing and implementing various controller strategies for a remotely controlled OHS aircraft. Specifically the main contributions are:

- Introduced and conducted an experimental study on a non-conventional aircraft control system design, specifically the OHS design of Kentfield [18] resulting in an aircraft with a high lift/drag ratio and unusual flight dynamics
- Developed and implemented a telemetry, data acquisition and control system for the OHS model aircraft using standard radio-controlled model aircraft equipment modified to provide the necessary signals
- Developed an analytical and an experimental model to represent the unusual longitudinal dynamics of the OHS aircraft using a first principles approach as well as a parameter estimation method

- Conducted theoretical and experimental research using Proportional, Proportional plus Derivative, and LQR controllers to study the effects of fixed gain controllers on the OHS aircraft
- Developed an adaptive gain-scheduled controller for use on the OHS aircraft to accommodate the variation in dynamics with airspeed

1.6 Organization of Dissertation

The organization of the ten chapters of this dissertation follows the sequence of experimental development.

Explained in **Chapter Two** is the background and motivation for the use of aircraft control systems and illustrates some applications.

Described in **Chapter Three** are the apparatus and control hardware and software used for the experiments.

Presented in **Chapter Four** is a method for analytically modelling the aircraft. A first principles analysis is discussed resulting in a fifth order linear state space model.

Introduced in **Chapter Five** is simple feedback control. An outline of the control theory followed by computer simulations and experimental results.

Described in **Chapter Six** is the application of Linear Quadratic control to the OHS aircraft. The controller is designed, simulated and then implemented on the OHS aircraft.

Presented in **Chapter Seven** is the concept of optimal output feedback. The elimination of certain less critical states can save on computing time and complexity.

Explained in **Chapter Eight** is a second method for modelling the dynamics of the OHS aircraft. This process uses the Recursive Least Squares (RLS) parameter estimation scheme. Using input and output data from the experimental model, a best fit function can be calculated and used as the basis for a numerical model.

Developed in **Chapter Nine** is an adaptive controller based on the RLS models determined in Chapter 8. Non-linearities in the OHS aircraft force the requirement for a variable gain controller with changes in airspeed. An adaptive LQR gain scheduled controller was developed to accommodate this need.

Contained in **Chapter Ten** is a summary of the main results and some direction for future work.

Chapter 2
Literature Review

2.1 Introduction

The following is a brief description of prior work in the field of aircraft control. This dissertation covers a broad range of control issues, including various modelling techniques, and several control schemes. Also, the issues of remotely piloted and fly-by-wire aircraft are discussed. The literature review will cover the various control topics as applied to remotely piloted vehicles (RPV).

2.2 Modelling

Aircraft modelling has been around almost since the beginning of the 20th century with the invention of the aircraft. The focus of this section will start a little later, closer to the time of the application of control systems to aircraft.

In 1968, **Dommasch et al** [9] developed a generalized numerical model of an airplane based on first principles. The analytical model is a set of differential equations of motion describing the longitudinal dynamics, as well as, the long and short period modes of an aircraft.

Several analytical methods used in the mathematical modeling for airplane control system design are described by **Roger** [43]. A set of state equations was presented in-

cluding lifting surface aerodynamics. Also, a three-dimensional turbulence model was studied.

The research into underwater RPVs runs parallel to the aerial versions. In 1990, **Hopkin et al** [16] developed a non-linear model of a simplified two-dimensional underwater towed vehicle. Wind tunnel tests were used to verify aerodynamic coefficients and to examine non-linear body lift and downwash effects. A Linear Quadratic controller was then developed to provide the desired bottom following and altitude control for the vehicle.

Wigdorowitz [51] in 1992 developed a method for determining the validity of linearizing a non-linear model for the purpose of linear controller design. The method was successfully applied to a dynamic model of a F4-J aircraft and determines when linearization is an acceptable qualitative approximation to the dynamic behavior of the non-linear model.

In 1992 **Stevens & Lewis** [47] described the flight dynamics of an F-16 aircraft from the equations of motion. A four input, twelfth order non-linear state space model is derived.

The references from above show a number of methods for the modeling of aircraft dynamics. In particular, the method employed by Dommasch[9] is used as the basis for the analytical modeling in this dissertation.

2.3 RPV and Fly-By-Wire Systems

The increasing speed and performance of microcomputers has aided the development of RPV and fly-by-wire systems. This is an ever increasing field of research in both the

civilian environmental and transportation areas as well as various military applications. The cost savings and safety issues associated with unmanned vehicles is of prime concern.

In 1980, **Ambegaonkar & Ellis** [2] described the application of an Intel 8085 Microprocessor controlling a Mini-RPV. The microprocessor featured preprogrammed flight control, programmable gain setting, and software implementation of all functions.

The use of a remotely-piloted model aircraft for aerial photography in environmental applications was investigated in 1983 by **Tomlins** [48]. The proposed model would be equipped with automatic flight controllers, digitally encoded radio signals for secure aircraft command, and a black and white video camera for real-time imagery.

Hill [15] in 1984 describes the use of RPVs in weather research. The RPVs were flown close to thunderstorms with onboard sensing systems to measure the existing potential gradients and apply them to the flight controller.

In 1986, **Xie & Liu** [52] described the application of the D-4 RPV to aerophotogrammetry, aerogeophysical prospecting, and aerial observation. A high degree of precision is required in maintaining the flight attitude to ensure the camera is sufficiently vertical to the ground. Also, the flight path involves a set of equidistant parallel lines, in the horizontal plane, adding to the control problem.

The pitch axis control system of the QF-4 full scale aircraft target is discussed by **Hartley** [14] in 1986. The controller allows the remote operator to pilot the vehicle in both interactive and automatic modes. The interactive all-attitude pitch rate controller adjusts the damping ratio to meet the appropriate military specifications.

Vandersteen [49] in 1986 discusses the avionics for the Lockheed RPV aimed at reconnaissance and surveillance missions. The Lockheed adaptive modular payload system uses a standard two-axis gimbal platform for which many forms of imaging sensors can be installed.

In 1996, **Ashely** [4] describes the fleet of remotely controlled aerial reconnaissance planes. The Unmanned Air Vehicles (UAVs) carry compact radar systems which can distinguish foot-long objects through thick cloud cover. Neither traditional aircraft nor orbital spy satellites could perform the tasks of the prop-driven UAVs.

The unifying feature of these works is their drive towards an RPV that is capable of high precision performance, at a reduced cost to the user. In this dissertation, the objective will be to extend these results. The proposed control algorithm, when applied to the OHS aircraft, yields superior results in both stability augmentation and adjusting flight characteristics to that of a conventional aircraft design.

2.4 Aircraft Control

The study of aircraft control systems is a very broad field of research. Military aircraft were the first to use closed loop control for stability augmentation and for the improvement in flight performance. As the technology and science of controls became well known, it propagated to the commercial and civilian aircraft industries where it is still in an infancy period.

In 1975, **Larsen** [24] describes the development of the RPV technology with respect to the XQM-103, an extensively modified model 147G drone. Quantitative control system

flight test experiments involving vehicle improvements, remote piloting techniques and applications were studied.

Montoya & Jai [34], in 1979 study the microcomputer-based, real-time closed loop control system as applied to a scale model aircraft. The controller is used for stability augmentation for the research of stall/spin characteristics of high performance aircraft.

The use of an LQR controller in conjunction with an incremental gradient procedure for an RPV was used by **Dunn** [11] in 1980. The incremental gradient technique reduces the full-state feedback required by the LQR controller to a realizable design.

In 1988, **Mudge & Patton** [36] describe the design of a sliding mode controller based on the equations of motion of an RPV. The linear and non-linear model responses were compared when subjected to the same variable structure control design.

A Kalman filter for tracking translational and angular position, velocity and acceleration of a maneuvering aircraft using remote sensor data was described in 1992 by **Mook & Shyu** [35]. A 16 state Kalman filter is designed giving not only the states but also the control variables consisting of thrust and control surface deflections. In the same year, **Frangos & Yavin** [13] proposed a synthesis methodology for automating the design of linear optimal controllers. A de-coupled command tracking multivariable Proportional plus Integral control structure was employed. The controller design procedure was applied to the design of a de-coupled lateral control system for an RPV.

In 1995, **Linehan et al** [27] discuss the design and development work on multivariable control strategies on the RPV named the Raven 2. This RPV is a short range aircraft used for tactical military surveillance. In the following year **Linehan et al** [28] address the

problem of accurately tracking a non-zero reference input in the context of multivariable flight control. In order to position the aircraft accurately in time and space during specific autopilot maneuvers, a zero steady state error is required. The optimal dyadic pole placement algorithm plus an LQR controller achieves robust performance and zero steady state error.

The results of the application of an H_∞ loop sharing controller to the VAAC (Vectored Thrust Advanced Aircraft Control) Harrier STOVL (Short Take Off Vertical Landing) aircraft was presented by **Postlethwaite & Bates** [41] in 1998. The suitability of the IFPC (Integrated Flight Propulsion Control) design was considered.

With such a broad number of proven control algorithms available, an objective of this dissertation is to apply the results of the above to the OHS aircraft as appropriate. In particular, since the OHS aircraft design is still in its infancy, it seems appropriate to begin with the application of classical feedback and an LQR strategy, and the work of [11] provides an appropriate benchmark for this task.

2.5 Parameter Estimation

Aircraft are becoming more and more complex making it difficult to model the aircraft analytically. Parameter estimation allows for a mathematical model to be developed with the aid of experimental input and output data from the physical system. The desired model may be obtained without the in depth analytical study of the sometimes uncertain physics in the system.

In 1981, **Coleman et al** [7] study the mini-RPV for a wide range of military payload operations. A control system was developed which relied on the identification of the aerodynamic derivatives in the three axes using rate sensor measurements and lateral yaw acceleration.

Lin & Wen [26] in 1989 study a state estimation algorithm for flight measurement systems as applied to RPV telemetry and control. The system transmits real-time measurement data from the aircraft to the ground.

A framework for the derivation of a Laplace representation of an airframe based on raw aerodynamic data from both wind tunnel testing and actual flight tests was presented in 1995 by **Redling** [42]. The process was successfully carried out on the C-141B and A-4D aircraft at Allied Signal Aerospace Guidance and Control Systems.

The OHS aircraft is an inherently complicated system, making an accurate analytic model quite difficult to obtain. Futher, the success of the proposed control law is often in direct proportion to the accuracy of the model. Thus, the need for a system-specific modelling technique, such as parameter estimation, becomes apparent. The aforementioned works provide an excellent groundwork for this powerful technique, as well as outlining the necessity of parameter estimation.

2.6 Adaptive and Autonomous Control

Combining aircraft control and parameter estimation is one method of obtaining adaptive control. In this case, the controller adjusts itself to compensate for varying flight conditions and situations. Taken one step further, an autonomous aircraft controller no

longer requires a pilot, but performs the prescribed mission without the aid of human intervention.

In 1984, **Mizell** [33] discusses the hardware and software requirements for a fully autonomous aerial vehicle for military applications. The concepts of preparation for the mission, perception of the surroundings, and reaction to the perception of the situation are studied.

The flight control with nonlinear parameter correction based on a model reference adaptive structure for cases with misspecified system dynamics is studied by **Krutova & Rutkovskii** [22] in 1992.

A gain scheduled controller design for a missile longitudinal autopilot was presented in 1993 by **Shamma & Cloutier** [45]. The missile dynamics were modelled as a quasi-linear parameter varying form via a state transformation. A robust controller using $\mu - synthesis$ was designed to give angle-of-attack control using fin deflections.

Neidhoefer & Krishnakumar [38] discuss a project focussing on the design, implementation, and verification of concepts in immunized neurocontrol as applied to a remotely piloted model aircraft in 1994. The aircraft is trained off-line based on collected piloted data. Closed loop control is accomplished with a PC based controller.

In 1996, **Amato & Ambrosino** [1] design a flight control system for the tracking of a parabolic trajectory producing a micro-gravity environment. The combination of feedforward control guaranteeing good tracking and gain-scheduled output feedback to minimize the steady state error were employed. A simulation was carried out for a remotely piloted vehicle.

In this thesis, the above works are used as a springboard to achieve a new variation on an adaptive, gain scheduled controller. In the spirit of [22] and [45], a controller is designed that incorporates both parameter estimation and LQR control. The result is an adaptive LQR gain scheduled controller that constitutes a precursor to autonomous flight for an OHS aircraft.

2.7 Summary

The prior work in the flight control systems field as applied to remotely piloted vehicles is discussed in this chapter. Areas of interest include: modelling, remotely piloted vehicles, various control structures, parameter estimation, and adaptive and autonomous control. These aspects of aircraft control are discussed further in this dissertation including a discussion of design, simulation and experimental analysis. Separate components are combined into an innovative structure as applied to a unique aircraft design. An adaptive controller utilizing parameter estimation, and LQR control are developed around the OHS model aircraft in an attempt to improve the flying qualities in a major portion of the flight envelope.

Chapter 3
Aircraft and Instrumentation

3.1 Introduction

The process of instrumenting a radio controlled model aircraft has a number of difficulties such as radio interference, sensor compatibility and data acquisition issues. These problems as well as the steps taken to resolve the problems are examined.

Describe in this chapter are all the necessary components of the control system starting with the aircraft itself. The aircraft is an unconventional design adding to the complexity of the instrumentation. After a description of the aircraft and the overall control system, each component is examined in detail starting with the aircraft telemetry system, continuing on to data acquisition, and ending with how the pilot controls the aircraft.

3.2 System Overview

There are three major components in the closed loop real time feedback control system: the OHS remote controlled aircraft, the pilot control transmitter, and the computer controller. A schematic diagram of the physical components is shown in Figure 3.1. The dashed lines denote radio links, described in Sections 3.2.7 and 3.2.10, while the solid lines indicate hard wire connections consisting of both analog voltage signals as well as digital streams of data.

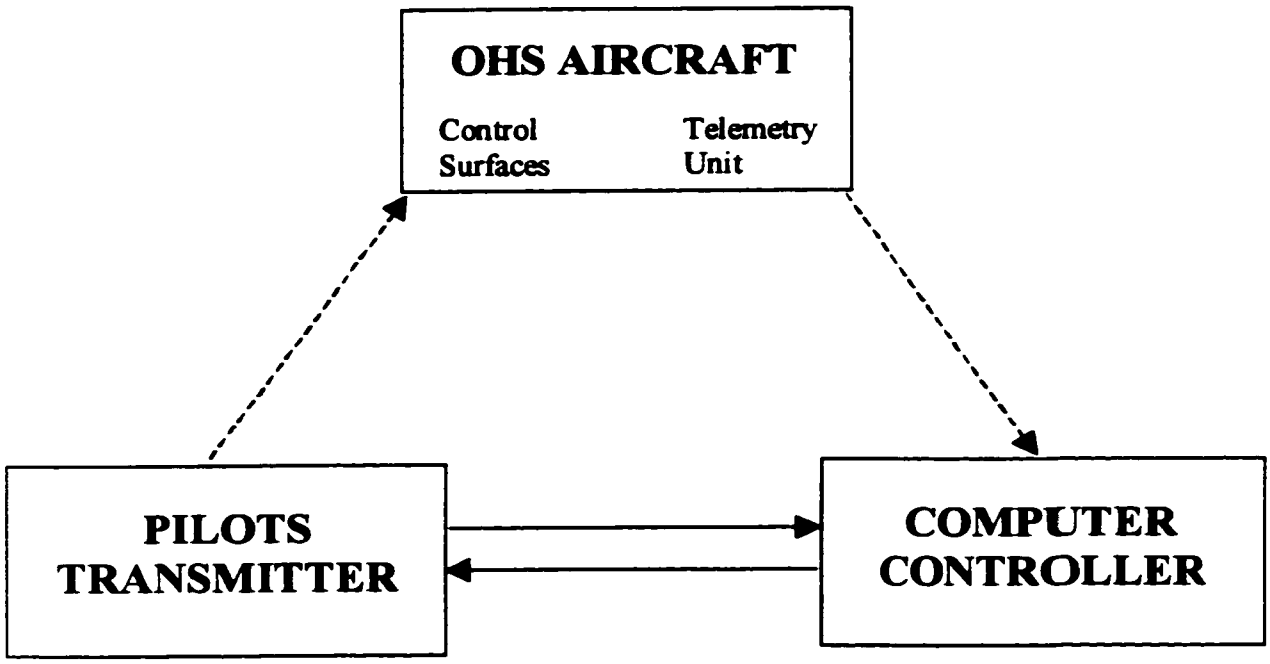

Figure 3.1 Control System Schematic

Alternatively, a computer processor and a recording device could have been installed directly onboard the aircraft eliminating the need for a downward telemetry link. The computer controller and data storage system would be confined to the aircraft, and the flight data could then be analyzed post flight. However, the ability to monitor the experiments from the ground and make changes, (i.e. control gain adjustments) during the flights seem to be more advantageous for research purposes.

3.2.1 Aircraft Construction

The OHS model aircraft is constructed of various materials in an attempt to optimize the structure for strength, weight, and ease of assembly, as an entry into the 1995 SAE aero

design competition. The materials include: balsa wood, spruce, carbon fiber, fiberglass, aluminum, steel, styrofoam and a heat shrink mylar film for the covering.

The fuselage is built up from a balsa wood frame and sheeted with 0.8 *mm* balsa. The entire structure is then covered in fiberglass cloth with specific reinforcements at the wing and landing gear attachment points. The K&B 10 *cc* two stroke engine is attached to the carbon fiber firewall with rubber engine mounts. The aluminum cantilevered main landing gear is also attached to a carbon fiber block mounted within the fuselage. The nose gear is a 4.8 *mm* diameter spring steel rod affixed to the firewall. Air filled rubber tires were used for the experiments to accommodate grass and rough surface runways.

The wing is the most intricate component of the OHS aircraft. The shape is critical in providing lift and the least amount of drag as possible. The high lift airfoil section is shown in Figure 3.2. A Gurney flap was also applied to the trailing edge of the wing on

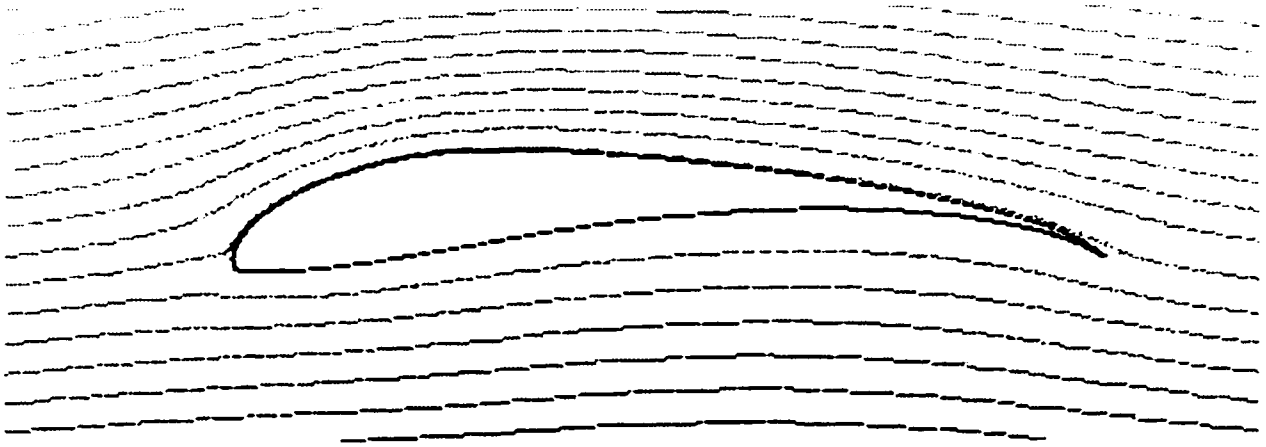

Figure 3.2 The Selig S1223 airfoil at zero degrees angle of attack

the high pressure surface. This flap increases lift by up to five percent at high angles of

attack, while not appreciably increasing the drag. Full span flaperons were installed on the wing to give roll control when used differentially in aileron mode or to adjust the lift and drag on the wing when used as flaps. A conventional aircraft has a wing supported at the fuselage alone while the OHS configuration requires support for the tail boom assemblies at the wing tips. This increases the structural complexity of the wing. The wing is of built up construction using balsa ribs and sheeting, and full span spruce spars reinforced with carbon fiber. The center section near the fuselage is also reinforced with a fiberglass wrap to withstand the excessive bending loads at the wing root. Also, the wing tips were reinforced to handle the bending and torsional forces applied by the tails.

The boom and tail assemblies are quite distinctive on the OHS aircraft. The booms are made from carbon fiber tubes which exhibit very little twist and bending when loaded by the tails. The tail sections are of styrofoam core and sheeted with 0.8 mm thick balsa. A solid balsa block joins the vertical and horizontal tail sections to the boom. Both the wing and tails are covered in a heat shrink mylar film witch adds some strength and results in a smooth finish. Both horizontal sections contain elevators for pitch control and the vertical surfaces contain rudders for yaw control.

3.2.2 Radio Gear

The aircraft is controlled using a Futaba Skysport six channel FM radio. The onboard receiver is located in the front of the fuselage behind the engine firewall. The receiver is powered by a five volt battery pack which is also used to drive the servomotors. The throttle and nose-gear steering use a standard Futaba 148 servomotor, both being located

in the fuselage. Each flaperon has an Airtronics 94141 high-torque micro servo located directly in front of the respective control surface. The elevators and rudders use Airtronics 94143 micro servos also located in close proximity to their respective control surface. This eliminates the need for elaborate mechanical linkages. However, the long power and signal wires used to drive the servos needed to be shielded so as not to interfere with the telemetry transmission and vice versa. Before the long servo wires were shielded, they acted like a giant antenna receiving radio interference from the telemetry transmitter antenna extending from the rear of the fuselage and running parallel to the tail booms.

3.2.3 Telemetry System

The onboard telemetry unit contains four sensors, a transmitter, and a power supply. An angle of attack meter and an airspeed sensor are located mid-station on the right wing as shown in Figure 3.3, while an angular rate sensor and an accelerometer are located at the aircraft center of gravity within the fuselage. The telemetry transmitter, along with the power supply and sensor signal conditioner are also located within the fuselage as depicted in Figure 3.4. All components are encased in foam padded aluminum boxes for increased electromagnetic shielding and security.

Radio interference from the telemetry transmitter has been a major factor in this project. Several components were replaced with alternatives due to their sensitivity to radio noise. A differential pressure transducer employing strain gauges was used to measure airspeed in conjunction with a Pitot tube. The bridge circuitry in the pressure transducer was very sensitive to electrical noise and therefore could not be used. Therefore, an alter-

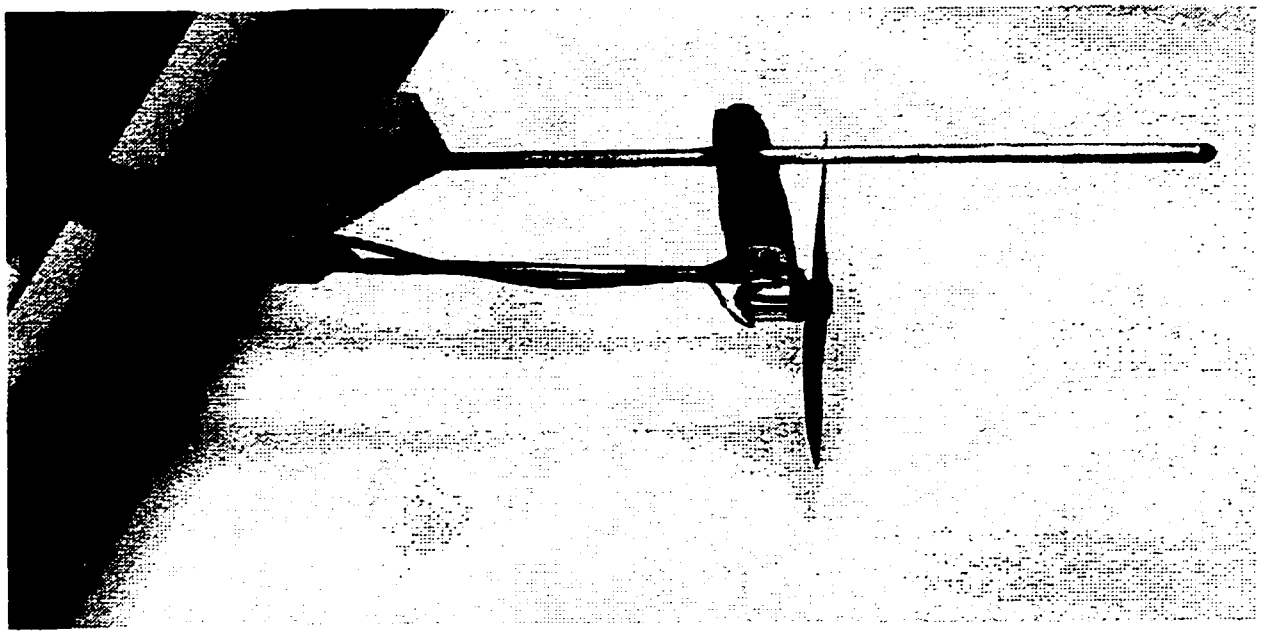

Figure 3.3 Speed sensor and angle of attack meter mounted on wing

nate airspeed sensor was designed. Also, operational amplifiers were found to be greatly affected by the induced noise in the telemetry circuitry. Several attempts at reducing the noise with shielding, diodes, and electrical isolation circuitry failed. The options were either a new transmitter or replace the affected components, the latter being the most effective in terms of cost and time.

3.2.4 Sensors

There are four sensors located onboard the OHS aircraft. A potentiometer is used to measure the angular deflection of a downwind pivoted vane to provide angle of attack. The multi-axis angular rate sensor measures pitch rate and roll rate, and when the signal is integrated, will give pitch and roll respectively. An accelerometer is used to measure ver-

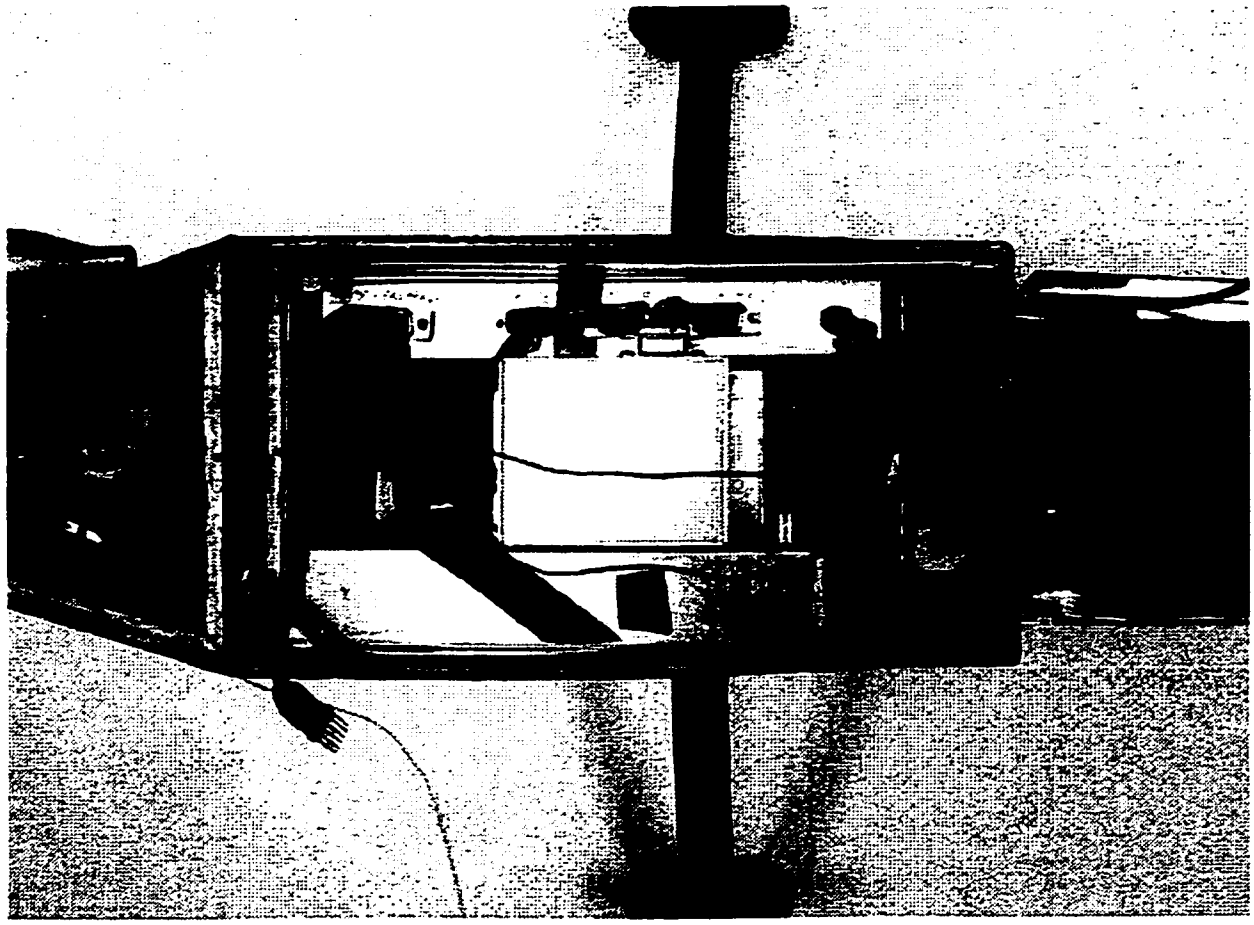

Figure 3.4 Telemetry package within aircraft fuselage

tical displacement, or altitude, and an anemometer (propeller driven DC motor) measures airspeed.

The angle of attack sensor measures the angle between the relative wind and the wing chord. The vane depicted in Figure 3.3 is made of a thin steel plate attached to a steel tube. A counter weight mounted in the nose of the tube statically balances the vane so it lies horizontally when undisturbed. The vane is pivoted on a 5 $k\Omega$ potentiometer mounted to a fixed arm relative to the wing. The endpoints on the resistor are wired to common ground

and five volts while the wiper is the output signal. The change in the angle of the vane thus results in a change in voltage reading with respect to ground through the potentiometer giving angle of attack in volts.

Also mounted on the same fixed arm is the air speed sensor also shown in Figure 3.3. Airspeed is a measurement of the forward motion of the aircraft through the surrounding air. In zero-wind conditions, and body axis coordinate system, the airspeed and forward velocity of the aircraft are identical. This airspeed sensor is analogous to a stationary wind powered generator. A small turbine blade (propeller) is mounted to the shaft of a small DC-motor acting as a generator. When the airspeed is sufficient to overcome the friction in the rotor, the turbine will spin. This rotation will electromagnetically generate a small voltage. The turbine rotational speed is proportional to the airspeed, and the generator output voltage is proportional to its rotational speed. Therefore a proportional constant between airspeed and voltage produced can be determined.

The angular rate sensor is located within a 9.0 cm foam filled aluminum box on the center of gravity of the aircraft. The Watson Industries "tuning fork" angular rate sensor model No. ARS-C332-1A [50] has three sensing axis and a nominal full scale output of ± 300 degrees per second at respectively $\pm 10.0\ V$. The unit is 2.9 cm wide by 5.1 cm long by 5.2 cm high and a mass of 85.0 grams. This transducer consists of two pairs of piezoelectric Bender elements as shown in Figure 3.5.

The two piezoelectric Bender elements are mounted end to end with a 90 degree rotation. The base mounted element is driven such that the sense element swings in a reciprocating arc. When a rate of rotation exists, conservation of momentum causes a

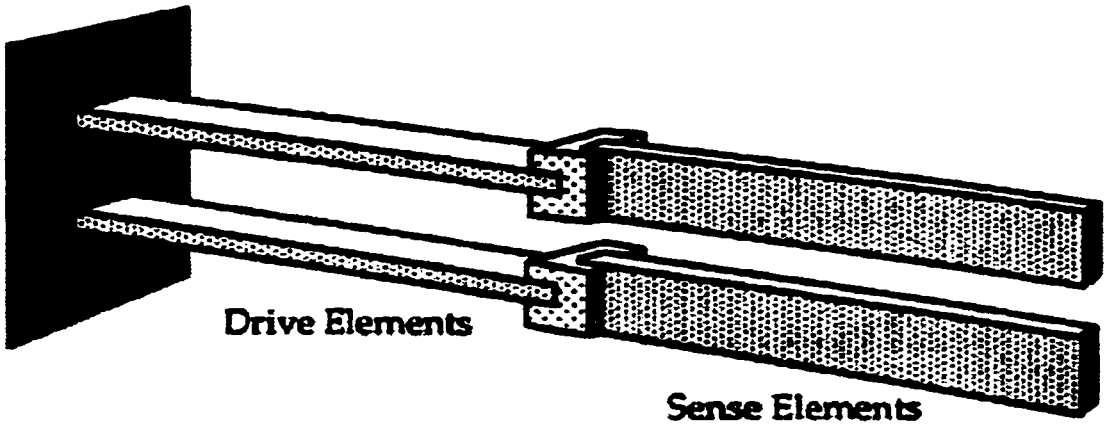

Figure 3.5 Internal diagram of the angular rate sensor

bending in the sense element in turn causing a change in the piezoelectric voltage which is proportional to the angular rate. The phase of the output is dependant on the direction of rotation giving measurement about all three axis. The tuning fork arrangement (i.e. two pairs of piezoelectric elements) reduces the effects of external vibrational and acoustical noise.

The Crossbow Technology Inc. tri-axial steady state accelerometer model No. CXL-04M3 [8] is also located on the center of gravity of the aircraft. It has a full scale output of $\pm$ 4.0 g with a nominal sensitivity of 500 mV/g. The package dimensions are 2.5 cm square at the base and 1.9 cm high with a mass of 20.0 grams. The sensing element is a silicon micromachined capacitive beam held in a force balance. The accelerometer measures

a range from steady state, or DC, up to 100 Hz. This allows altitude, measurements after a double integration of the vertical acceleration signal. The accelerometer signal must therefore be corrected depending on the pitch of the aircraft.

The accelerometer is mounted inside a 6.0 cm cubed foam filled aluminum box. A 115.0 gram lead mass is attached to the accelerometer to increase the inertial mass of the sensor in an attempt to reduce the measured engine vibration noise. The following development shows how increasing the mass reduces the susceptibility to external vibration.

The accelerometer-aircraft system can be modeled as in Figure 3.6 with the mass being the accelerometer and the spring and damper together comprising the foam.

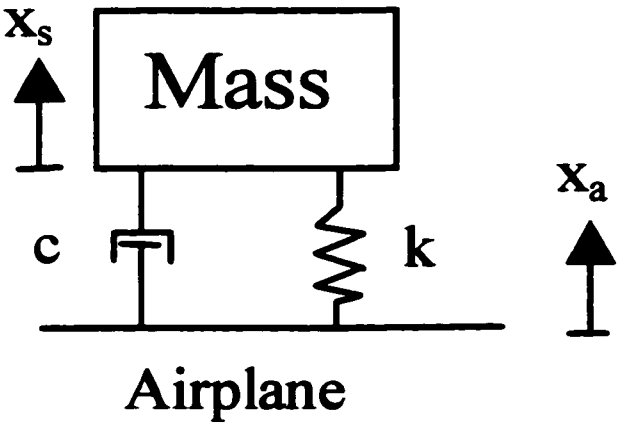

Figure 3.6 Mass-Spring-Damper system

The equation of motion can be written as follows:

$$m\frac{d^2x_s}{dt^2} = -c(\frac{dx_s}{dt} - \frac{dx_a}{dt}) - k(x_s - x_a) \tag{3.1}$$

The system can be transformed to the Laplace domain and rearranged as:

$$\frac{x_s(s)}{x_a(s)} = \frac{cs+k}{ms^2+cs+k} = \frac{1}{m}\frac{cs+k}{s^2+\frac{c}{m}s+\frac{k}{m}} \tag{3.2}$$

Equation 3.2 shows that by increasing m, the displacement of the sensor x_s for a given displacement in the aircraft x_a is reduced, thus reducing the susceptibility of the accelerometer to high frequency vibration caused by the engine. The reduction in damping ($\frac{c}{m}$) is not sufficient to cause an underdamped response and the reduced natural frequency ($\frac{k}{m}$) is still far above the useful bandwidth of 5 Hz.

3.2.5 Sensor Calibration

Each sensor must be calibrated to standard metric units before their signals can be utilized in the experimental setup. The calibration constants are applied to the signals in software before being used in the controller. Simple calibration techniques were employed since a high degree of accuracy in the calibration factors is not required. Since experimental errors due to noise and other disturbances will be larger, a five percent error tolerance for all sensors is acceptable for this application. This research is more interested in the relative response of the system under varying conditions as opposed to precise physical quantities.

The angle of attack sensor was calibrated using a protractor. The vane was rotated through its range of motion at several intervals while recording the outputs as measured by the laptop computer. The results were plotted on a graph shown in Figure 3.7 giving a straight line; the slope of which was taken as the calibration factor. The angle of attack calibration factor was 44 counts per degree with a correlation coefficient of 0.995. The

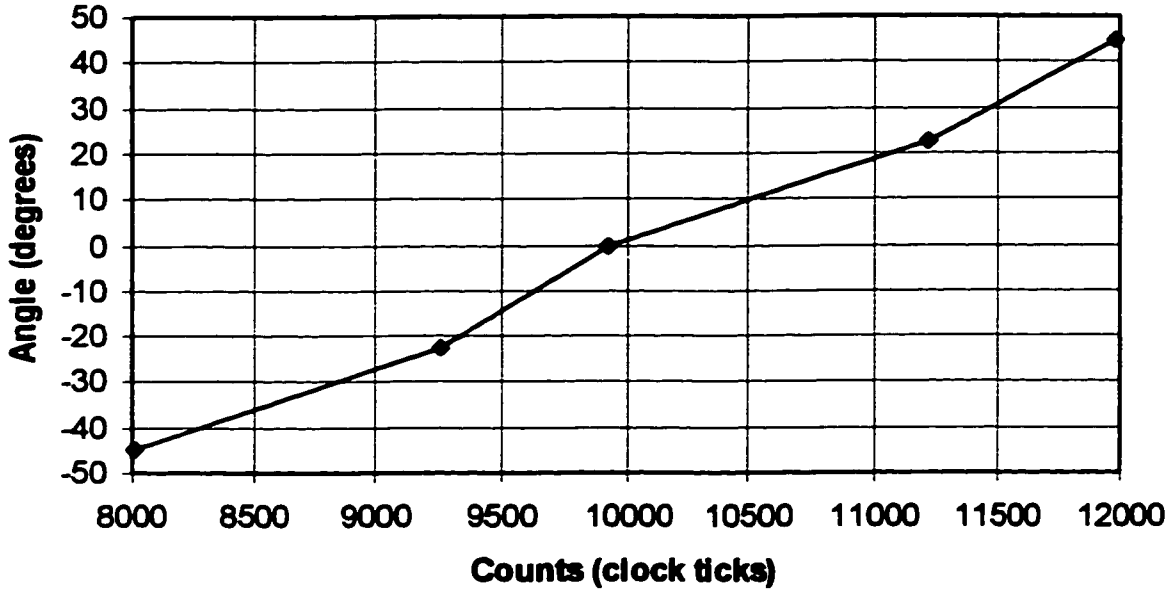

Figure 3.7 Angle of attack calibration curve

counts, or clock ticks are the units of measure outputted by the DAQ system. This is explained in more detail in Section 3.2.8.

The airspeed sensor required the use of a wind tunnel for calibration. The sensor was placed inside an open jet wind-tunnel with a cross sectional area 137 cm wide by 76 cm tall and a maximum air velocity of 16 m/s. The output was measured incrementally from zero to maximum speed and then back to zero, and plotted on a graph as shown in Figure 3.8.

The increasing and decreasing paths are nearly identical indicating that there are no hysteresis effects. The slope of the curve was taken as the calibration factor. The output is measured in counts or clock ticks which is described in Section 3.2.8. The airspeed sensor calibration factor was 152 counts per m/s with a correlation coefficient of -0.997.

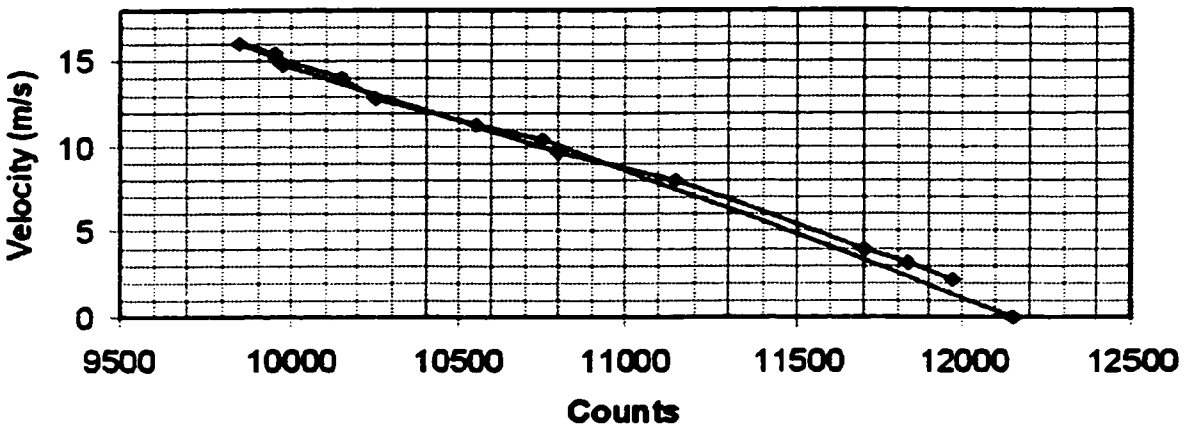

Figure 3.8 Anemometer calibration graph

Since the accelerometer is able to measure steady state acceleration, it was calibrated with the use of gravity. The accelerometer was first placed on a flat surface and a reading was taken. It was then turned through 180 degrees until it was upside down and another reading was taken. The accelerometer had just experienced a change in acceleration of -2 g ($-19.62\ m/s^2$). The change in acceleration divided by the change in output reading gives the calibration factor of 204 counts per m/s^2 for the accelerometer.

There are a number a ways to calibrate an angular rate sensor (gyro), most of which require some sort of constant angular rotation device (i.e. a turntable). This was not necessary for this setup because the gyro signal is integrated by the computer (see Section 3.2.9). The integrated gyro signal yields angle from angular rate giving the means for static calibration. The gyro was rotated incrementally through an angle of 90 degrees while recording the output values. These data generate a straight line on a graph as shown

in Figure 3.9; the slope of which is the calibration factor for the gyro. The angular rate sensor calibration factor was 39 counts per degree for both the pitch and roll axis with a correlation coefficient of 0.996.

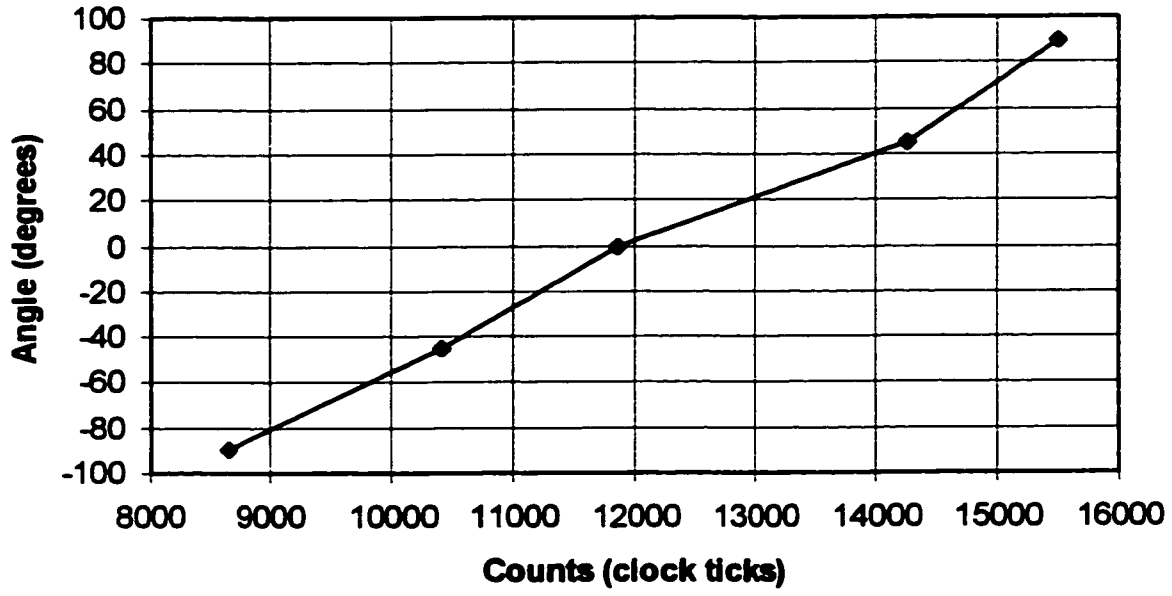

Figure 3.9 Angular rate sensor calibration curve

3.2.6 Signal Conditioning Circuit

The sensor signals must be adjusted to fit the input requirements for the telemetry transmitter. The transmitter requires a DC signal from 1.0 to 4.0 V, therefore output of each sensor must be altered to conform to these specifications. Also, the sensor signals are filtered in order to reduce noise associated with engine vibrations.

Initially, operational amplifier (opamp) circuits were used to amplify the signals and provide DC offsets where needed. This proved unsuccessful in that the opamps were unstable, or erratic, in the presence of the electrical noise emanating from the telemetry transmitter. Significant effort was expended trying to solve the noise problem. Attempts at filtering, shielding and isolation of the transmitter noise proved to be in vain. The signal conditioning circuitry was then restructured to eliminate all active electronic components (i.e. opamps) and replace them with passive ones (i.e. resistors and capacitors) that are less susceptible to radio and high frequency disturbances. Also, a differential pressure transducer used for measuring airspeed in conjunction with a Pitot-static tube was replaced. The sensor used strain gauges mounted to the surface of a diaphragm. The strain gauges measured the deflection of the diaphragm due to the differing pressures on either side. The bridge circuit that produced the signal was very sensitive to electrical noise and every attempt at filtering and isolation failed to resolve this issue. The output would simply saturate to the upper rail voltage making the sensor useless. The sensor was replaced by the anemometer in the form of a turbine driving a small DC motor as mentioned in Section 3.2.4.

The angle of attack sensor uses a 5 $k\Omega$ potentiometer as mentioned in Section 3.2.4. This potentiometer is an artifact of the original radio transmitter as discussed in the following section. The output signal already conforms to the necessary transmitter specifications of 1 to 4 V, therefore, the angle of attack sensor is connected directly to the transmitter.

The DC motor of the velocity sensor required more extensive circuitry. The output of the motor ranges from zero volts at zero speed to 0.5 V at the full speed of the wind

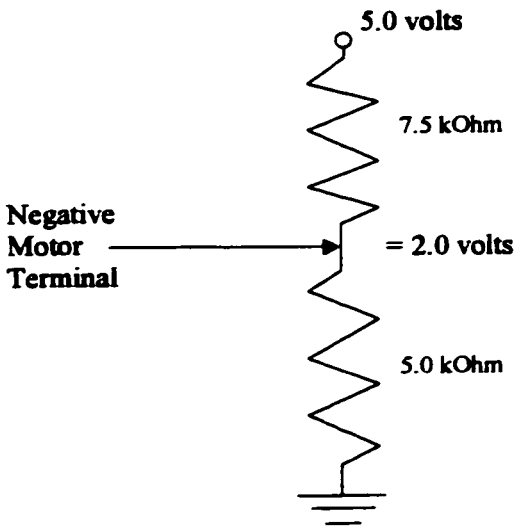

Figure 3.10 Voltage divider resulting in a 2 Volt reference

tunnel ($V_{max} \approx 16\ m/s$). The signal needed a DC shift to bring it into the acceptable range required by the transmitter input. This was accomplished by attaching the negative terminal of the motor to a voltage divider at two volts as shown in Figure 3.10. The output then ranges from 2 to 2.5 V. This is an acceptable signal range and should provide enough resolution (94 counts per m/s). Amplification of the velocity sensor signal would require an opamp circuit which determined to be incompatible with the radio transmitter as mentioned previously in this section.

The angular rate sensor is powered by a $\pm 15\ V$ dual supply, with a common ground connection. The outputs vary between -10 and +10 V so the signals require a DC shift as well as a scaling of the signals. The gyro has bias lines on the outputs so a voltage divider for each output was set up at 2.5 V to shift the signals. The outputs were then scaled using separate voltage dividers to reduce the signal by a factor of seven. The resulting outputs fit into the necessary specification of 1 to 4 V.

The accelerometer uses a +5 V single ended grounded supply with a nominal output of 2.5 V. The full scale output is from 0.5 to 4.5 V at ± 4 g which is very close to the required specification. The accelerometer output was therefore left unaltered. The aircraft should not experience more than ± 3 g in normal operation producing voltage levels within the 1.0 to 4.0 V transmitter limits.

The two gyro, and accelerometer sensor signals were filtered before being transmitted to the ground using three integrated circuit (IC) chip filters. The pre-filtering is done in the aircraft before transmission because the unfiltered signals were saturating the inputs on the transmitter. A reduction in the gain levels would also compensate for this problem except there would be a loss in resolution with the attenuation of the signals. The signals are filtered again in software using native Labview [23] filters on the ground. The gyro and accelerometer pick up vibration from the engine at frequencies corresponding to the operating speeds between 3500 and 10 000 rpm or 58.33 to 166.66 Hz. The outputs of these sensors are filtered through active eighth-order low pass Butterworth filters, with 15 Hz cut-off frequencies which is well below the minimum engine speed. The corner frequency is defined as the point where the filter output is 3.0 dB below the DC gain of the filter and is set by placing a capacitor on the external clock input. The capacitance value dictates the clock frequency which in turn adjusts the corner frequency. The ratio of clock frequency to corner frequency is 100, as set by the manufacturer, thus the clock frequency was chosen to be 1500 Hz giving a corner frequency of 15 Hz. The Maxim switched-capacitor Butterworth filter (Max291) was used because of the flat pass band

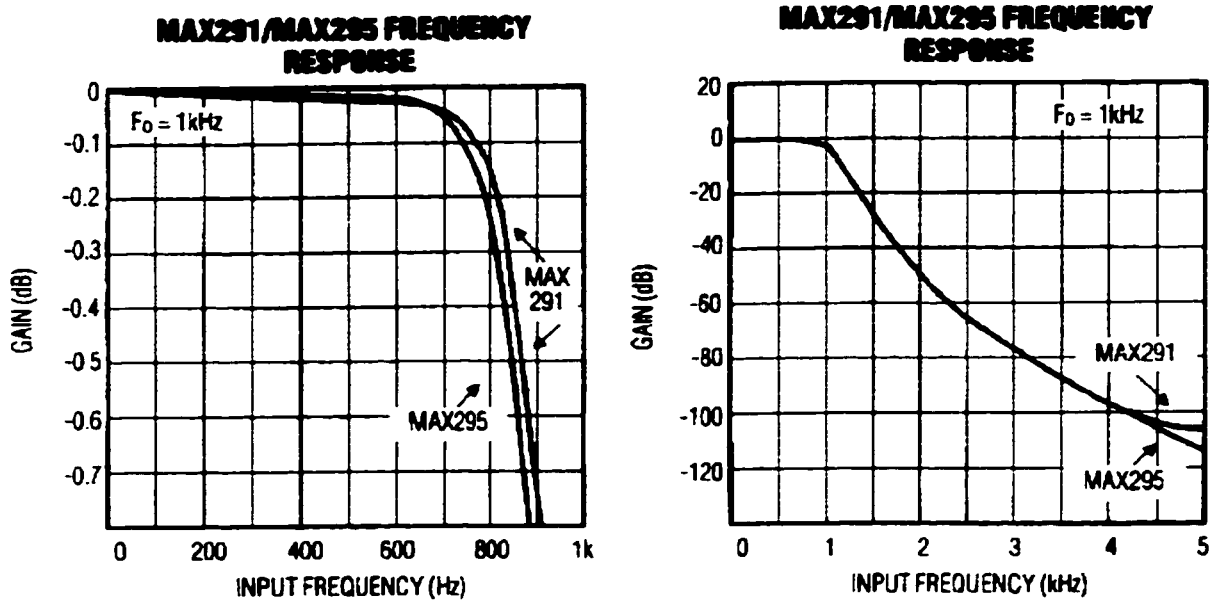

Figure 3.11 Frequency response of the hardware filter (Max291) shown with a corner frequency of 1 kHz

characteristics. The frequency response of the MAX291 filter is shown in Figure 3.11 [32]. Note that these manufacturer graphs use a corner frequency of 1.0 kHz.

Initially, the filters were affected by the radio noise. 0.01 μF capacitors were placed between the filter outputs and ground to fix the problem. These filters substantially reduced the associated noise while not adversely affecting the desired signal. Figure 3.12 shows the signal conditioning circuit and filters.

3.2.7 Telemetry Transmitter

The five sensor signals are transmitted to the ground-based receiver via a nominal 75 MHz frequency modulated radio transmission. The telemetry transmitter/receiver is an

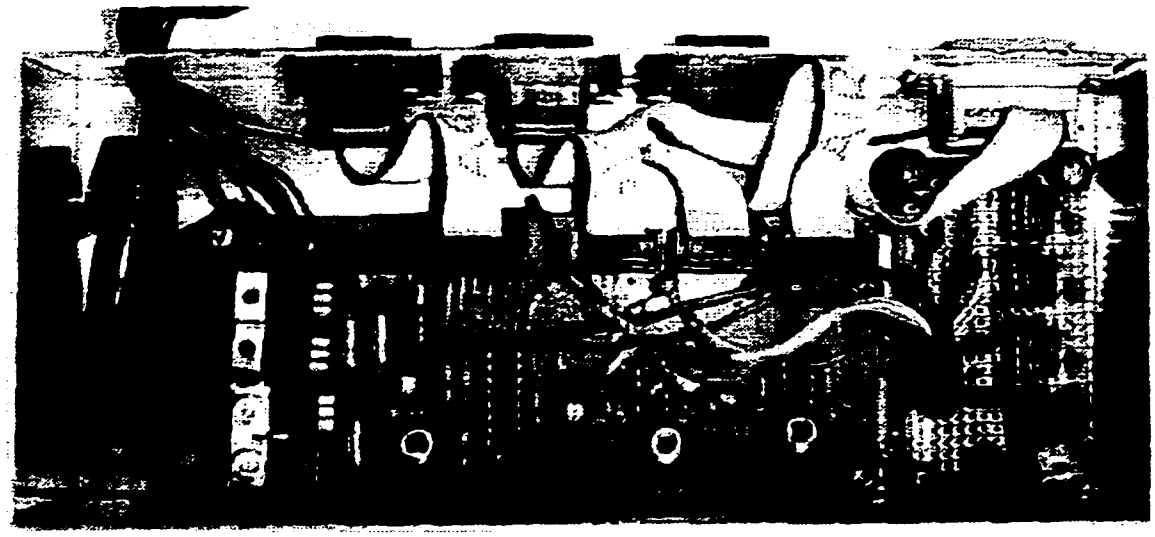

Figure 3.12 Signal conditioning circuitry

RC aircraft radio system operating on a marine frequency to eliminate signal interference between the aircraft flight control radio and telemetry radio.

The transmitter is an Airtronics six channel FM aircraft radio. The transmitter was stripped down to the radio frequency (RF) card, antenna, and multiplexer card. Originally, the transmitter inputs were attached to 5 $k\Omega$ potentiometers operated by the control sticks. For use as a telemetry system, the potentiometers were removed and replaced with the modified sensor outputs. Initially, the telemetry transmitter operated on a model aircraft radio frequency of 72.610 MHz. This caused interference with the pilot transmitter because of the proximity to the aircraft receiver. The fact that the aircraft receiver was so close to the telemetry transmitter, and the frequencies were relatively close resulted in cross talk interference from the side bands. The change was then made to the current 75.510 MHz model marine frequency to avoid such interference. The ground based telemetry antenna

Figure 3.13 Telemetry transmitter

was also increased in length from a quarter wavelength to a half wavelength. This change increased the usable telemetry range of the aircraft to roughly 500 m. Figure 3.13 shows the stripped down telemetry transmitter within an aluminum box.

3.2.8 Data Acquisition

The telemetry radio receiver is mounted inside a data acquisition (DAQ) box that is wired to the computer and the pilot transmitter. The output of the receiver is a pulse width modulated (PWM) signal operating at a frequency of 50 Hz. The PWM signals normally operate the servomotors in an aircraft but in this case are used as telemetry channels. Five

of the six available channels are being used for data acquisition. The sixth receiver channel is not connected but may be used in the future.

The PWM signals are demodulated with the aid of an 8 MHz clock frequency. Each sample is 0.02 seconds long or 1.6×10^5 clock ticks (counts) long. Each signal is modulated into a pulse whose width is proportional to the signal level: $1.0\ V = 7.0 \times 10^3$ counts and $4.0\ V = 1.6 \times 10^4$ counts. The pulses are then stacked serially into the whole pulse group with a four count dead-time in between pulses. Thus the total width of the pulse group is the sum of the six signal pulse widths. Figure 3.14 shows all of the pulses before they are de-multiplexed. As one pulse widens, the rest of the pulses shift to the right and vise versa. The time, in clock ticks, between the leading and trailing edges of each pulse is measured in the channel sequence: one, three, five, two, and four, over two complete cycles. Alternate pulses are measured because the gaps between the pulses are too short to pick up the leading edge of the next consecutive pulse. For example, channel one is measured in clock ticks, this value is transferred to a memory buffer and then the next channel, channel three, is measured and the value is stored, and so on. The resulting sampling frequency is 25 Hz because it takes two cycles to retrieve one sample of data.

The telemetry signals, along with the elevator and throttle inputs, are converted from numeric values to a digital stream and then sent to the laptop computer over the serial port. The serial signal consists of 15 bytes, a lead byte and 14 data bytes. Each of the five data channels and two control stick channels uses two bytes, a high byte and a low byte, giving a 16 bit resolution from 0-65535. The lead byte is identified by a one in the most significant bit (MSB) while the data bytes all have zeros as their MSB. This zero MSB for all the data

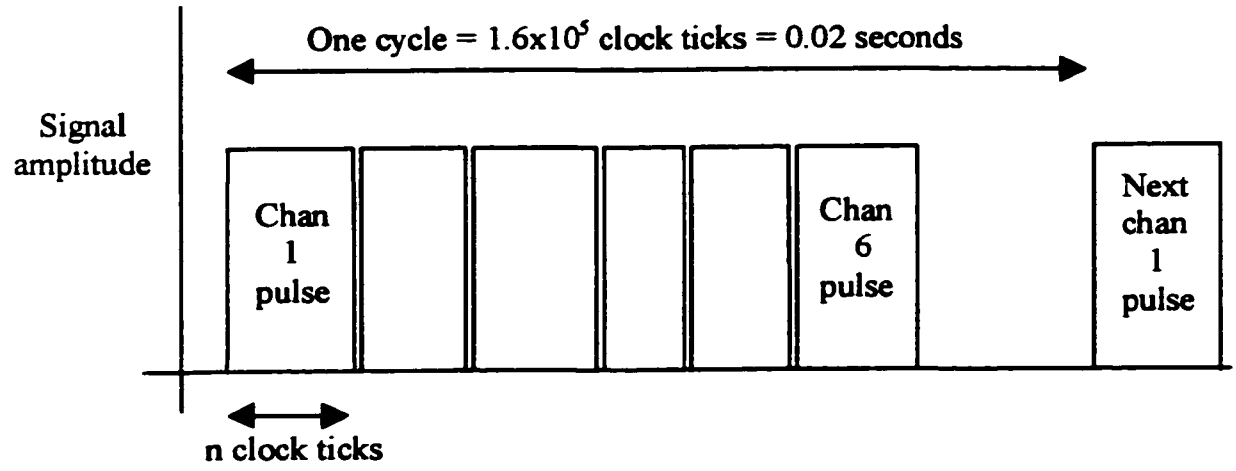

Figure 3.14 Pulse width modulated receiver signal

bytes is accomplished in two steps. The first step is to limit the maximum value to 32767 keeping the MSB of the high byte of each channel a zero. The second step is to force the MSB of each low byte to zero and map those bits onto the lead byte. For example, if the MSB of channel one is a one, then it will first be converted to a zero, and the least significant bit (LSB) of the lead byte will be a one as shown in Figure 3.15.

Control signal data is received by the DAQ box from the laptop computer in a similar manner. In this case, there are only the two control stick signals, elevator and throttle, being outputted from the computer. This gives one lead byte and four data bytes. The signals received from the laptop computer are decoded and then sent to the pilot transmitter after passing through 12 bit digital to analog (D/A) converters. The encoding and decoding process is done with a Z80 based embedded controller with $32k$ RAM, $8k$ ROM, and a $2Mhz$ clock frequency, running an assembly based program. The DAQ box was designed

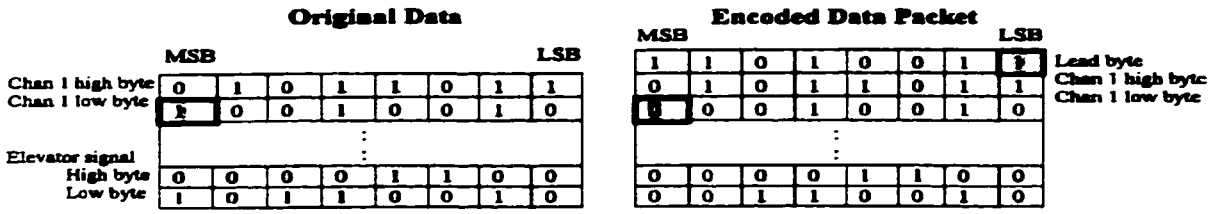

Figure 3.15 Encoding the serial byte stream

to be expandable by reprogramming the software and adding more D/A converters. Figure 3.16 shows inside the DAQ box.

3.2.9 Computer Controller

The ground based computer controller is a Digital Pentium 233 laptop with 48 MB of RAM and a 4.0 GB hard drive. The data collection, and signal processing, is programmed in Labview [23], an instrumentation software package that enables a computer program to run in the background of a graphical user interface. The programming language is called G for graphical programming. Instead of text based languages such as C, this language uses wiring diagrams. A sample program is shown in Figure 3.17. The actual Labview program is shown in Appendix A.

The Labview program reads the serial data one 15 byte packet at a time. This is accomplished by searching for a one in the MSB of the byte stream. When the lead byte has been located, the next 14 bytes are read from the serial buffer. An error checking routine checks the next byte for a one in the MSB verifying the lead byte. If the next byte is verified as the lead byte, then the packet is used, otherwise, the faulty packet is discarded

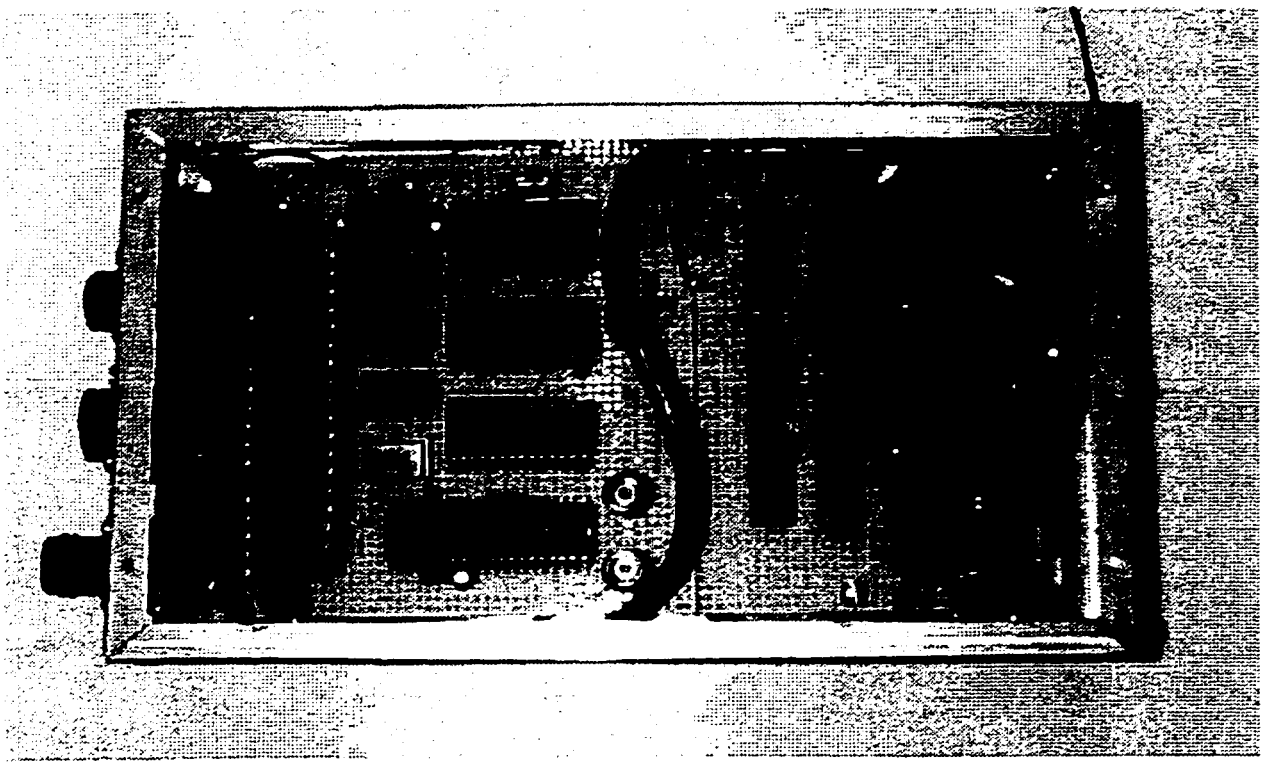

Figure 3.16 Data acquisition box containing telemetry receiver, A/D to computer and D/A to flight transmitter

and the search for the next lead byte continues. The data is decoded (i.e. reassembled), and de-multiplexed to form the original seven data channels.

The main program uses a while loop that waits for data samples to appear in the serial buffer. This times the program execution with the sampling interval of 25 Hz dictated by the DAQ system. The raw data is calibrated, using the calibration factors from Section 3.2.5, to standard SI units. The sensor and pilot stick signals are stored to an ASCII spreadsheet file on completion of the experiment. The data can then be analyzed at a later time.

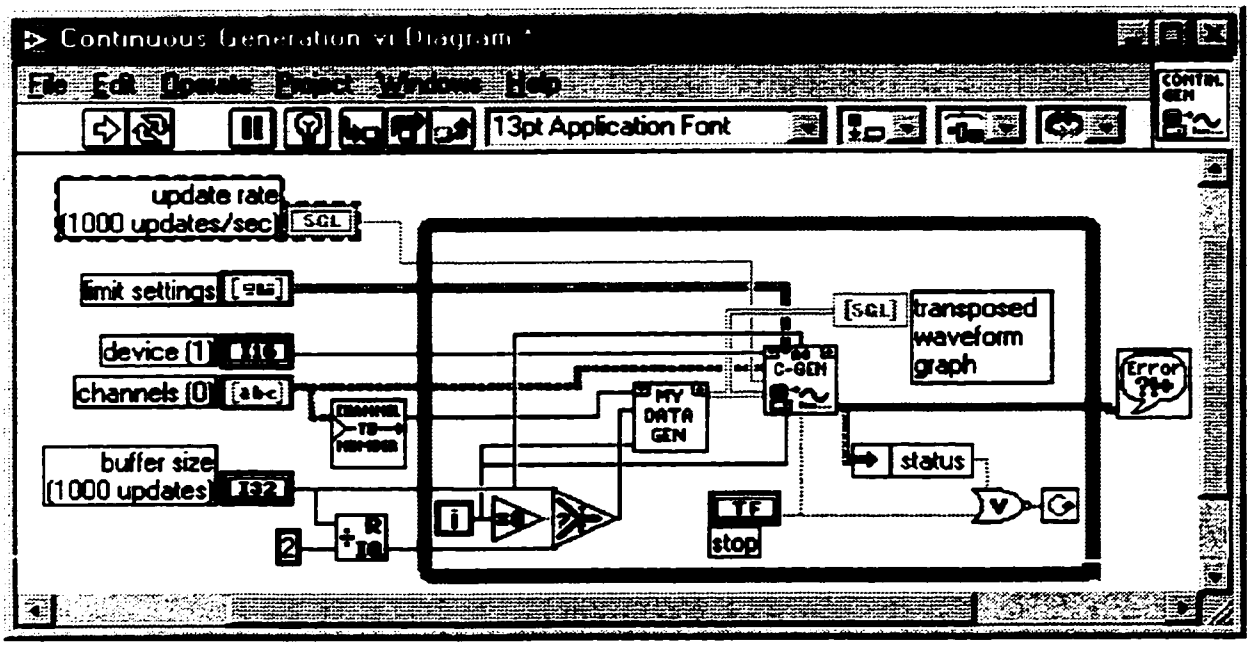

Figure 3.17 Sample Labview diagram

Closed loop control experiments were also conducted using this system. During closed loop control, the sensor signals are used as feedback to the controller as in Figure 3.18.

The sensor signals, along with the pilot stick inputs, are processed by the controller. The output of the controller (i.e. controlled elevator and aileron signals) is then converted to a serial byte stream and returned to the DAQ box. The encoding process is accomplished in the same manner as described in Section 3.2.8. The controlled signals are then sent to the pilot transmitter which are then conveyed to the aircraft actuators.

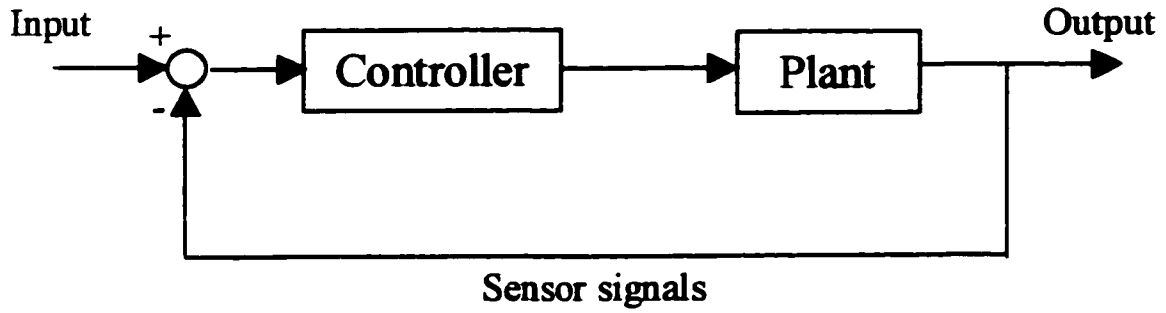

Figure 3.18 Feedback control diagram

3.2.10 Pilot Transmitter

The pilot is in one way communication with the aircraft, sending signals via the Futaba six channel FM aircraft radio which operates on a frequency of 72.910 MHz. The radio transmitter operates in two different modes. In the first mode, **MANUAL CONTROL**, the pilot has full authority of all the controls including throttle, rudder, aileron and elevator. While in the second mode, **COMPUTER CONTROL**, the computer takes control of elevator and aileron. The pilot however, remains in control of rudder and throttle. The pilot can choose which mode is active with a toggle switch located at the top of the transmitter as shown in Figure 3.19. In both modes, the stick signals are sent to the DAQ box and relayed to the computer over the hard wire connection between the transmitter and the DAQ box. In the case of an emergency situation, the pilot can at any time re-assume full control of the aircraft with the **computer-manual control** toggle switch.

The pilot can also control the on/off state of the transmitter on board the aircraft. Interference from the telemetry transmitter can cause the receiver in the aircraft to lose reception from the pilot transmitter. In these situations, the pilot can shut off the power

to the telemetry transmitter from a switch on the pilot transmitter. A power MOSFET (metal oxide semiconductor field effect transistor) switch is connected to the power supply of the telemetry transmitter and to a spare channel on the aircraft receiver. This channel is controlled by the channel five toggle switch located on the pilot transmitter.

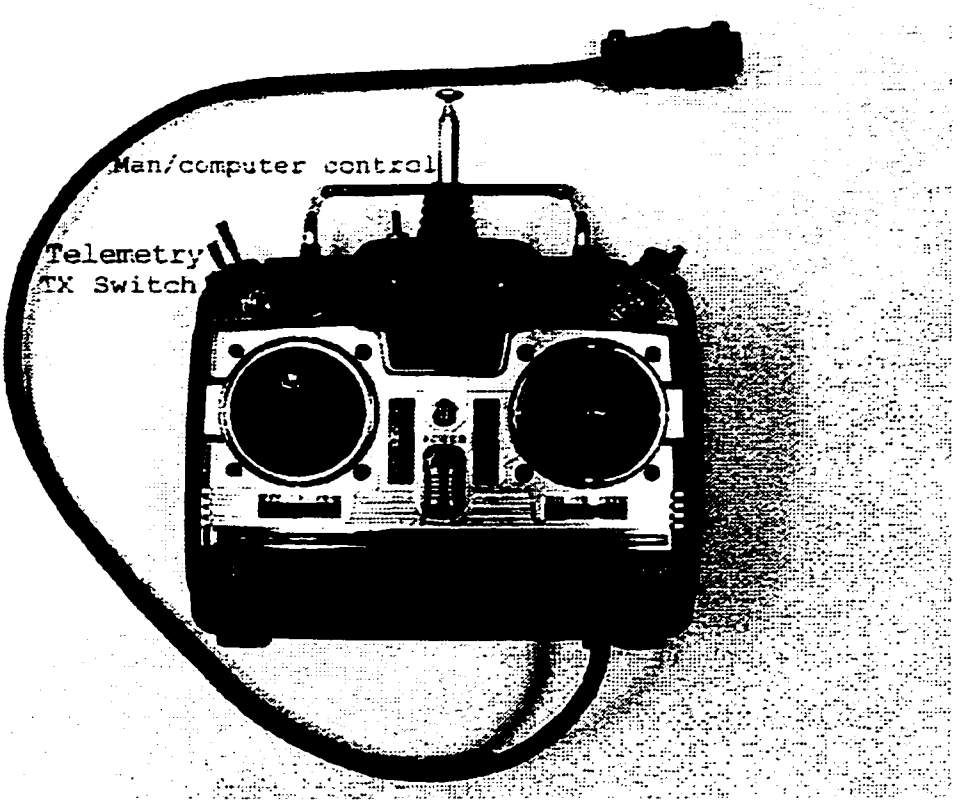

Figure 3.19 Pilots transmitter

3.3 Summary

Presented in this chapter are the major issues associated with the instrumentation of the remotely controlled OHS aircraft. Sensor suitability, radio interference and data acqui-

sition were major problems pertaining to the experimental setup. The radio interference issues were solved with appropriate sensor selection, shielding of external wires, the use of capacitors on the outputs and replacing the opamp circuits with passive components. The result is a full functioning real-time feedback control system operating at a sampling frequency of 25 Hz. The five sensor outputs include pitch rate, roll rate, vertical acceleration, airspeed, and angle of attack and the two inputs elevator and aileron.

Chapter 4
Theoretical Modelling

4.1 Introduction

A plant model is a necessity in the control system design process. The model initiates the direction for the rest of the control procedure. The complexity, or order of the model dictates certain factors such as using state feedback or output feedback. If the states are not available as outputs, an observer is required. These and other such considerations must be made when developing the theoretical model.

The aircraft model is based on the longitudinal dynamics of the OHS aircraft. These are essentially the pitching motions about the center of gravity, and variations in velocity and altitude. The lateral dynamics, consisting of the rolling and yawing motions, are not considered at this time.

4.2 First Principles

The first approach, and the concern of this chapter, is an analytical model based on Newton's second law of forces

$$\sum F = ma = m\ddot{x} \tag{4.3}$$

$$\sum M = I\alpha = I\ddot{\theta} \tag{4.4}$$

where F = force, m = mass, $a = \ddot{x}$ = acceleration, M =moment, I = moment of inertia, $\alpha = \ddot{\theta}$ = pitch acceleration. The aerodynamic and inertial moments were taken about the center of gravity of the aircraft. This included lift and drag forces on the main plane, tail surfaces and fuselage as well as the pitching moments of the wing and tail.

$$L = qSC_L \tag{4.5}$$

$$D = qA_fC_D \tag{4.6}$$

where q = dynamic pressure, S = planform area, C_L = lift coefficient, A_f = frontal area, and C_D = drag coefficient. The coordinate system is then transformed from body axis to global coordinates using an Euler transform. The modelling approach used was developed by Dommasch et al [9] and modified to account for the OHS configuration.

4.2.1 Lift

The most important concept in an aircraft is how lift is produced and on the OHS aircraft, the overall lift is generated in an unusual manner. The lift on the OHS aircraft is produced by both the wing and the tails, as opposed to conventional aircraft where the tail is nominally non lifting or slightly negative lifting. For these reasons, a brief discussion on the subject follows.

Lift is the component of the external forces on the aircraft that is orthogonal to the relative velocity of the aircraft. The magnitude of the lifting force must be equal to the weight of the aircraft in non accelerating straight and level flight. In the case of the OHS aircraft, all the lift is generated by the wing and tail surfaces in horizontal flight. The cross sectional shape, or airfoil section, provides a significant amount of the overall lift. The

airfoil is shaped to induce a faster airflow over the top surface as compared to the bottom resulting in a lower pressure. The pressure differential, shown in Figure 4.1 [12], produces a net lifting force on the wing. Also, the angle at which the wing strikes the airflow, or

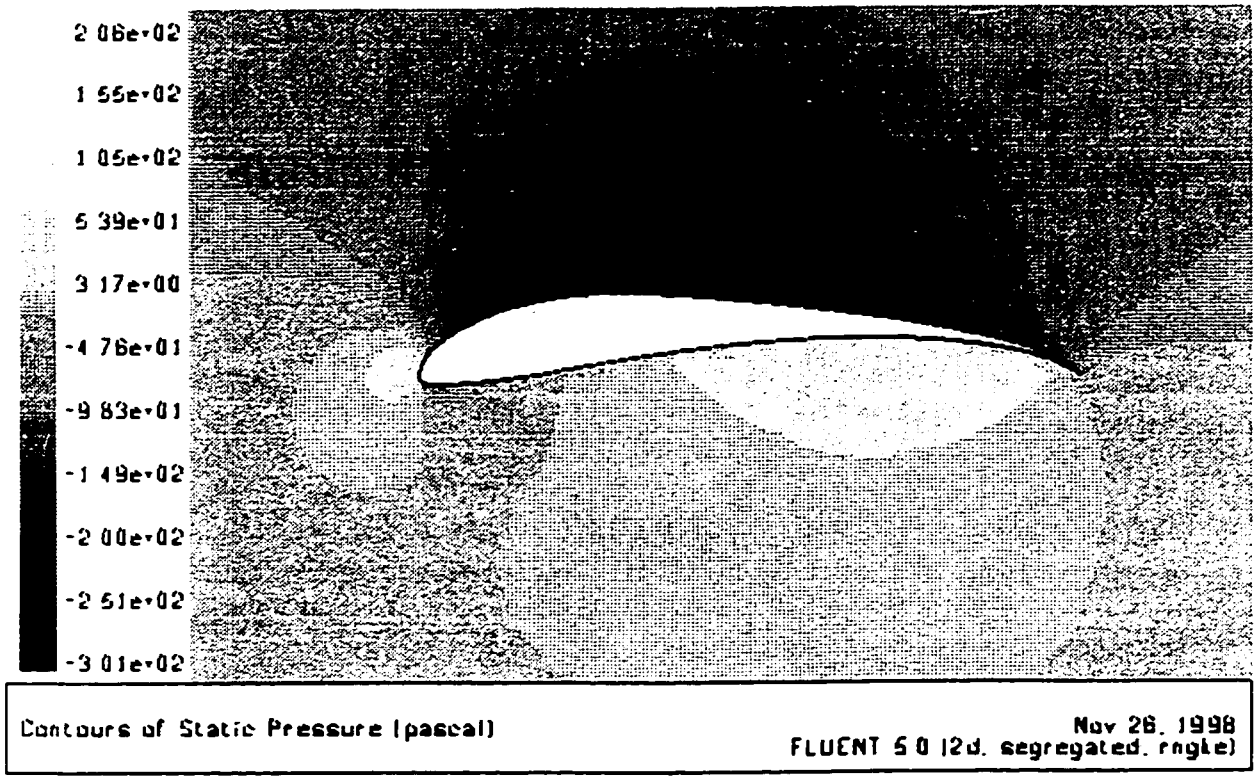

Figure 4.1 The Selig S1223 airfoil shown with a pressure distribution at zero degrees angle of attack

angle of attack, dictates the amount of lift generated. An increase in angle of attack results in an increase in lift as shown in Figure 4.2. The lift coefficient curve was calculated via X-Foil [10]. This is a linear curve until the stall occurs at roughly 14 degrees. This is the point at which the flow detaches itself from the upper surface. The detached flow region causes a dramatic decrease in lift and corresponding increase in drag.

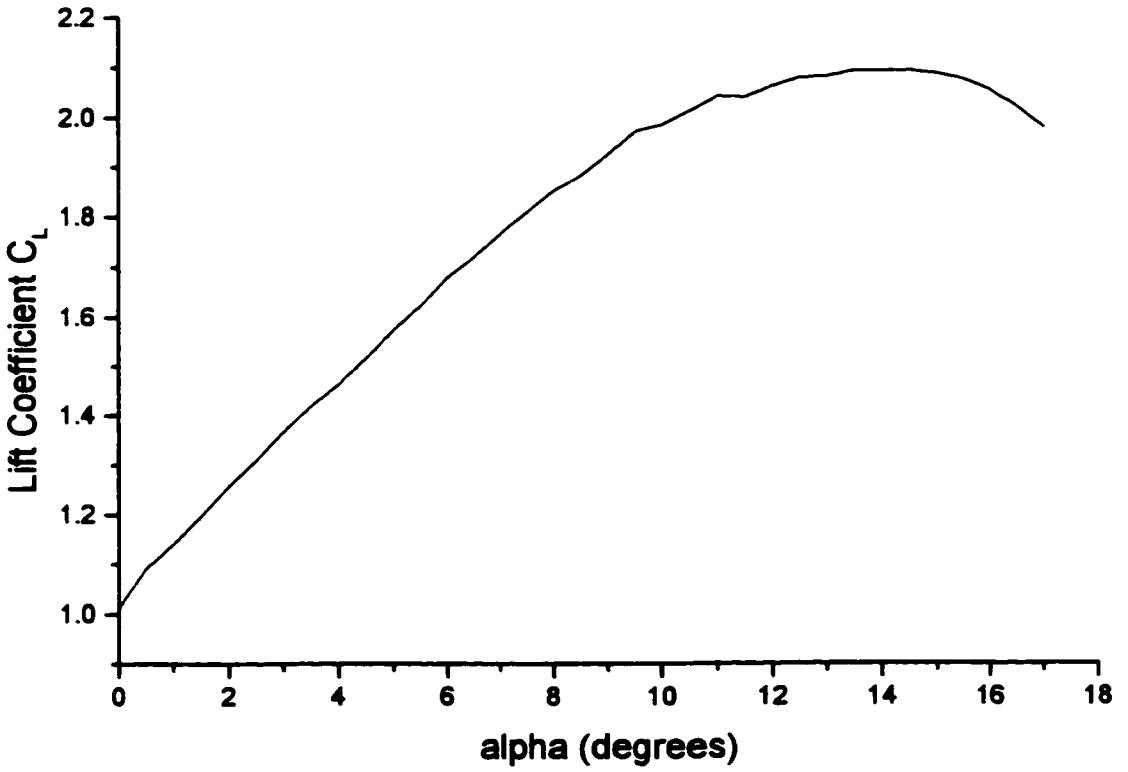

Figure 4.2 Lift coefficient vs angle of attack for the Selig S1223 airfoil without a gurney flap (Lift calculations performed via X-foil)

4.3 Non-Linear Dommasch Model

A non-linear set of differential equations is developed in [9] describing the longitudinal dynamics of a conventional aircraft. Modifications to the original equations in [9] were required to take into account the difference in the dynamics between the OHS and conventional aircraft configurations.

The differences between an OHS and a conventional aircraft are most apparent in the way the airflow behaves on the horizontal tail surfaces. In a conventional design, where

the single tail is centrally located behind the mainplane, the tail encounters the downwash from the mainplane. Conversely, the tails of the OHS aircraft are located in the upwash generated from the wing tip vortices as shown in Figure 4.3.

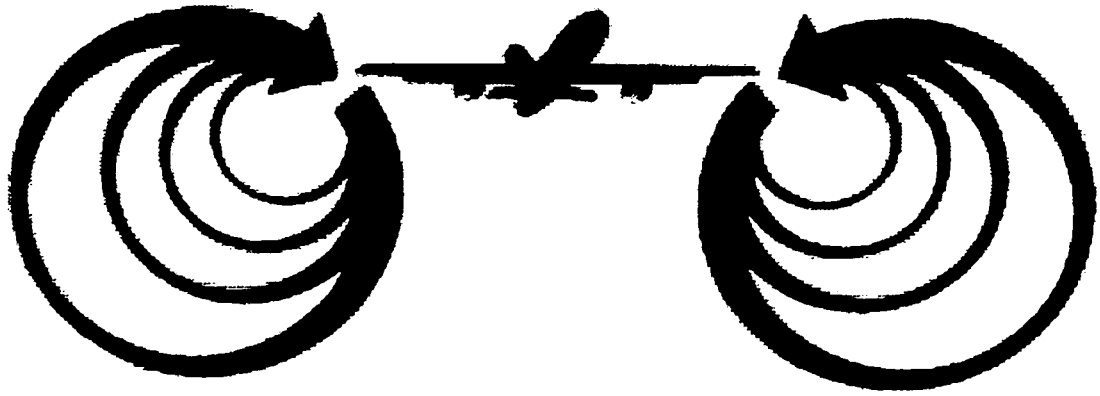

Figure 4.3 Wing tip vortices

Figure 4.4 shows a graphical representation of the flow field downstream of the right wing tip. The horizontal tail surfaces, existing in the upward flow regime, are able to have a negative angle of incidence while maintaining a positive angle of attack. The lift vector is now skewed forward as shown in Figure 4.5, negating some drag resulting in a very efficient lifting surface. Conversely, on a conventional aircraft horizontal tail, located in the downwash behind the wing, a positive angle of incidence would be required in order to create lift. The result is a lift vector skewed aft, adding to the drag already present.

The vertical tails also experience similar benefits being positioned within the wing tip vortices. A cross or inward flow, as seen in Figure 4.6, allows the vertical tails to be angled

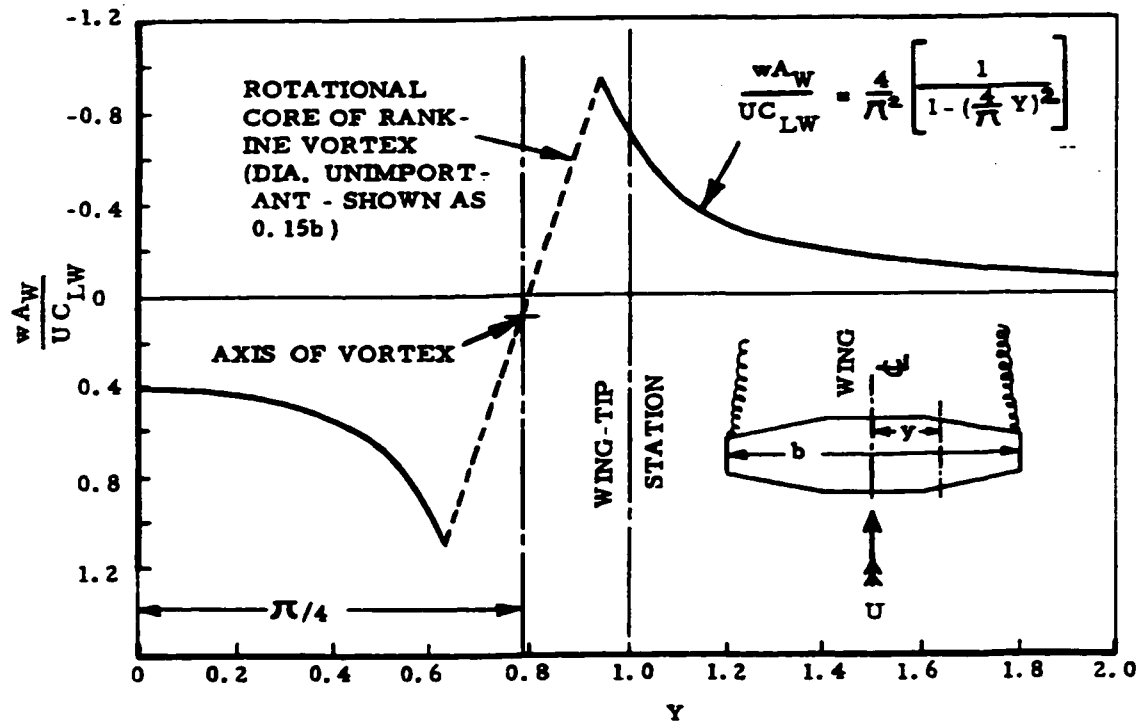

Figure 4.4 Flow field downstream of the right wing tip for an eliptically loaded wing

outward slightly. The angles are exaggerated for visualization purposes. The sideways force vector is skewed forward actually negating the drag of the vertical tail.

The relative stability of the aircraft is also altered due to the unusual tail placement. Consider the OHS in straight and level flight. As the nose pitches up, the lift coefficient increases on the mainplane due to the increase in angle of attack, thus resulting in an increase in the strength of the wing tip vortices. The tails, positioned in the upwash, react to the altered flow with an increase in the lift generated, providing a stabilizing, or nose down,

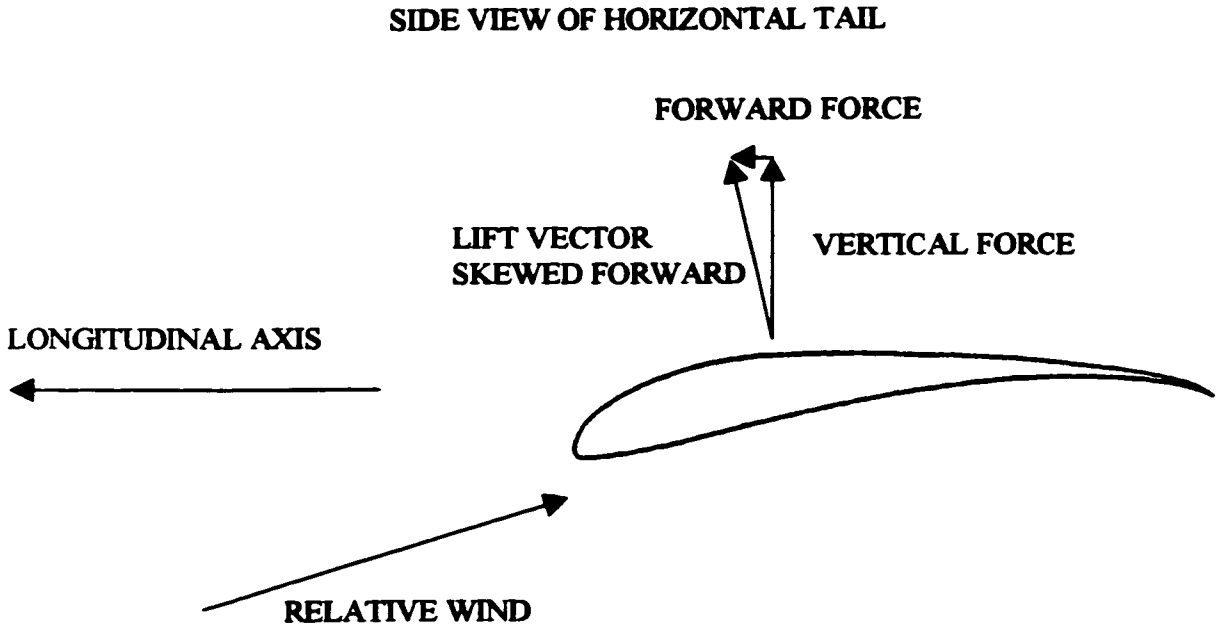

Figure 4.5 Effects of tip vortices on the horizontal tails

pitching moment. This damping or leveling effect occurs similarly for the nose down case, resulting in a moderately damped, stable aircraft.

Conversely, in a conventional aircraft, as the nose pitches up, the same increase in lift coefficient is experienced by the mainplane resulting in stronger tip vortices. Now, since the tail is positioned in the downwash flow regime centered behind the wing, there is a downward force, or a nose up moment. This initially aggravates the nose up attitude until other aerodynamic forces drive the nose back down. The nose down case can also be seen to provide an upward force on the tails forcing the nose down even farther. The result is an aircraft with lower stability and lower longitudinal damping than an OHS aircraft.

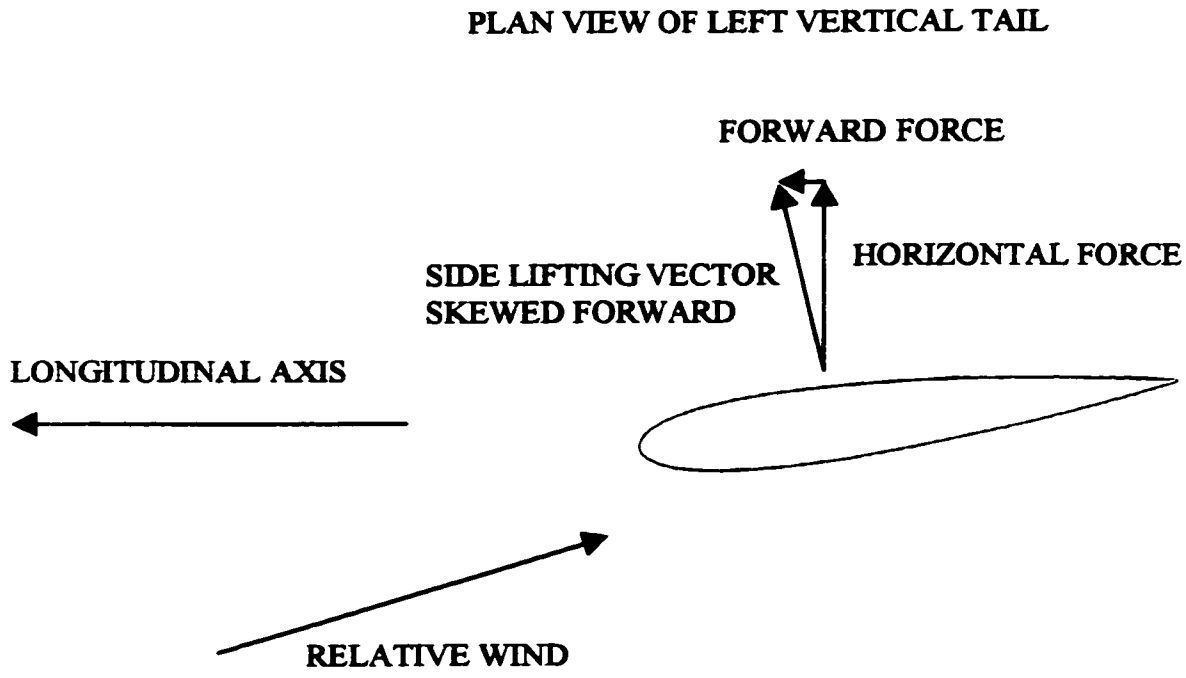

Figure 4.6 Effects of tip vortices on the vertical tails

The differences in aircraft dynamics are predominantly embedded in the pitching moment coefficient derivative in the following equation.

$$C_{Mcg} = C_{Mac} + C_L\frac{x'}{c} - (\alpha - i_w + i_t + \varepsilon)\frac{dC_{Lt}}{d\alpha_t}\frac{lS_tq_t}{qSc} \tag{4.7}$$

where C_{Mcg} = coefficient of pitching moment about the c of g, C_{Mac} = coefficient of pitching moment about the aerodynamic center, C_L = lift coefficient, x' = distance from c of g to neutral point, c = wing chord, α = wing angle of attack, i = incidence angle, l = c of g to tail distance, S_t = tail planform area, and q = dynamic pressure. The ε term is the angle that the airflow is turned by the main plane before it strikes the tail, also known as the downwash angle, or upwash angle for an OHS. The OHS aircraft has a positive ε while in a conventional aircraft ε is negative. This effect can be seen graphically in Figure 4.7. In

particular, the pitching moment coefficient, for the OHS configuration, has a much stronger relationship with angle of attack. The more negative the slope, the more stable the aircraft in a local sense.

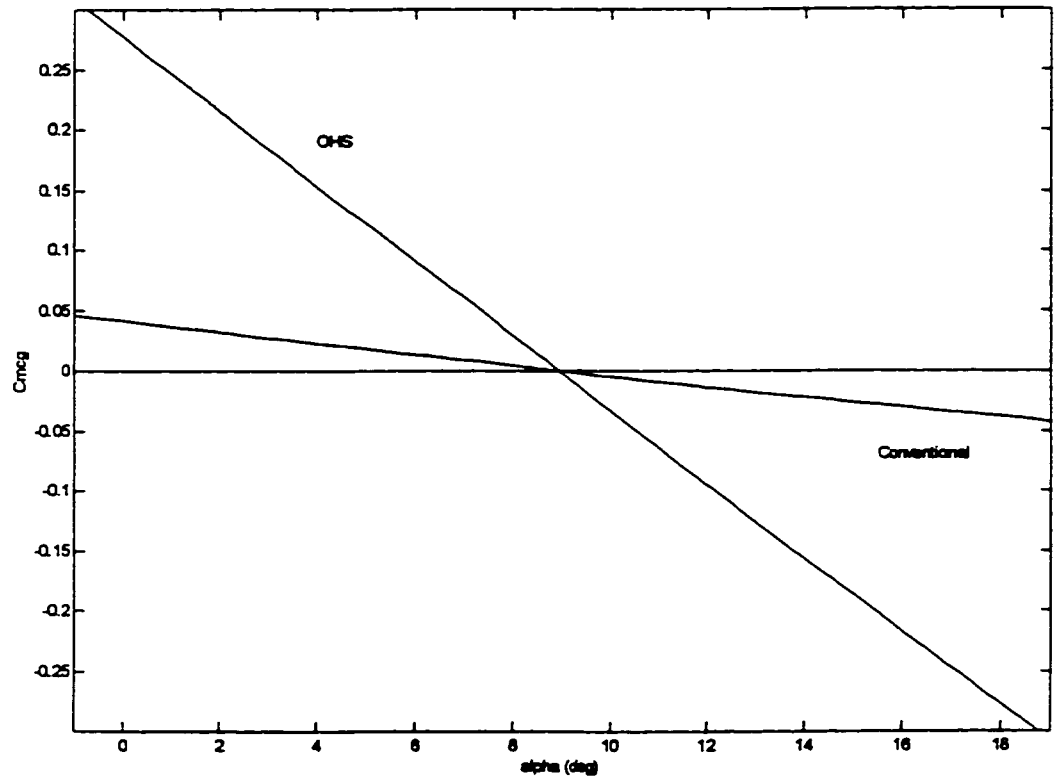

Figure 4.7 Pitching moment curves for a conventional and OHS aircraft

The differential equations of motion for this OHS aircraft can be written as follows:

$$\frac{d\overline{v}}{dt} = \frac{-2C_d g}{C_L V}\overline{v} + \left(g - \frac{2ga}{\pi eAR}\right)\overline{\alpha} - g\overline{\theta}$$

$$\frac{d\overline{\alpha}}{dt} = \frac{-2g}{V^2}\overline{v} - \frac{ag}{C_L V}\overline{\alpha} + \dot{\overline{\theta}}$$

$$\begin{aligned} \frac{d\overline{\theta}}{dt} &= \dot{\overline{\theta}} \\ \frac{d\dot{\overline{\theta}}}{dt} &= \frac{dC_{Mcg}}{dC_L} \cdot \frac{qSc}{aI}\overline{\alpha} - \frac{a_t l^2}{VI} q_t S_t \dot{\overline{\theta}} \\ \frac{d\overline{h}}{dt} &= -V\overline{\alpha} + V\overline{\theta} \end{aligned} \tag{4.8}$$

for the state variables:

$\overline{v}$ = Velocity

$\overline{\alpha}$ = Angle of attack

$\overline{\theta}$ = Pitch

$\dot{\overline{\theta}}$ = Pitch Rate

$\overline{h}$ = Altitude

and aerodynamic coefficients

$C_D = f(\alpha, V^2)$, Coefficient of Drag

$C_L = f(\alpha, V^2)$, Coefficient of Lift

g = Acceleration due to gravity $(9.81 m/s^2)$

$a = \frac{dC_L}{d\alpha}$

V = Nominal velocity

e = Oswald efficiency factor

AR = Aspect ratio (S/c)

$q = \frac{1}{2}\rho V^2$ = Dynamic pressure

ρ = Air density

S = Wing span

c = Average wing chord

I = Measured moment of inertia

l = Distance from c of g to tail center of pressure

$(\cdot)_t$ = tail

C_{Mcg} = Pitching moment coefficient about the center of gravity

4.4 Linearization

The fixed gain controllers are designed about a linear model. Thus the non-linear model from above must be linearized by choosing constant values for the aerodynamic coefficients at the nominal operating condition. The Dommasch model is a zero input response representation. The model was modified to include external inputs by choosing control derivatives to match steady operating conditions in the experimental aircraft. The set of experiments in this section uses elevator as the sole input to the system in combination with the five outputs listed above. Note that the lateral variables, i.e. aileron, roll, and roll rate, are kept separate.

4.5 State Space Representation

The linear set of differential equations can then be converted to state space form for ease of analysis and manipulation. The state equation is written as

$$\dot{x} = Ax + Bu \tag{4.9}$$

where $x = \begin{bmatrix} \bar{v} & \bar{\alpha} & \bar{\theta} & \dot{\bar{\theta}} & \bar{h} \end{bmatrix}^T$ and $u = \Delta_{elev}$, the pilot elevator commands. The output equation is represented as

$$y = Cx + Du \tag{4.10}$$

The following system is obtained by evaluating all of the variables in Equation 4.8. The B matrix is chosen to match steady state operating conditions based on computer simulations.

$$\begin{aligned} A &= \begin{bmatrix} -0.125 & 5.177 & -9.810 & 0 & 0 \\ -0.049 & -3.924 & 0 & 1 & 0 \\ 0 & 0 & 0 & 1 & 0 \\ 0 & -2.073 & 0 & -3.378 & 0 \\ 0 & -11 & 11 & 0 & 0 \end{bmatrix} \\ B &= \begin{bmatrix} 0.03 \\ 0.7 \\ 0.5 \\ 1.4 \\ 0.002 \end{bmatrix}, C = \begin{bmatrix} 1 & 0 & 0 & 0 & 0 \\ 0 & 1 & 0 & 0 & 0 \\ 0 & 0 & 1 & 0 & 0 \\ 0 & 0 & 0 & 1 & 0 \\ 0 & 0 & 0 & 0 & 1 \end{bmatrix} \\ D &= 0_{5x5} \end{aligned} \tag{4.11}$$

4.6 Model Validation

The above model can now be used for simulation and further analysis. The eigenvalues of the A matrix show two distinct sets of poles corresponding to the long (phugoid) and short period modes as depicted in Figure 4.8. The damping ratio of the long period mode can be calculated from the pole locations as follows:

$$\begin{aligned} \zeta &= \left| \frac{real\ \ part}{magnitude} \right| \\ &= \left| \frac{-0.07}{0.66} \right| \\ &= 0.11 \end{aligned} \tag{4.12}$$

The long period mode in an aircraft usually has a period of oscillation of roughly 10 to 20

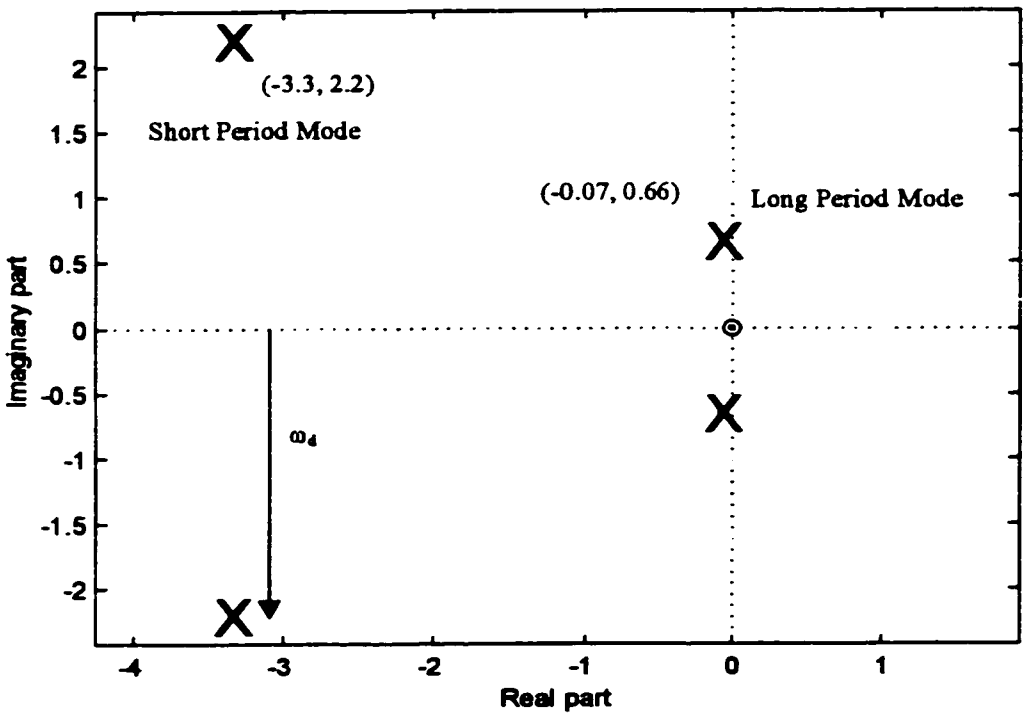

Figure 4.8 Poles of the Linearized Dommasch model

seconds. The airplane will follow a sinusoidal path pitching up and down (Figure 4.9). The phugoid oscillation takes place at near constant angle of attack and is visualized as an exchange of energy; altitude for airspeed and vice versa.

The short period mode is simply small rotations about the center of gravity of the aircraft in flight (Figure 4.10). This mode occurs at nearly constant airspeed. Most aircraft have a lightly damped stable long period mode.

Some aircraft have unstable long period modes. This is not usually a critical problem, just a nuisance for the pilot to correct, because it is such a slow oscillation. This is not

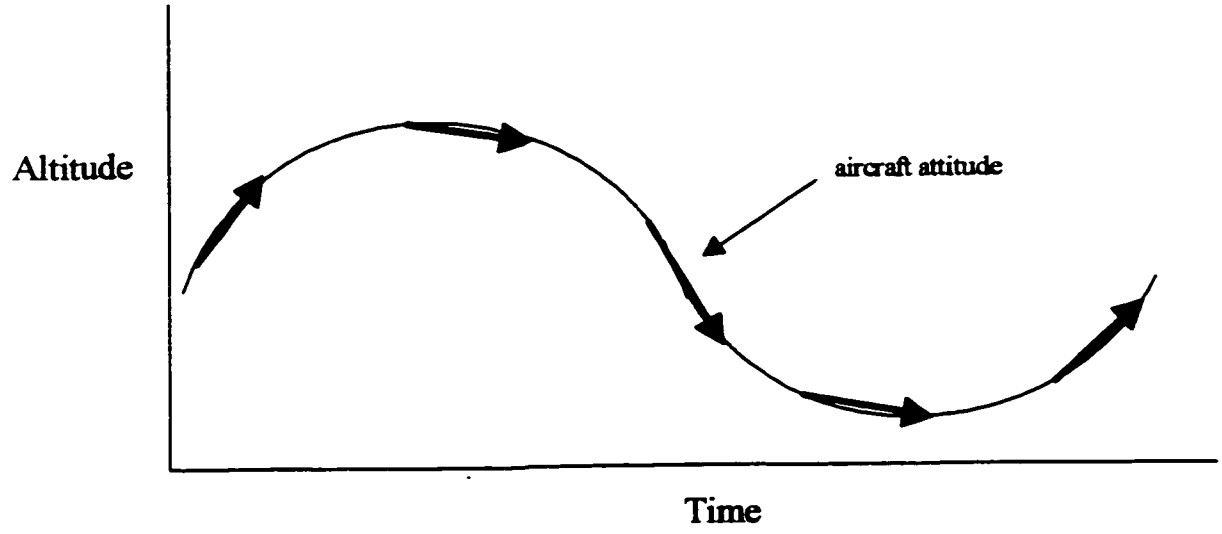

Figure 4.9 Long period mode dynamics (arrows represent longitudinal axis)

the case with the short period mode. The short period mode must be at least moderately damped for the pilot to keep control of the aircraft. The period of oscillation can be calculated as follows:

$$period = \frac{2\pi}{\omega_d} \tag{4.13}$$

where ω_d is the damped natural frequency.

Both phugoid and short period modes are shown to be stable with periods of 10.5 and 2.8 seconds respectively. Non-instrumented flights of the OHS experimental aircraft visually displayed a stable long period mode of roughly 10 seconds, showing good correlation to the theoretical model.

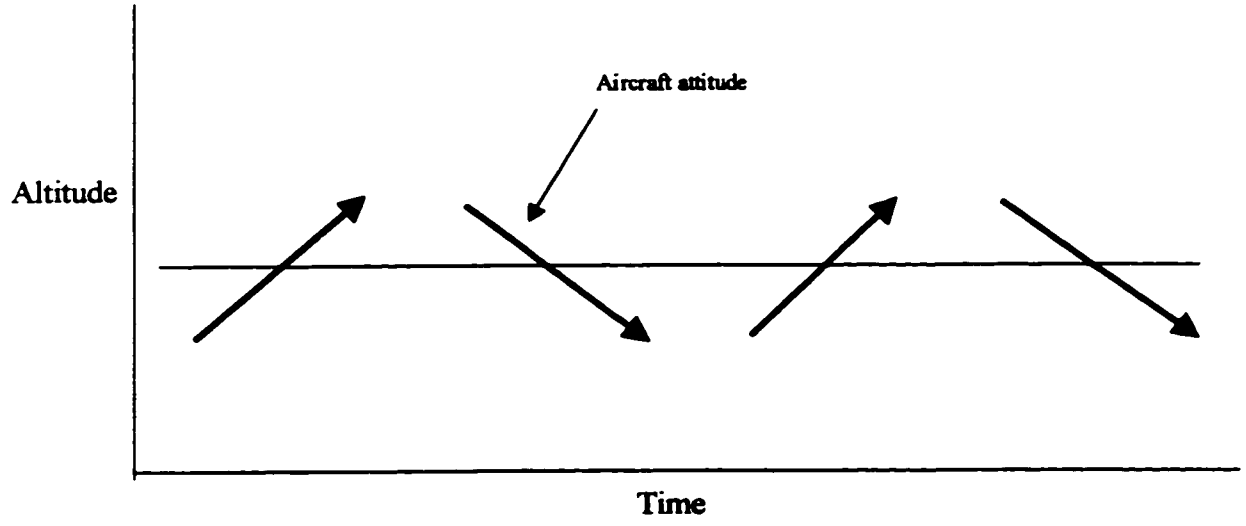

Figure 4.10 Short period mode dynamics (arrows represent longitudinal axis)

4.7 Summary

The OHS aircraft is modelled using an analytical method developed by Dommasch et al [9]. The method was modified to take into account the differences in the OHS aircraft from a conventional aircraft. The Dommasch method is based on Newton's second law where aerodynamic forces and moments are summed about the center of gravity of the aircraft. A non-linear fifth order model including elevator as the input, and velocity, angle of attack, pitch, pitch rate, and altitude as the outputs, is developed. The model is linearized about a nominal operating condition to aid in controller development. The model is then validated by analyzing the long and short period modes and studying the stability of those modes.

Chapter 5
Classical Feedback Control

5.1 Introduction

Once a model is developed, it is necessary to define the performance specifications and choose a controller type to meet those specifications. The performance specifications will often evolve with the design process. As the knowledge base is built up with experimentation and analysis, a better understanding of the system (i.e. strengths and weaknesses) will emerge. At this point in time, an improvement in the aircraft's response to disturbances is desired. This will result in better tracking performance and a smoother flight path. The theoretical model shows a lightly damped, long period mode. The first objective is to increase the damping of the phugoid oscillation and increase the speed of response.

5.2 Control Theory

One of the simplest forms of control is proportional only control. The single input single output (SISO) feedback control system is shown in Figure 5.1 with elevator as the input and pitch as the output.

The system is defined in state space as:

$$\dot{x} = Ax + Bu \tag{5.14}$$

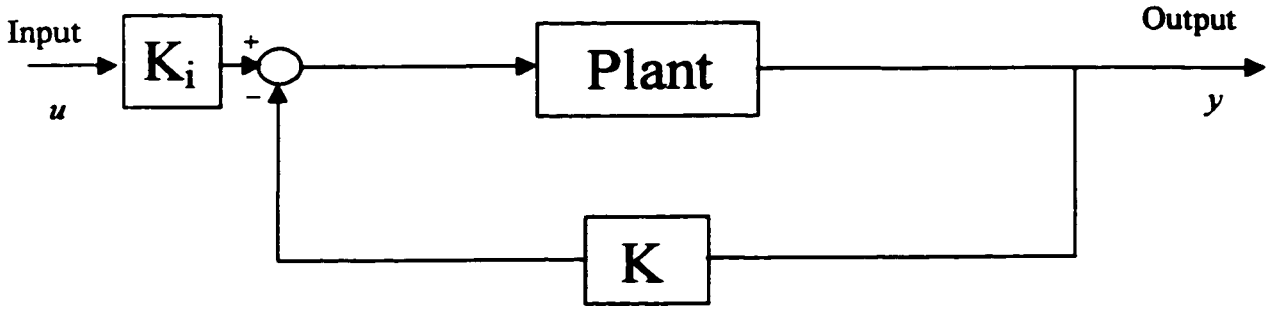

Figure 5.1 Proportional feed back diagram

$$y = Cx + Du \tag{5.15}$$

for the state vector $x = \begin{bmatrix} v & \alpha & \theta & \dot{\theta} & h \end{bmatrix}^T$, input $u = [elev]$, output $y = [\theta]$, and system matrices A, B, C, D. The feedback is added to the system according to the control law:

$$u = -Ky \tag{5.16}$$

where K is the proportional control gain.

The effects of the application of proportional feedback can be seen in a root locus diagram. The closed loop poles, from the analytical model developed in Chapter 4, are shown in Figure 5.2 with control gains varying from zero to infinity. According to the root locus plot, the addition of proportional feedback will increase the damping and speed of response of the OHS aircraft system.

5.3 Computer Simulation

The open and closed loop modelled system was simulated in Matlab [31]. An elevator doublet signal, consisting of a full scale deflection of 20 degrees in both directions for a duration of 1.5 seconds, was used to excite the system. The fifth order system model de-

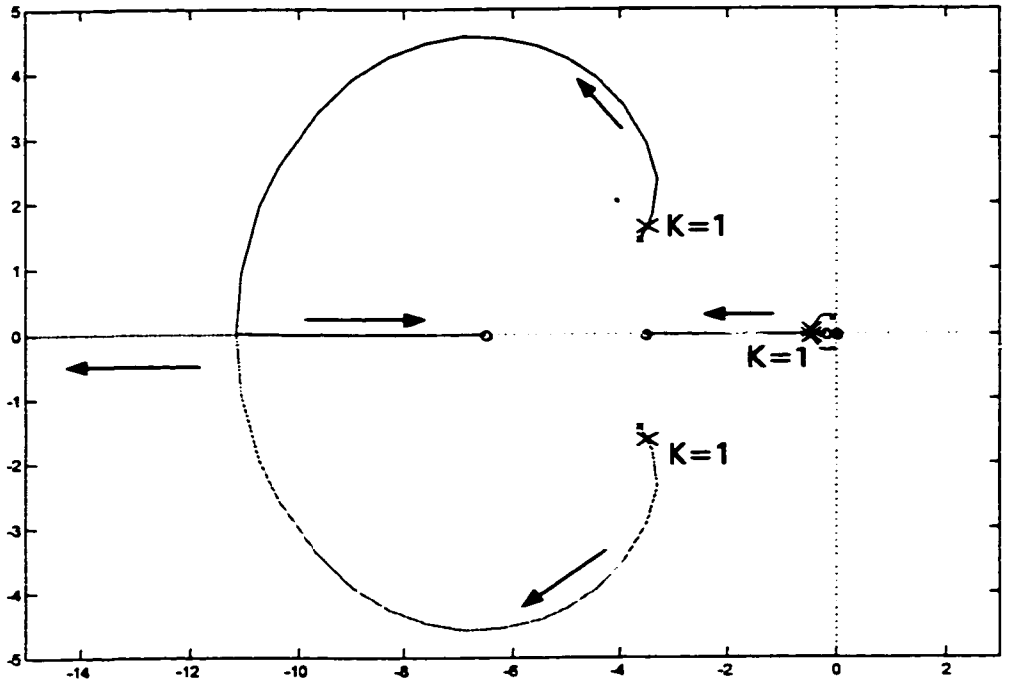

Figure 5.2 Root locus diagram for proportional only control applied to the fifth order analytical model

veloped in Chapter 4 with elevator as the input and velocity, angle of attack, pitch, pitch rate, and altitude as the outputs.

Figure 5.3 shows the open loop simulation of the OHS aircraft model. The response shows a lightly damped system which is in agreement with the open loop poles depicted in the root locus diagram in Figure 5.2. The open loop system has a period of oscillation of 10.5 seconds and a settling time of roughly 40 seconds.

Proportional feedback was added to the aircraft simulation with the same elevator doublet used as the excitation signal. A proportional feedback control gain was set to $K = 1$ and the response is shown in Figure 5.4. The control action moved the system poles

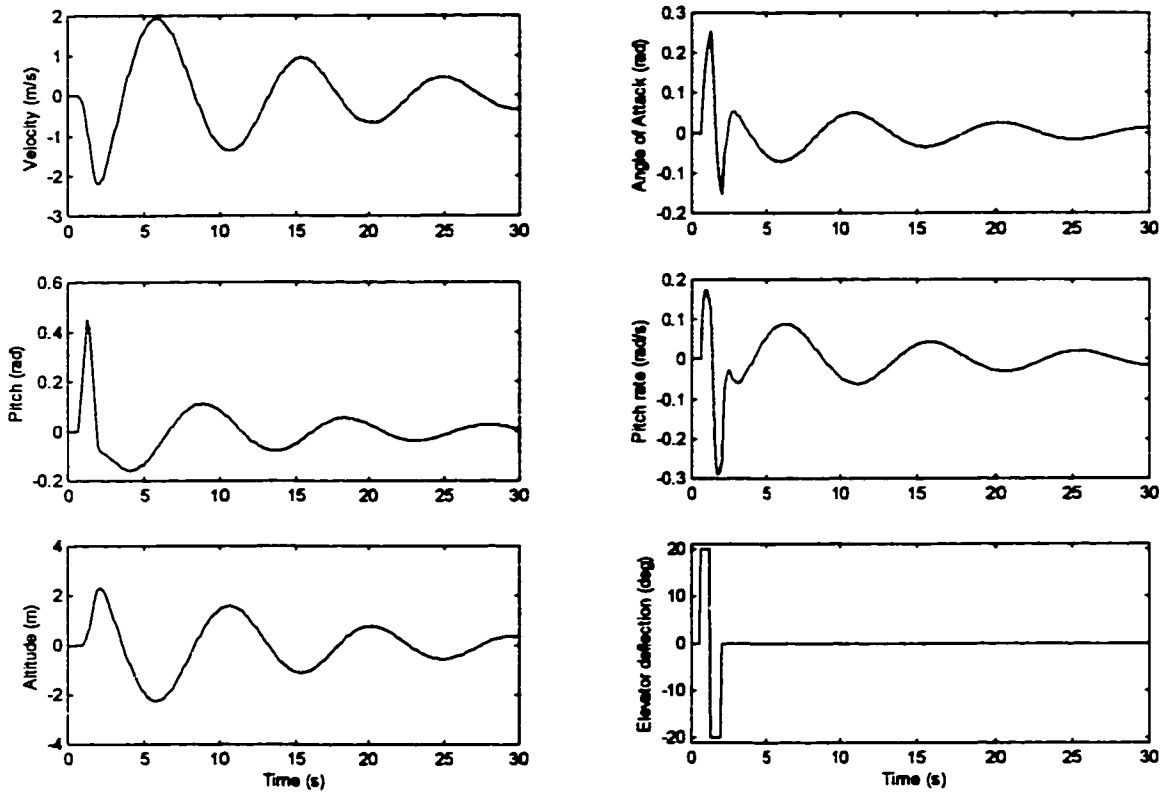

Figure 5.3 Simulated open loop response to an elevator doublet

to the new values of -3.44 ± 2.48 ($\omega_n = 4.24\ rad/s$, $\zeta = 0.81$) for the short period mode and -0.326 ± 0.737 ($\omega_n = 0.81\ rad/s$, $\zeta = 0.40$) for the long period mode. The aircraft system settles to its steady state value within 10.5 seconds following the completion of the excitation signal. According to the simulation, this small addition of proportional feedback has greatly reduced the settling time and increased the damping of the OHS aircraft.

Another form of feedback is proportional plus derivative (PD) control. Not only is the scaled output signal fed back but the scaled derivative of the output signal is also fed back. PD control gives more authority over the poles in the closed loop system by

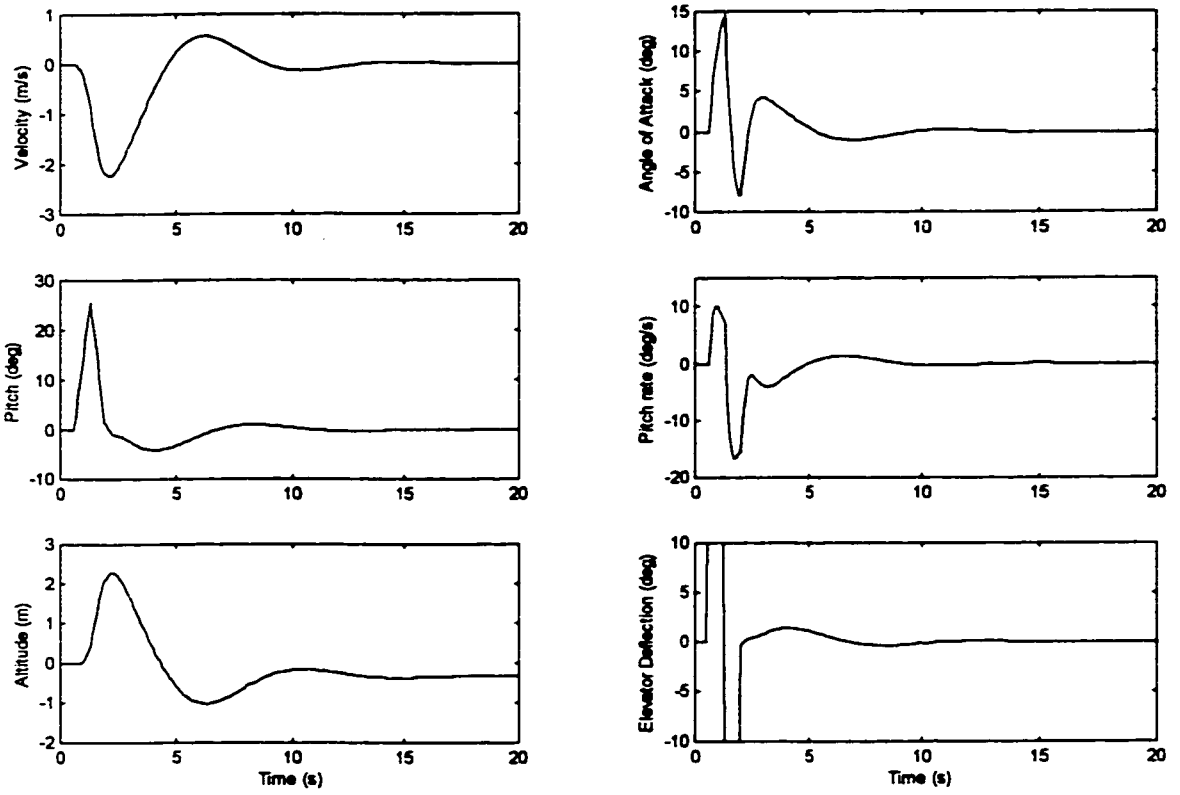

Figure 5.4 Simulated proportional only feedback response to an elevator doublet

adding a second degree of freedom to the system. This can be extended to the case where there are enough feedback control variables to individually place every pole in a desired location. This is generally called the pole placement method. A simplified root locus diagram is shown in Figure 5.5 where $K_{pd} = K(1+s)$. Note that the ratio of proportional and derivative control gains is fixed in order to generated a root locus diagram.

Figure 5.6 shows a simulation of the elevator doublet response to the OHS aircraft with PD control. Both the proportional feedback gain K_p and the derivative feedback gain K_d were set to one. The settling time has been reduced to 8.5 seconds from 10.5

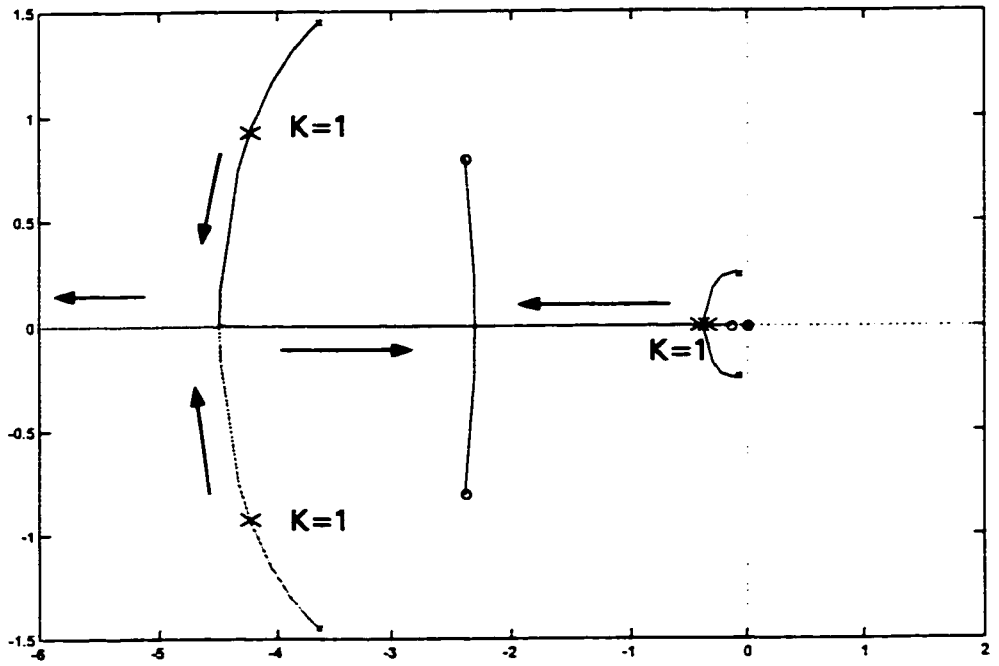

Figure 5.5 Simplified root locus for the PD controller

seconds with the addition of derivative feedback control. The closed loop poles have been repositioned to -3.97 ± 1.15 ($\omega_n = 4.13\ rad/s, \zeta = 0.96$) and -0.395 ± 0.54 ($\omega_n = 0.67\ rad/s, \zeta = 0.59$) respectively for the short and long period modes.

5.4 Experimental Results

Most of the remote controlled flight tests were conducted in the summer of 1999 at the abandoned South Calgary Airport. The OHS aircraft was flown by an experienced RC pilot (Scott Rollefstad) for aircraft safety and reliability considerations. All flight test runs were performed into wind at various airspeeds and at an altitude of about 40 m. A small

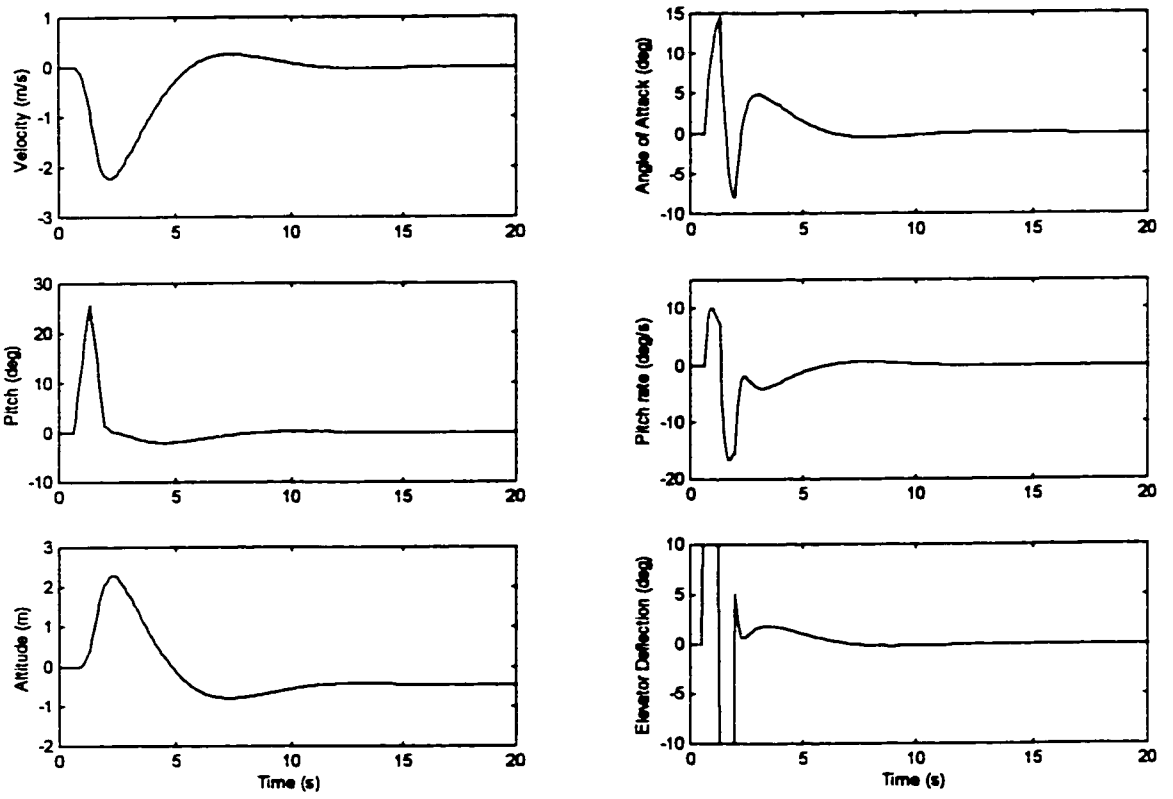

Figure 5.6 Simulated proportional plus derrivative feedback response to an elevator doublet

amount of air turbulence was present for most of the experiments despite efforts taken to fly on calm windless days.

Figure 5.7 shows the open loop elevator doublet response. The excitation signal is the same full scale deflection of the elevator to an angle of 20 degrees, in both directions, for a total of 1.5 seconds (full up for 0.75 seconds followed by full down for 0.75 seconds). The open loop response has a period of oscillation of 7.5 seconds which is almost fully damped

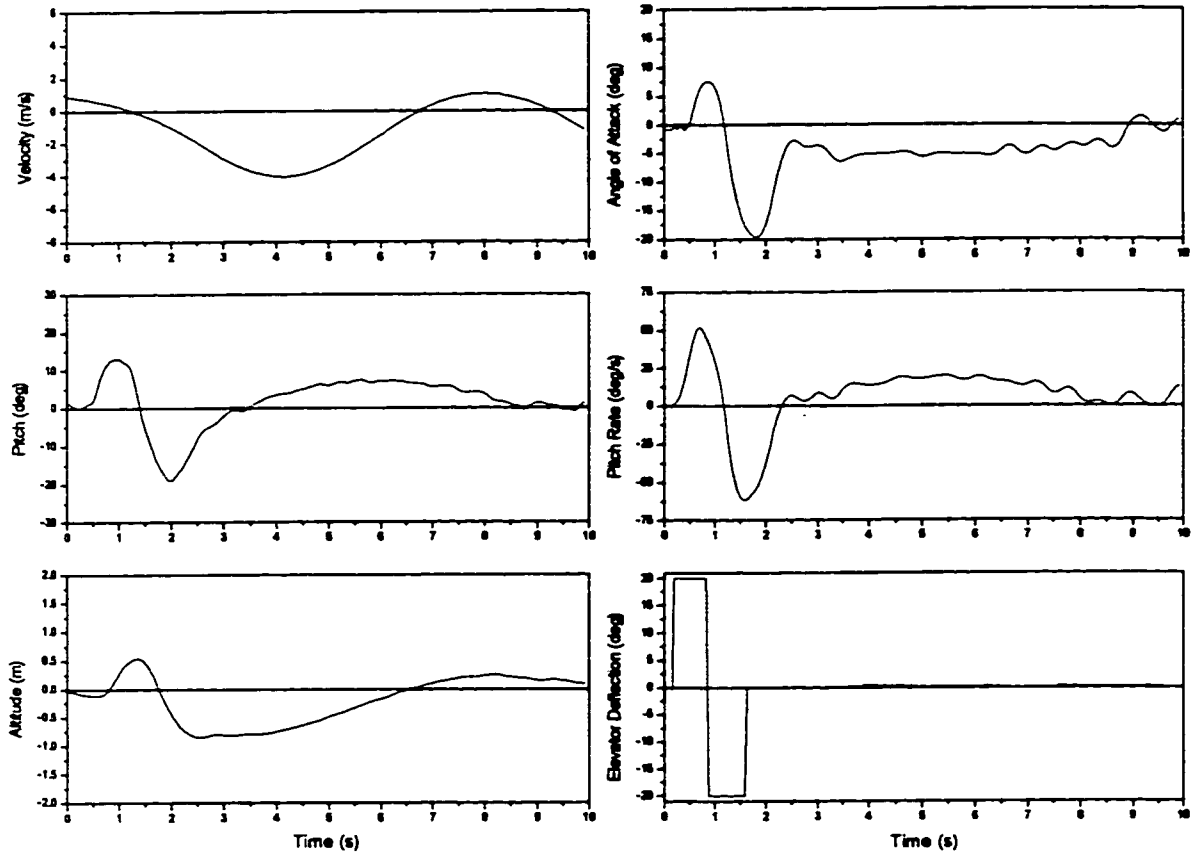

Figure 5.7 Experimental open loop response

out after completing the first post excitation signal cycle. The experimental aircraft system is fairly close to the analytical model except for the increased amount of apparent damping.

Proportional feedback was then applied to the experimental OHS aircraft. The feedback gain ($K = 1$) was chosen to coincide with the computer simulations. Figure 5.8 depicts the response of the aircraft with the addition of proportional feedback. The response shows a marginally stable system when in fact, according to the numerical model,

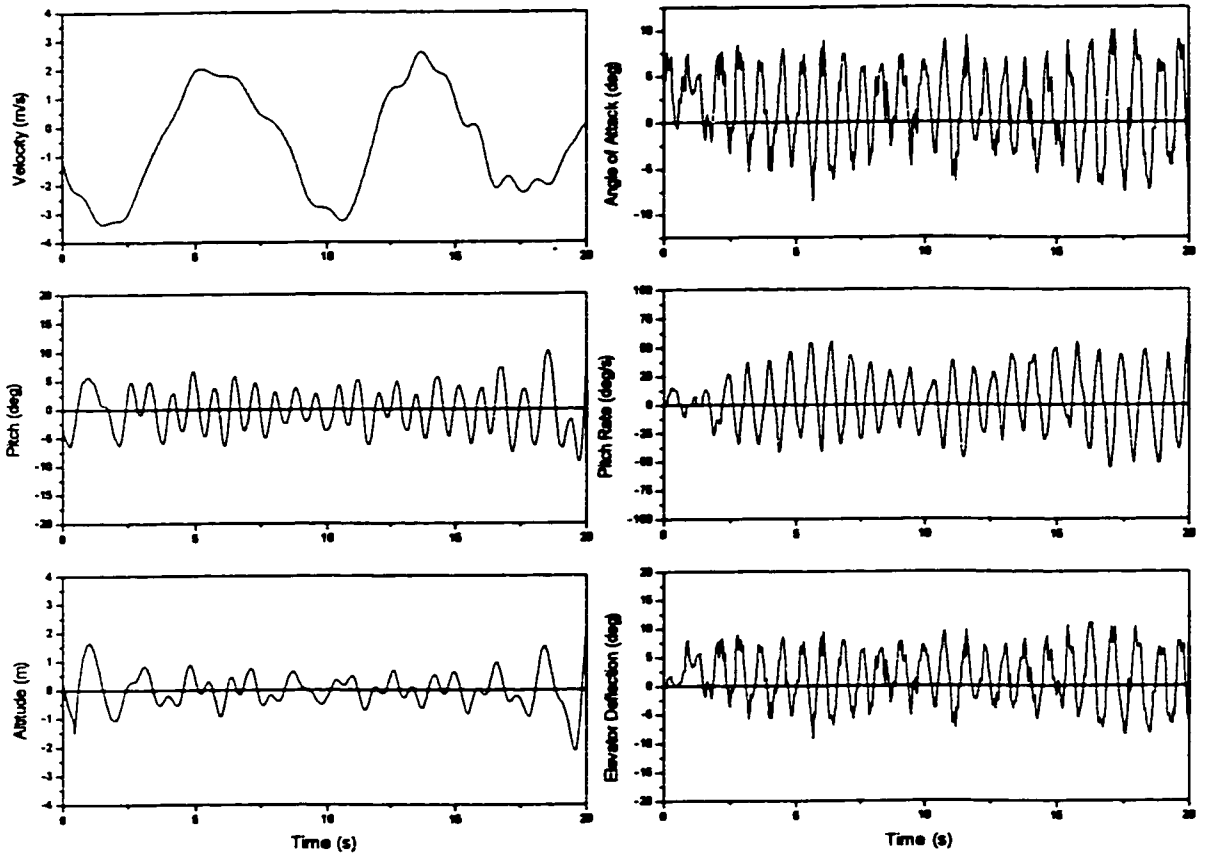

Figure 5.8 Experimental flight test showing the effects of proportional only feedback

a very stable moderately damped system should exist. The elevator doublet signal was not used to excite the aircraft in this case. The aircraft simply started into a constant oscillation that continued until the controller was disengaged. It is evident that a discrepancy exists between the analytical model and the experimental aircraft. It would appear that proportional only feedback is inappropriate.

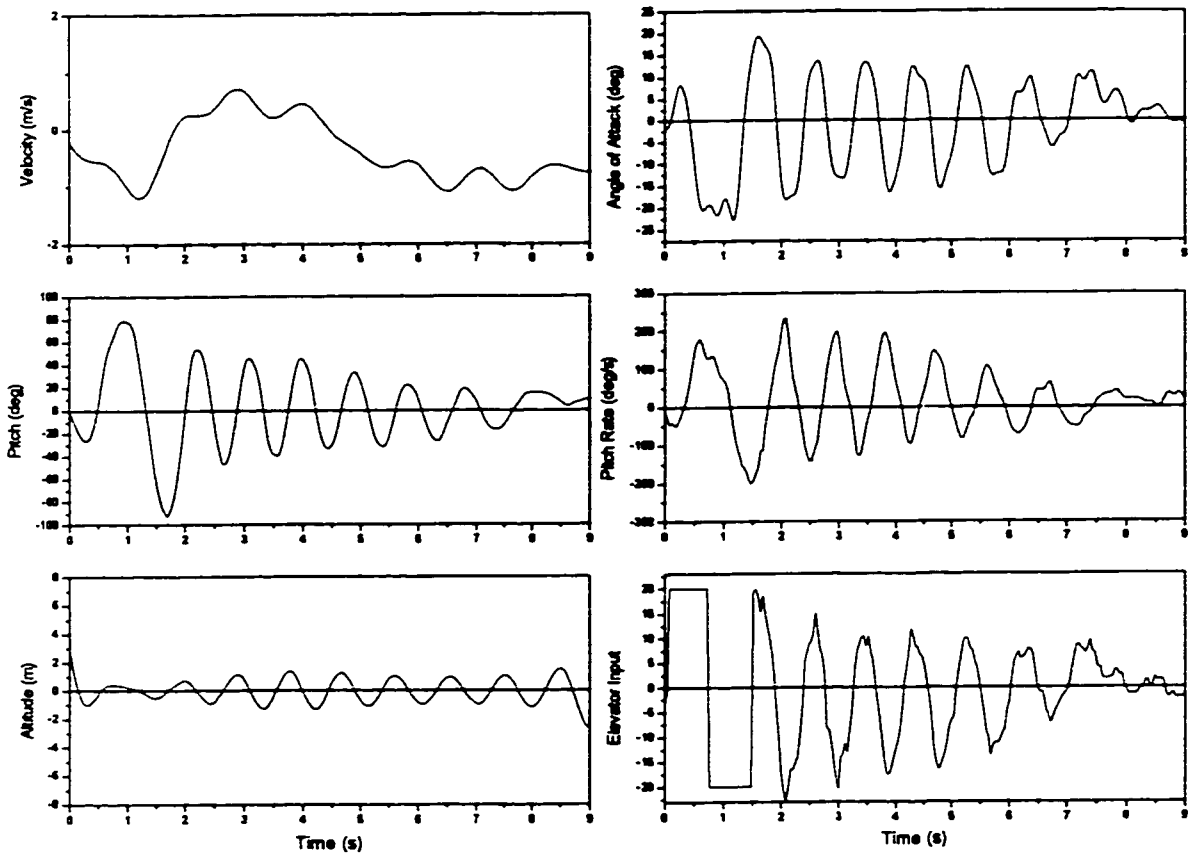

Figure 5.9 Experimental elevator doublet response using PD feedback

The next step was to apply PD control to the experimental model. Figure 5.9 shows the experimental elevator doublet response to PD feedback control. Both the proportional and derivative gains were set to one. The response has improved from the marginally stable condition with proportional control to a lightly damped state. The aircraft reaches a steady state condition nine seconds following the completion of the excitation signal, although, seven diminishing oscillation cycles occur before doing so. This is not considered

as a good flying characteristic. Tuning of the PD controller will most likely improve the response of the system, although, no further time was spent investigating other PD controllers.

5.5 Summary

Examined in this chapter is the application of simple feedback control to the OHS aircraft. The proportional only controller and the PD controller are developed for the OHS aircraft. First, a root locus analysis is done to check the suitability of the proportional only controller. The root locus diagram shows that the application of proportional control would lead to a stable system with good dynamic characteristics. The controller is then simulated in Matlab [31] using a feedback gain of one. The response shows good results. Next, a PD controller is tried in simulation and the system response improved further, decreasing the settling time from 9.5 to 7.5 seconds.

The controllers are then implemented on the experimental aircraft model. The results are not indicative of the computer simulations. The proportional only controller gives a marginally stable system and the PD controller results in a stable system but with high frequency oscillations occurring before being damped out in 7.5 seconds. This is not an adequate response for the OHS aircraft, however, tuning of the PD controller would probably result in a favorable response. PD control was nonetheless dropped in favor of optimal control. The discrepancy between the simulation and experiments indicate that, in this situation, the model does not accurately represent the actual aircraft.

Table 5.1 shows the simulated and experimental cost functions (see Chapter 7) for P and PD controllers applied to the OHS aircraft. The simulation results for the P and PD

Control	q	Simulated	Experimental
P	0.1	0.24	7930
P	1	2.41	75228
P	10	24.04	748210
PD	0.1	0.31	8713
PD	1	3.11	81693
PD	10	31.06	811490

Table 5.1 Cost function J for various P and PD controllers

controllers indicate that the cost function increase roughly by a factor of ten with increasing q. The Experimental results for both the P and PD controllers show similar trends even though the magnitudes of the experimental values are greater than that of the simulations. The differences in magnitude between the simulated and experimental results could be due to the fact that the experimental data contains noise as well as non-zero steady-state end points. Also, both the simulation and experimental results show that the P controller has a relatively smaller cost function than that of the PD controller.

Chapter 6
Linear Quadratic Optimal Control

6.1 Introduction

Since the control objectives were not achieved with the application of proportional, or proportional plus derivative control, a more complex control approach will be attempted. The thrust of this chapter deals with the design and implementation of a linear quadratic optimal controller (LQOC) for the OHS RC aircraft. The controller was first simulated in Matlab [31] using the theoretical model, and then implemented on the aircraft during the flight test phase.

6.2 Control Theory

Linear Quadratic Optimal Control [3] is favorable here considering the availability of state feedback based on the theoretical model developed in Chapter 4. The use of an observer is therefore not warranted. This control scheme is based on the H_2 energy minimization criterion. The objective is to minimize the "energy" of the signal error giving optimal nominal performance, as opposed to the case of H_∞ control where the "worst case" signal error is minimized resulting in optimal robust stability. The control scheme is designed around the state space system

$$\dot{x} = Ax + Bu. \tag{6.17}$$

The LQOC technique calculates the optimal gain matrix K in the control law $u = -Kx$ in order to minimize the cost function

$$J = \int_0^\infty \left(x^T Q x + u^T R u\right) dt \tag{6.18}$$

where x and u are the system states and inputs respectively and $Q = q \cdot I$ and $R = r$ are weighting matrices that dictate the amount of control used. The larger the ratio of q/r the greater the control action. The choice of these weighting matrices is based on performance criteria and available actuator limits. The optimal control gain K for any given q and r is calculated by solving the following Riccati equation for P

$$A^T P + PA - BPR^{-1}PB^T - Q = 0 \tag{6.19}$$

and then solving for the controller gain K

$$K = -R^{-1}B^T P. \tag{6.20}$$

The optimal control gain was determined using Matlab [31].

6.3 Computer Simulation

The control system was simulated on the computer with Matlab. Various q and r values were used in the simulations to allow for differing performance specifications as well as to show the effects of adjusting these variables on the aircraft control system.

Simulations were conducted using an elevator doublet as the excitation signal. The elevator doublet is a full scale ($\pm$ 20 degrees) deflection of the elevator in both directions

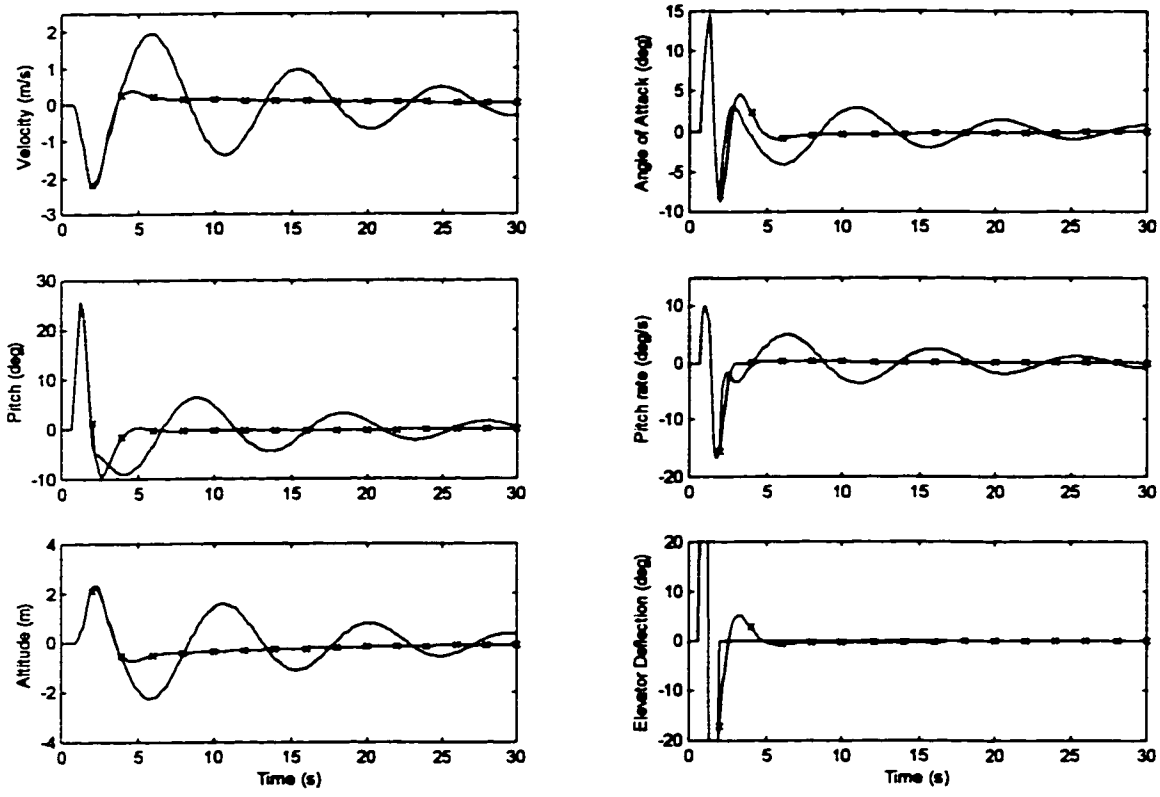

Figure 6.1 Open loop simulation (solid) and closed loop simulation (–x–x–x–) (q/r=1)

for a total duration of 1.5 seconds (0.75 seconds in each direction). Figure 6.1 shows the longitudinal response of the linearized mathematical model. The five measured states as well as the elevator control input are plotted for the open loop (solid) and closed loop (–x–x–x–) cases. The open loop long period mode (damped natural frequency) of the mathematical model is shown to be 9.5 seconds in Figure 6.1. A damping ratio of 0.11, calculated in Chapter 4, is evident in the slow decay of the oscillation. The highly damped short period mode is not apparent in the graphs, although it is calculated as 2.8 seconds from the mathematical model developed in Chapter 4.

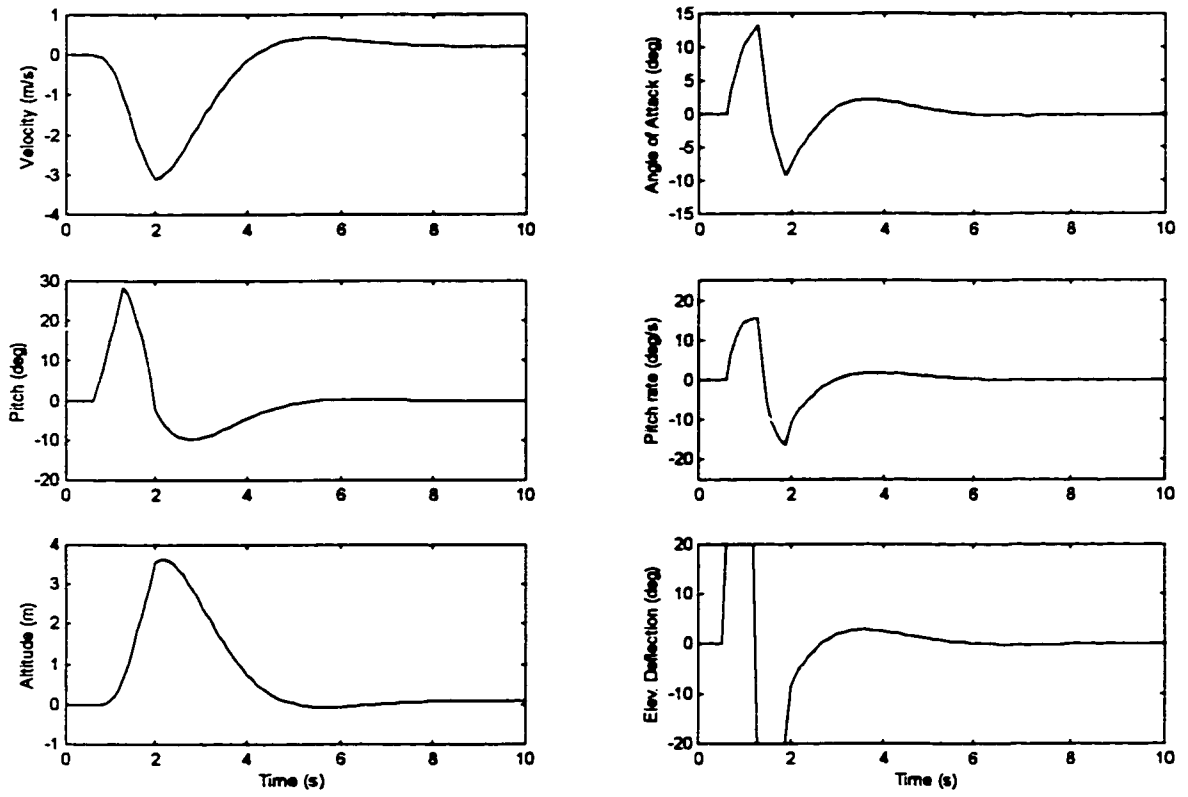

Figure 6.2 Closed loop simulation with q/r=0.1

The closed loop response of the mathematical model is also plotted in Figure 6.1. Adding the LQOC as feedback to the system makes a dramatic improvement to the overall response. The closed loop system reaches the steady state condition within two seconds of the completion of the excitation signal. The long period poles have also shifted from -0.07 ± 0.66 ($\omega_n = 0.66\ rad/s$, $\zeta = 0.11$) to -2.0 ± 2.2 ($\omega_n = 2.97\ rad/s$, $\zeta = 0.67$) explaining the quicker response and increased damping.

The closed loop simulations were also conducted with a number of weighting conditions. Adjustments to the ratio of weighting matrices dictates the amount of control used.

A controller designed with a large Q/R ratio will use more control than one with a smaller q/r. The closed loop response depicted in Figure 6.1 used $q = 1$ and $r = 1$.

Figure 6.2 shows the closed loop simulated response with $q = 0.1$ and $r = 1$. Note that the scales on the closed loop graphs have been adjusted for clarity. The long period poles have now moved to -1.1 ± 1.3 ($\omega_n = 1.70\ rad/s$, $\zeta = 0.65$). The damping is slightly lower and the damped natural frequency is slower than the previous closed loop response as expected. The poles are less effected due to the smaller control gains. The result is a slower responding system with poorer tracking characteristics.

Figure 6.3 shows the closed loop response of the mathematically modeled system with the weighting matrix $q = 10$ and $r = 1$. The long period closed loop poles are at -2.6 ± 3.3 ($\omega_n = 4.20\ rad/s$, $\zeta = 0.62$) for this case giving a faster system response. The tracking is improved over the previous cases with the increase in control gains.

The poles of the closed loop system with various values of the weighting matrices are shown in Figure 6.4. The poles start at the right for low control gains (small Q/R ratio) and proceed to the left with ever increasing control. Note that the damping ratio of the long period poles remain almost constant throughout the range of values. However the natural frequency of the dominant poles increase steadily with increasing control.

The results are based on the controller design for a linearized numerical model. The results of adjusting controller gains on the physical aircraft may differ from the simulations. Therefore, one must conduct flight experiments to validate the theoretical results.

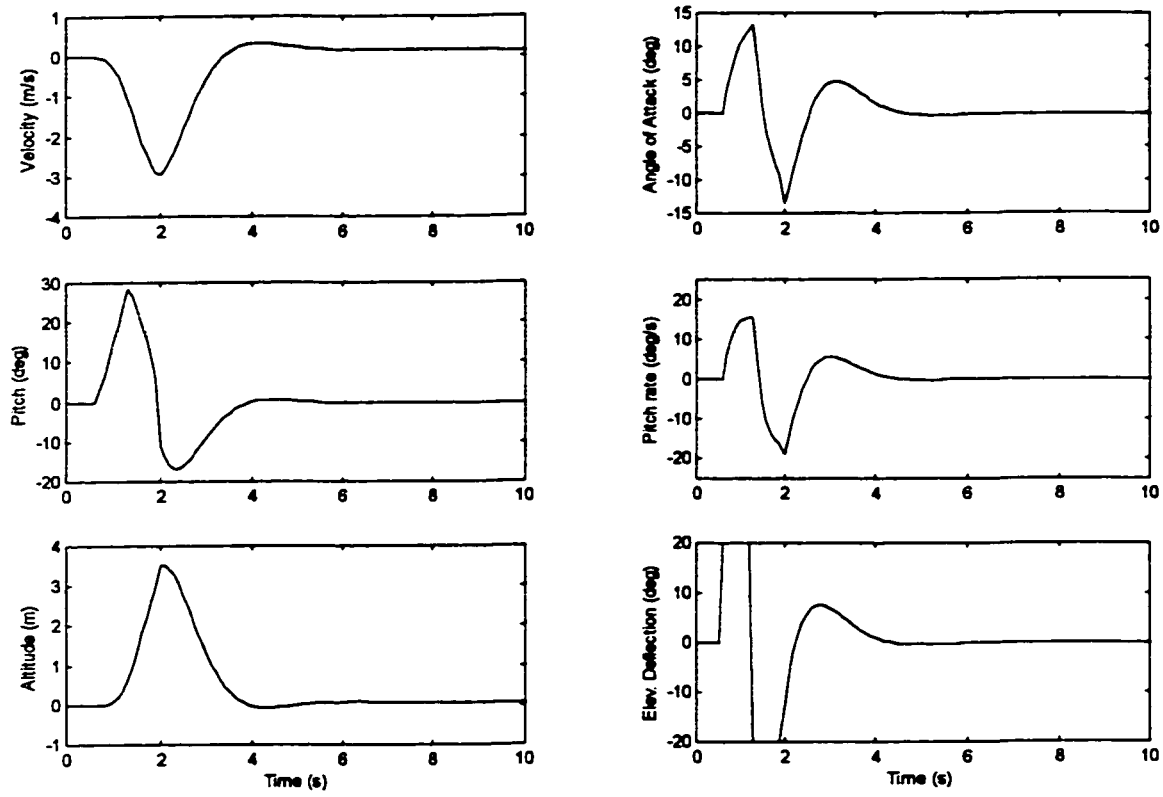

Figure 6.3 Closed loop simulation with q/r=10

6.4 Experimental Flight Results

Following from the computer simulations, a similar set of experiments were carried out on the remote controlled OHS aircraft. The input or excitation signal was an elevator doublet of near full scale deflection. An angle of ±20 degrees was used as the elevator excitation amplitude for a total period of 1.5 seconds. The elevator input signal was scaled on the following graphs giving the amplitude of the elevator doublet equal to one. During the flight experiments the excitation signal was performed in an open loop control config-

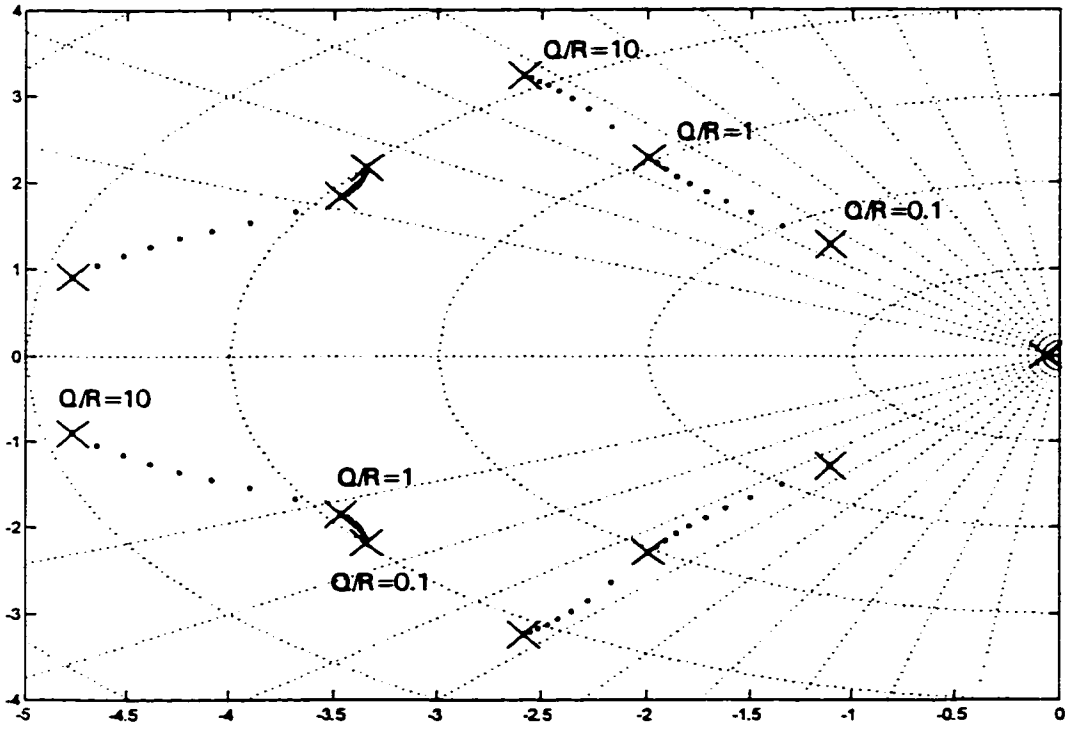

Figure 6.4 Pole positions with various q/r ratios

uration. The LQR controller was deactivated for the duration of the elevator doublet to ensure similar initial conditions for all the flight experiments. The computer simulations were conducted in the same manner.

Figure 6.5 depicts the open loop response to the elevator doublet excitation signal. A long period mode of about 7.5 seconds is close to the simulated open loop dominant mode of 9.5 seconds. The damping is slightly higher in the physical aircraft. Oscillatory motions are almost fully damped out shortly after the completion of the first post excitation cycle.

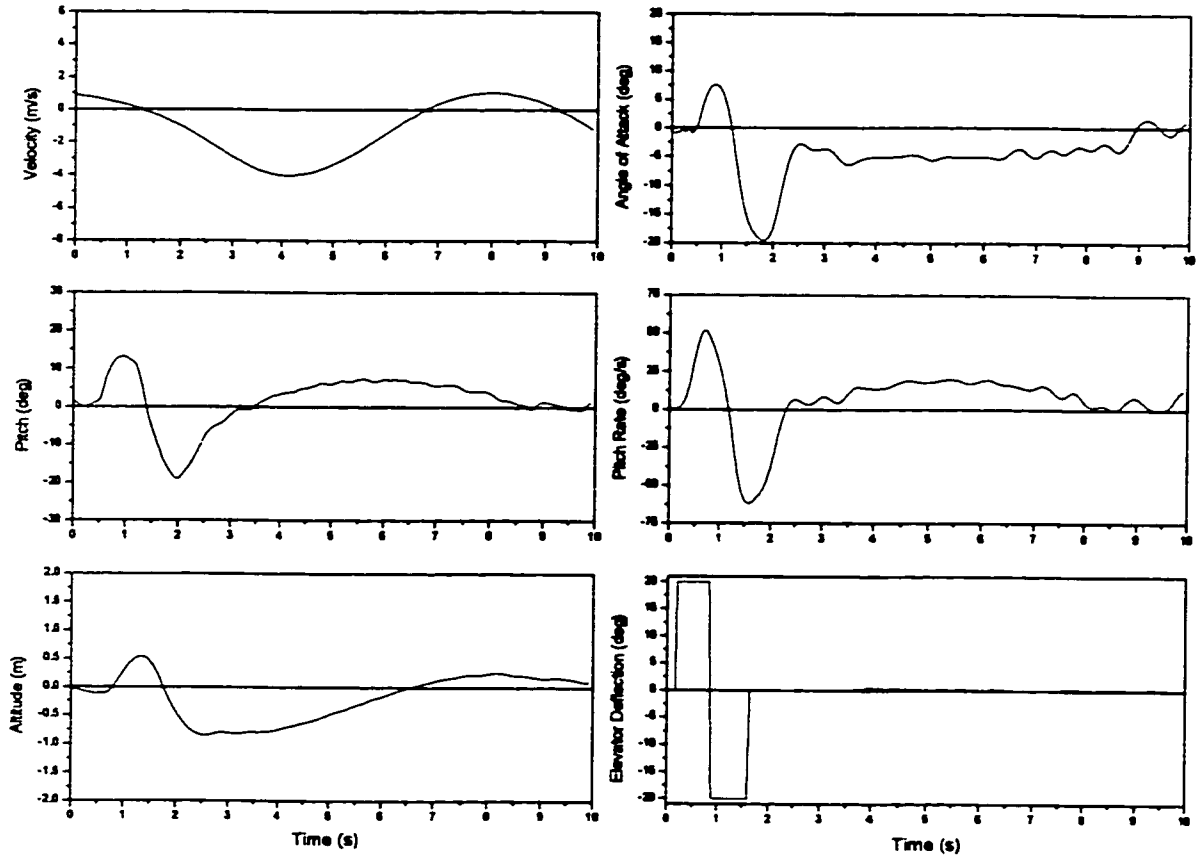

Figure 6.5 Open loop experiment

LQR control was then added to the aircraft system to modify the response. Figure 6.6 shows the closed loop response of the OHS aircraft with the weighting matrices chosen to give small controller gains. The weighting values are $q = 0.1$ and $r = 1$ as in the computer simulation. The response is forced to steady state in 3.0 seconds following the excitation signal similar to the closed loop simulation in Figure 6.2. All oscillations have been damped out resulting in a much faster response than the open loop system.

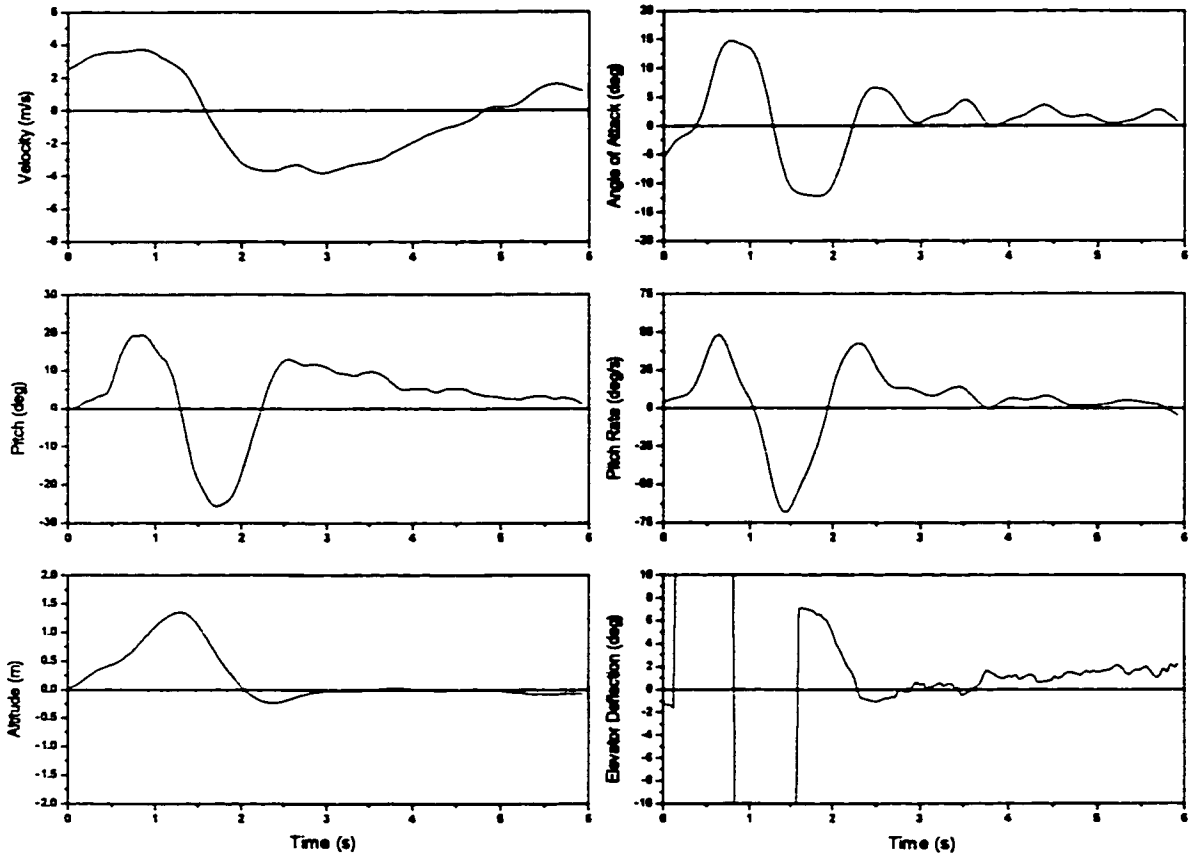

Figure 6.6 Closed loop experiment with q/r=0.1

The angle of attack, pitch, pitch rate, and altitude all show dramatic differences with the addition of LQR control. The computer simulation (Figure 6.2) shows a substantially quicker response in velocity, yet the experimental velocity measurement is much less affected by the control action. This is partly due to the time constant of the velocity sensor. The anemometer is a propeller driven DC motor with an output voltage signal proportional

to airspeed. The aerodynamic and inertial effects slow the response of the motor-propeller system and is therefore unable to detect the relatively fast changes in airspeed.

The weighting matrices were adjusted to give more aggressive control as depicted in Figure 6.7. Again, a q/r ratio of 10 was chosen corresponding to the computer simulation. The system response time is slightly longer than the theoretical value. Here, the system reaches steady state in 1.5 seconds following the excitation signal. The computer simulation reached steady state in just over 3.0 seconds following the completion of the elevator doublet. Figure 6.7 does show a faster response with the higher control gains than the previous graph with the smaller control gains. This is apparent in both the experimental and theoretical situations.

6.5 Summary

A Linear Quadratic Optimal controller was designed for the OHS aircraft based on the mathematical model. Open and closed loop computer simulations were conducted to analyze the response of the mathematical model and to aid in controller design. Finally, the controller was implemented on the physical aircraft in a series of open and closed loop experiments.

Overall, the experimental results are in correspondence with the theoretical analysis of the mathematical model. The open loop response of the theoretical and experimental system had long period modes of 9.5 and 7.5 seconds respectively. The closed loop theoretical and experimental response also showed comparable reductions in settling time and variations due to controller design modifications.

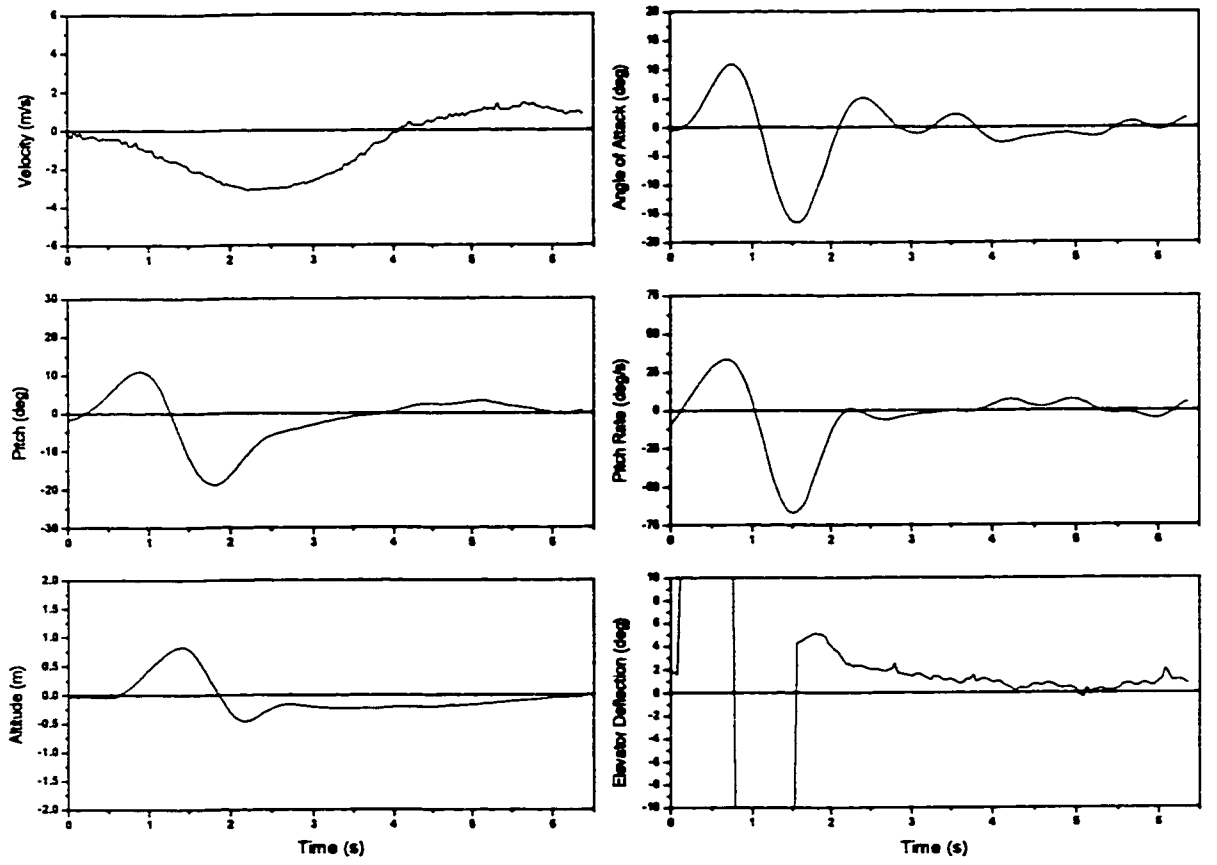

Figure 6.7 Closed loop experiment with q/r=10

The linearized mathematical model is therefor a good representation of the physical aircraft at the nominal operating condition of 11 m/s. Table 6.1 shows the simulated and experimental cost functions (see Chapter 7) for the LQR controllers.

The simulation results show an increase in J by a factor of 24.7 with an increase in q. The experimental values are in reasonable correspondence with a multiplying factor of 53.3 between the different q cases.

q	Simulated	Experimental
0.1	0.027	193
10	0.668	10289

Table 6.1 Cost function J for various LQR controllers

Chapter 7
Optimal Output Cost Function

7.1 Introduction

The solution for an output feedback controller allows for a reduction in the number of measured states. Optimal, in a linear quadratic sense, feedback control provides an analytic solution for a minimum energy closed loop system, as measured by a given cost function [25]. A reduction in the feedback states results in a savings in sensor and computational costs and complexity.

The simulation results for the design of a control system for the OHS aircraft is shown. The reduction in the complexity of the feedback system, by the elimination of certain feedbacks, does not significantly degrade performance of the closed loop system. An evaluation is made of which states may be removed from the feedback structure resulting in acceptable degradation in performance as measured by the cost function.

7.2 Optimal Output Feedback Controller Design

The discrete time dynamic system to be controlled is assumed to be linear time invariant with n states (x_k), m controls (u_k) and p measured outputs (y_k):

$$x_{k+1} = \Phi x_k + \Gamma u_k \tag{7.21}$$

$$y_k = C x_k \tag{7.22}$$

This is a sampled data version of the aircraft dynamics from Chapter 4. The design objective is to construct a control sequence so that the cost function:

$$J = \sum_{k=1}^{\infty} (x_k^T Q x_k + u_k^T R u_k) \tag{7.23}$$

is minimized [39]. The control function is limited to a linear combination of the measurements:

$$u_k = -K y_k = -KCx_k \tag{7.24}$$

Substituting the assumed control policy into the cost function gives:

$$J = \sum_{k=0}^{\infty} (x_k^T Q x_k + x_k^T C^T K^T R K C x_k) = \sum_{k=0}^{\infty} x_k^T Q' x_k. \tag{7.25}$$

Expanding this sum gives:

$$J = x_0^T Q' x_0 + x_0^T \Phi_{cl}^T Q' \Phi_{cl} x_0 + \ldots \tag{7.26}$$

$$J = x_0^T S x_0 = tr(S x_0 x_0^T) \tag{7.27}$$

where $\Phi_{cl} = \Phi - \Gamma K C$ and $S = \sum_{k=0}^{\infty} \Phi_{cl}^{Tk} Q' \Phi_{cl}^k$. The state is assumed to have non-zero initial conditions, x_0. From this definition of S, a Liapunov equation for S can be derived. Left multiply by Φ_{cl}^T and right multiply by Φ_{cl} to get:

$$\Phi_{cl}^T S \Phi_{cl} = \sum_{k=1}^{\infty} \Phi_{cl}^{Tk} Q' \Phi_{cl}^k \tag{7.28}$$

Subtract S from both sides:

$$\Phi_{cl}^T S \Phi_{cl} - S = \sum_{k=1}^{\infty} \Phi_{cl}^{Tk} Q' \Phi_{cl}^k - \sum_{k=0}^{\infty} \Phi_{cl}^{Tk} Q' \Phi_{cl}^k \tag{7.29}$$

$$= -Q \tag{7.30}$$

Rearrange and expanding Q' results in:

$$\Phi_{cl}^T S \Phi_{cl} - S + Q + C^T K^T R K C = 0 \tag{7.31}$$

In locating a minimum value for the cost function, the variational Lagrangian:

$$\mathcal{L} = tr(Sx_0x_0^T) + tr([\Phi_{cl}^T S\Phi_{cl} - S + Q + C^T K^T RKC]L^T) \tag{7.32}$$

is formed. The global minimum with respect to the variables S, K and L is located where the partial derivatives of the Lagrangian with respect to each parameter is zeroed. Evaluating the partial derivatives at their optimal values:

$$\frac{\partial \mathcal{L}}{\partial L} = \Phi_{cl}^T S\Phi_{cl} - S + Q + C^T K^T RKC = 0 \tag{7.33}$$

$$\frac{\partial \mathcal{L}}{\partial S} = x_0x_0^T + \Phi_{cl} L\Phi_{cl}^T - L = 0 \tag{7.34}$$

$$\frac{\partial \mathcal{L}}{\partial K} = (RKC - \Gamma^T S\Phi_{cl})LC^T = 0 \tag{7.35}$$

Rearranging this last equation gives:

$$K = R^{-1}\Gamma^T S\Phi_{cl} LC^T[CLC^T]^{-1} \tag{7.36}$$

$$K = R^{-1}\Gamma^T S(\Phi - \Gamma KC)LC^T(CLC^T)^{-1} \tag{7.37}$$

$$K = R^{-1}\Gamma^T S(\Phi LC^T(CLC^T)^{-1} - \Gamma K) \tag{7.38}$$

$$K = [R + \Gamma^T S\Gamma]^{-1}\Gamma^T S\Phi LC^T[CLC^T]^{-1} \tag{7.39}$$

The update of this optimal output feedback gain matrix as a function of S and L is defined as:

$$K_{i+1} = (1 - \alpha_{i+1})K_i + \alpha_{i+1}[R + \Gamma^T S_i\Gamma]^{-1}\Gamma^T S_i\Phi L_i C^T[CL_iC^T]^{-1} \tag{7.40}$$

so that the updated version of the feedback gain, K_{i+1}, is a blending, using the parameter $\alpha_{i+1} \geq 0$, of the previous gain and a new solution found from the current solutions for S_i and L_i which are found using the most recent output feedback, that is:

$$[\Phi - \Gamma K_iC]^T S_i[\Phi - \Gamma K_iC] - S_i + Q + C^T K_i^T RK_iC = 0 \tag{7.41}$$

and:

$$[\Phi - \Gamma K_i C] L_i [\Phi - \Gamma K_i C]^T - L_i + x_0 x_0^T = 0. \tag{7.42}$$

The blending parameter, α_{i+1}, is chosen so that approach to the optimal minimum J is continued. That is so that J is always chosen smaller than its previous value. Such an α_i will exist by the Pontryagin minimum principle since the cost function is quadratic in the states. The minimum J is found from:

$$J_{i+1} = J_{i+1}(S_{i+1}, L_{i+1}, K_{i+1}, \alpha_{i+1}) \leq J_i = tr(S_i x_0 x_0^T) \tag{7.43}$$

7.3 Application to the OHS Aircraft

The Longitudinal dynamics of the OHS aircraft were modelled in Chapter 4 as a single input five output system. In actuality, there are only four independent outputs since altitude is simply a scaler multiple of two other outputs: pitch and angle of attack. For this reason, altitude will be left out of this examination.

The linear system to be controlled is:

$$\dot{x} = Ax + Bu \tag{7.44}$$

where:

$$x = \begin{pmatrix} velocity \\ angle\ \ of\ \ attack \\ pitch \\ pitchrate \end{pmatrix}, u = (elevator) \tag{7.45}$$

The system is to be intermittently controlled at a rate of 25 Hz. Therefore, in order to design a discrete time controller, the plant matrices were converted via a zero-order-hold

with a sampling time of $T_x = 0.04\ s$. This results in the discrete time system:

$$x_{k+1} = \Phi_k x_k + \Gamma_k u_k \tag{7.46}$$

The controller synthesis problem considers the cost function of Equation 7.23 to be minimized by the choice of some constrained linear feedback of Equation 7.24. The state and control weightings in the cost function were chosen as: $Q = I_4$ and $R = 1$. This results in the states all having equal weightings.

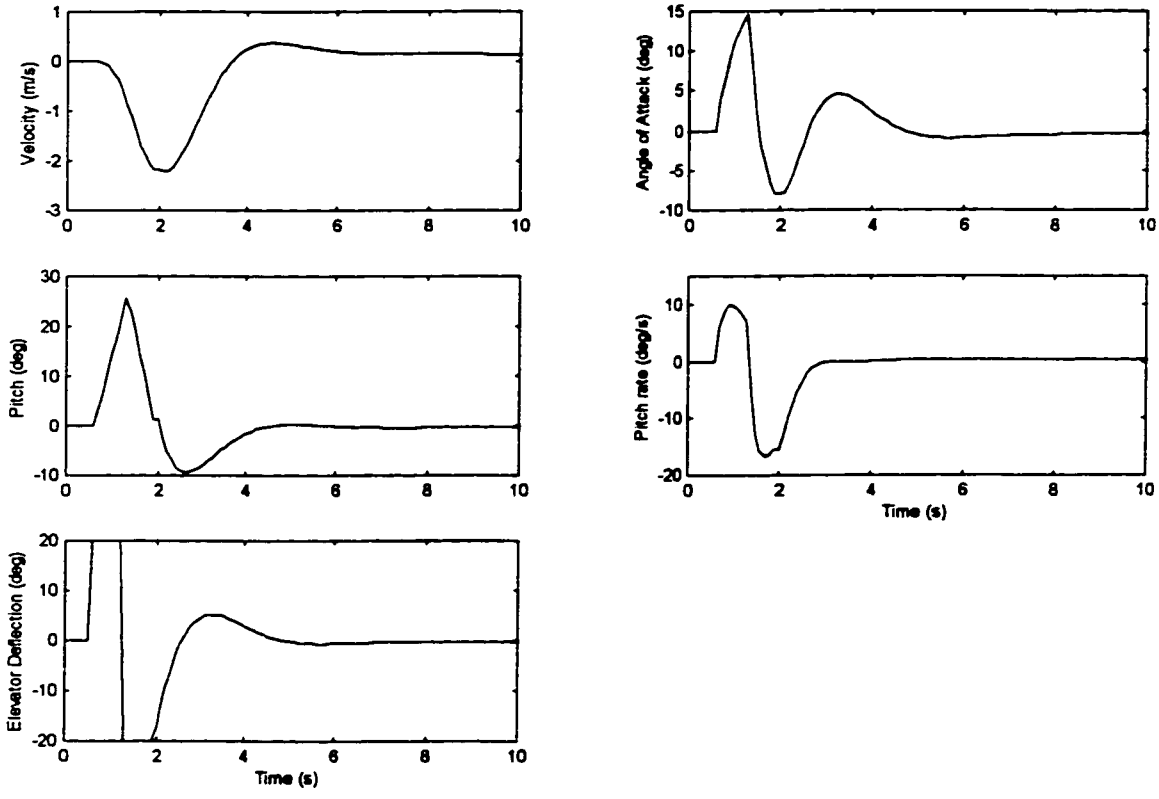

Figure 7.1 Simulated LQR response with full state feedback

The optimal solution for full state feedback was then calculated using the output feedback optimization algorithm to give the state feedback gain matrix:

$$K_{full} = [\ -0.690 \quad -0.705 \quad 3.441 \quad 0.579\ ]. \tag{7.47}$$

This gives a minimum value for the cost function of $J = 8.9531$ corresponding to the initial condition $x_0 = [\ 1 \quad 0.1 \quad 0.1 \quad 0.1\ ]$. Figure 7.1 shows a simulation of the closed loop elevator doublet response using the above controller K_{full}.

Next, all of the states were eliminated except for pitch. The resulting controller is:

$$K_{pitch} = [\ 0 \quad 0 \quad 1.06 \quad 0\ ] \tag{7.48}$$

giving a cost function $J = 13.55$. This is only slightly larger than the cost function for full state feedback and much smaller than the open loop cost function of $J = 244.88$. Table 7.1 shows cost functions for various states removed.

States Eliminated	Cost Function
None	8.9531
Pitchrate	8.9532
Angle of Attack	8.9535
Pitch Rate, A of A	8.9536
Velocity	9.1924
Velocity, A of A,Pitch Rate	13.550
Pitch	27.571
Pitch, A of A, Pitch Rate	171.64
Open Loop	244.88

Table 7.1 Optimal cost function with various states removed

Figure 7.2 depicts the simulated closed loop response with only pitch feedback.The graph shows a small loss in performance. The settling time has increase from four seconds with full state feedback to seven seconds with pitch only feedback.

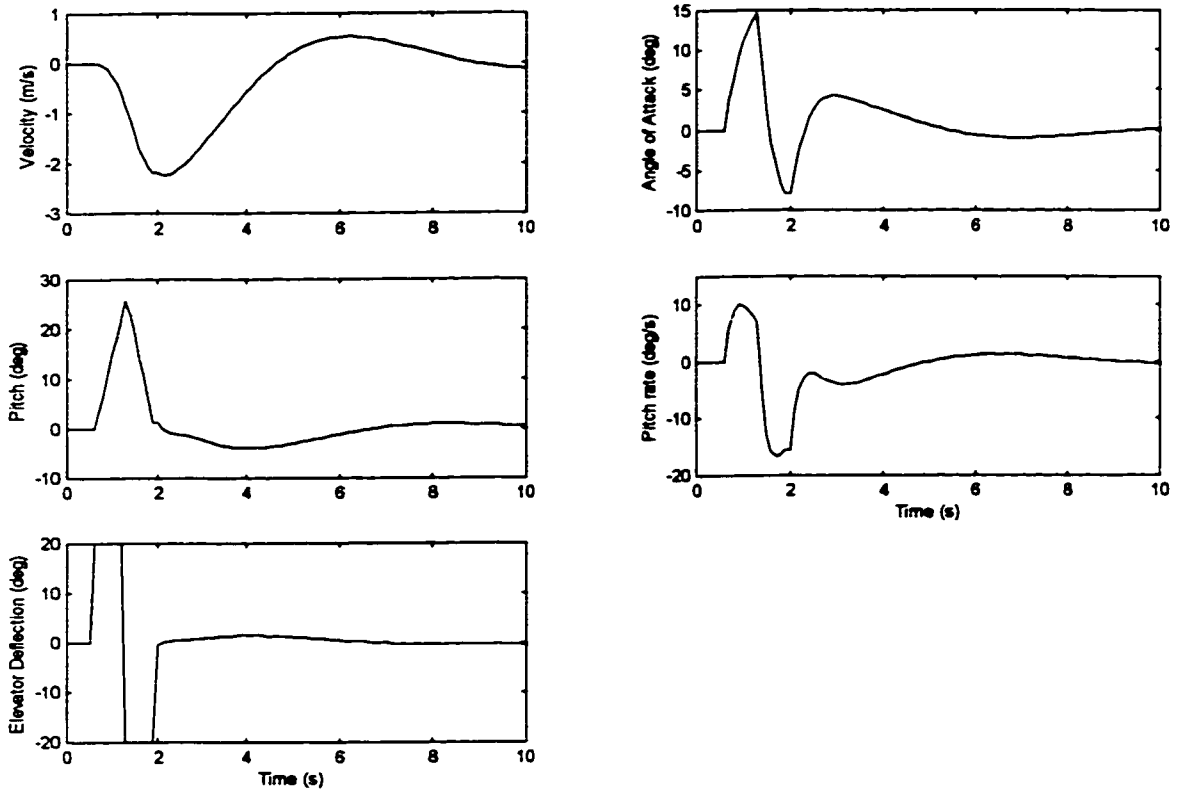

Figure 7.2 Simulated LQR response with pitch only feedback

7.4 Experimental Results

The optimal output feedback controller was then applied to the remotely controlled OHS aircraft. Figure 7.3 shows the elevator doublet response to the pitch only controller. The experimental result is not in correspondence with the computer simulation. The response shows a marginally stable control action. This experiment shows a discrepancy between the analytical model and the actual aircraft. The problem could be that the nonlinearities present in the physical system are too important to be ignored. Otherwise, errors

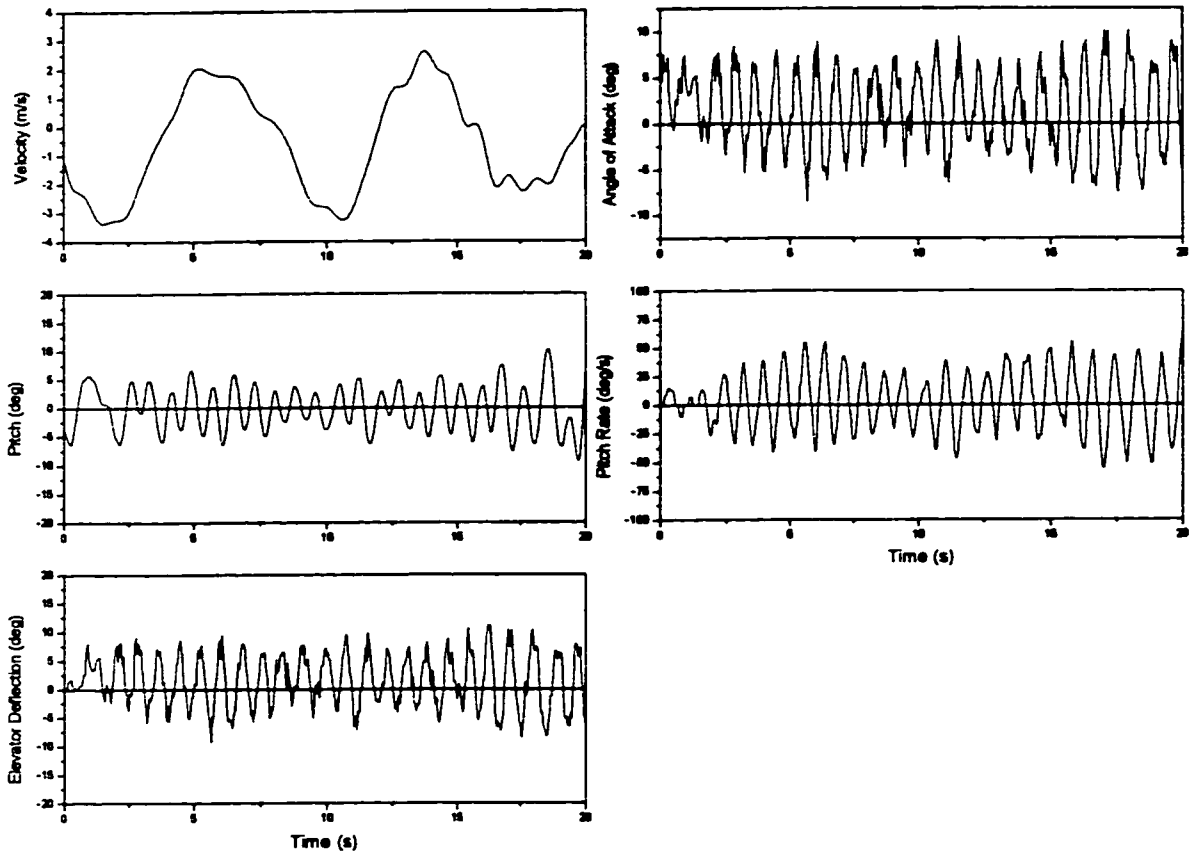

Figure 7.3 Closed loop flight test with Pitch only feedback

in the plant model could contribute to a poor choice in the controller gain resulting in the unsatisfactory system dynamics.

7.5 Summary

An algorithm for the LQ-optimal discrete time output feedback control problem is introduced and applied to the OHS aircraft. The optimal full state feedback controller is

designed for a set of given weighting matrices and resulted in a cost function of $J = 8.9531$. The cost function is recalculated after all but the pitch state was removed. The cost function increased to $J = 13.55$ and resulted in an acceptable loss in performance according to the computer simulations. However, the experimental results did not concur with the theoretical simulation. According to the physical experiment, pitch only control is not appropriate for this aircraft.

Chapter 8
System Identification

8.1 Introduction

The aircraft is fitted with numerous inertial and aerodynamic sensors. These sensors, along with the telemetry system, allow real-time flight data to be obtained. The experimental data is processed through a recursive least squares (RLS) parameter identification algorithm. The discrete time RLS algorithm is used to give continuity to later experiments involving real-time on-line estimation. The resulting model of the aircraft is the first step towards the development of adaptive and re-configurable flight control. These control schemes are useful in icing conditions, damaged flight or control surface situations. Also, autonomous flight can be used for control of unmanned high altitude research platforms such as sampling in the Ozone layer, and various military surveillance operations.

8.2 Recursive Least Squares Parameter Estimation

During flight experiments, telemetry data was recorded at a rate of 25 samples per second, on all five channels. These input and output data were processed through the RLS parameter estimation algorithm . To maintain continuity with actual experiments involving on-line parameter identification, the RLS algorithm is preferred over the batch method. The available sampling rate of 25 Hz dictates the use of discrete time equations, which are developed as follows.

Starting with the discrete time transfer function model of a dynamic system,

$$A(q)y(k) = B(q)u(k) \tag{8.49}$$

where q is the shift operator and $A(q)$ and $B(q)$ are the polynomials:

$$A(q) = q^n + a_1 q^{n-1} + \ldots + a_n \tag{8.50}$$

$$B(q) = b_1 q^m + b_2 q^{m-1} + \ldots + b_m \tag{8.51}$$

where n is the number of poles, and m is the number of zeros. The transfer function model can now be written in the discrete time domain as:

$$y(k) + a_1 y(k-1) + \ldots + a_n y(k-n) = b_1 u(k+m-n) + \ldots + b_m u(k-n). \tag{8.52}$$

Introduce a parameter vector:

$$\theta^T = \begin{bmatrix} a_1 & \ldots & a_n & b_1 & \ldots & b_m \end{bmatrix} \tag{8.53}$$

and regression vector:

$$\varphi^T(k-1) = \begin{bmatrix} -y(k-1) & \ldots & -y(k-n) & u(k+m-n) & \ldots & u(k-n) \end{bmatrix}. \tag{8.54}$$

The regression model can then be written as:

$$y(k) = \varphi^T(k-1)\theta. \tag{8.55}$$

The parameter estimates are obtained by recursively solving the following equations:

$$\begin{aligned} s(k) &= y(k) - \varphi^T(k-1)\hat{\theta}(k-1) \\ P(k) &= P(k-1) - P(k-1)\varphi(k)(I + \varphi^T(k)P(k-1)\varphi(k))^{-1}\varphi^T(k)P(k-1) \\ \hat{\theta}(k) &= \hat{\theta}(k-1) + P(k)\varphi(k-1)s(k) \end{aligned} \tag{8.56}$$

where $\hat{\theta}$ is the estimate of the parameters and the estimated model is:

$$\hat{y}(k) = \varphi^T(k-1)\hat{\theta}. \tag{8.57}$$

This will minimize the unweighted output error in measurements:

$$e = \sum_{j=1}^{k} (y(j) - \hat{y}(j))^2 \tag{8.58}$$

8.3 Flight Experiments

The flight tests for the 10th order experimental model were performed at the Airdrie Model Aircraft Society field in the summer of 1998. The pilot was Peter Thannhauser, an experienced RC aircraft pilot. Instrumented flights were conducted in early mornings and evenings in order to reduce effects of wind gusts and turbulence. Flight time was dictated by fuel consumption; the eight to ten minutes available provided sufficient time for numerous maneuvers.

The first tests were open loop instrumentation flights. The flight data was recorded and filtered on all channels and integrated on altitude, velocity and pitch, all in real time. Data collection was conducted in real time although it is not required during open loop tests. The control system requires the output signals: velocity, angle of attack, pitch, pitch rate, and altitude, as inputs to the controller in a closed loop configuration. This advanced development was therefore implemented during the open loop tests for continuity with later experiments.

8.3.1 10th Order Experimental Model Development

The RLS algorithm developed in Section 8.2 is applied to experimental flight data in order to model the aircraft. Several segments of data, five to ten seconds in length, with a

sufficiently rich elevator input, usually a varying frequency sign wave or elevator doublet signal, were utilized.

At first, a fifth order model was used to identify each system in hopes that the long and short period modes would be evident. The Dommasch [9] model suggests this to be the case, even though only one set of poles were perceptible for each output in the experimental data. Either the long period mode, in the case of velocity, or the short period mode in the case of altitude, pitch, pitch-rate and angle of attack. This could have been due to sensor noise, wind disturbances or non-linearities in the physical model overpowering the weaker mode in each channel.

The non-linearities in the OHS aircraft are predominantly in the pitching moment. The coupling that occurs between the lift on the tails and the wing tip vortices affects the pitching moment with changes in angle of attack. The experimental model is developed at a flight regime of nominally straight and level flight. The significance of the non-linearities is that the aircraft dynamics are difficult to portray with a simple model. Therefore, a higher order model was chosen in order to better represent the dynamics of the OHS aircraft.

The next approach involved reducing the order of the identified subsystem. A second order model should capture the dominant poles that are apparent in each subsystem. Therefore, the RLS algorithm was applied independently to each of the five output signals to obtain a second order system with two poles and one zero:

$$T(z) = \frac{z + b_1}{(z + a_1)(z + a_2)} \tag{8.59}$$

The covariance matrix was chosen as $P = 10^6 \cdot I_3$ and the initial parameter estimate $\theta_0^T = \begin{bmatrix} 0 & 0 & 0 \end{bmatrix}$. The parameter convergence for the elevator to pitch subsystem is

shown in Figure 8.1 and is indicative of the general processed data for all subsystems. Note that the majority of the parameter convergence took place in only four to five samples which is roughly the same as number of parameters in each identified subsystem.

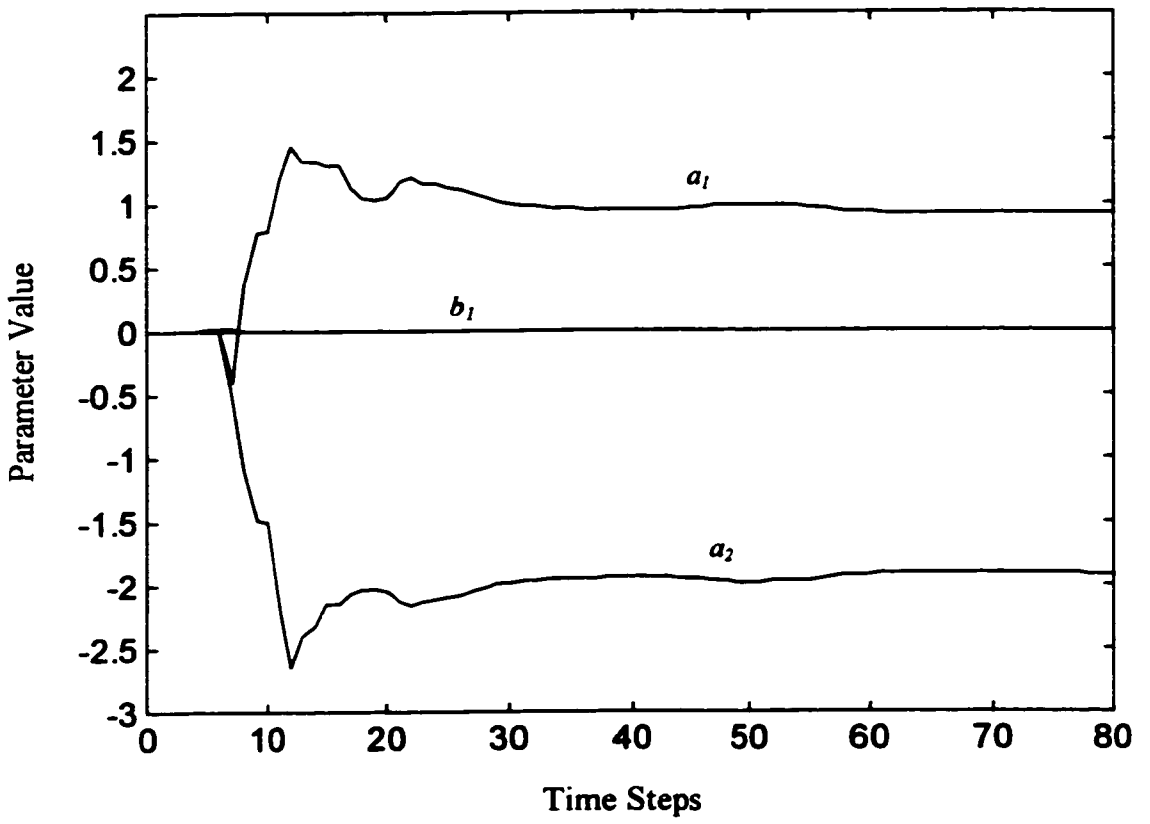

Figure 8.1 Convergence of pitch model parameters

The identified parameters as transfer functions are transformed to state space and then converted to continuous time via a zero order hold. The subsystems are then combined into a single state space model as follows

$$Ae = \begin{bmatrix} A_1 & 0 & 0 & 0 & 0 \\ 0 & A_2 & 0 & 0 & 0 \\ 0 & 0 & A_3 & 0 & 0 \\ 0 & 0 & 0 & A_4 & 0 \\ 0 & 0 & 0 & 0 & A_5 \end{bmatrix}, Be = \begin{bmatrix} B_1 \\ B_2 \\ B_3 \\ B_4 \\ B_5 \end{bmatrix}$$

$$Ce = \begin{bmatrix} C_1 & 0 & 0 & 0 & 0 \\ 0 & C_2 & 0 & 0 & 0 \\ 0 & 0 & C_3 & 0 & 0 \\ 0 & 0 & 0 & C_4 & 0 \\ 0 & 0 & 0 & 0 & C_5 \end{bmatrix}, De = \begin{bmatrix} D_1 \\ D_2 \\ D_3 \\ D_4 \\ D_5 \end{bmatrix} \quad (8.60)$$

The result is a 10th order model with elevator as the input and velocity, angle of attack, pitch, pitch rate, and altitude as the output. The estimated system in straight and level flight was calculated to be:

$$A_1 = \begin{bmatrix} 24.09 & -24.12 \\ 25.92 & -25.89 \end{bmatrix}, A_2 = \begin{bmatrix} 24.25 & -24.37 \\ 25.73 & -25.60 \end{bmatrix}$$

$$A_3 = \begin{bmatrix} 24.51 & -24.80 \\ 25.39 & -25.10 \end{bmatrix}, A_4 = \begin{bmatrix} 24.42 & -24.58 \\ 25.53 & -25.36 \end{bmatrix}$$

$$A_5 = \begin{bmatrix} 24.74 & -24.83 \\ 25.23 & -25.13 \end{bmatrix}$$

$$B_1 = \begin{bmatrix} 12.80 \\ -13.11 \end{bmatrix}, B_2 = \begin{bmatrix} 12.74 \\ -12.98 \end{bmatrix}$$

$$B_3 = \begin{bmatrix} 12.74 \\ -12.74 \end{bmatrix}, B_4 = \begin{bmatrix} 12.68 \\ -12.84 \end{bmatrix}$$

$$B_5 = \begin{bmatrix} 12.58 \\ -12.64 \end{bmatrix}$$

$$C_1 = [\ 0 \quad 0.0201\ ], C_2 = [\ 0 \quad -0.2148\ ]$$

$$C_3 = [\ 0 \quad -0.3239\ ], C_4 = [\ 0 \quad -0.1938\ ]$$

$$C_5 = [\ 0 \quad -0.0737\ ]$$

$$De = 0_{5x1}$$

Where the subsystems: $A_1 \Rightarrow velocity$, $A_2 \Rightarrow pitch$, $A_3 \Rightarrow pitchrate$, $A_4 \Rightarrow angle\ of\ attack$, and $A_5 \Rightarrow altitude$

The dynamics of the experimental model are present in the eigenvalues of the matrix Ae and are shown in Figure 8.2.Note that distinctions in the long and short period modes

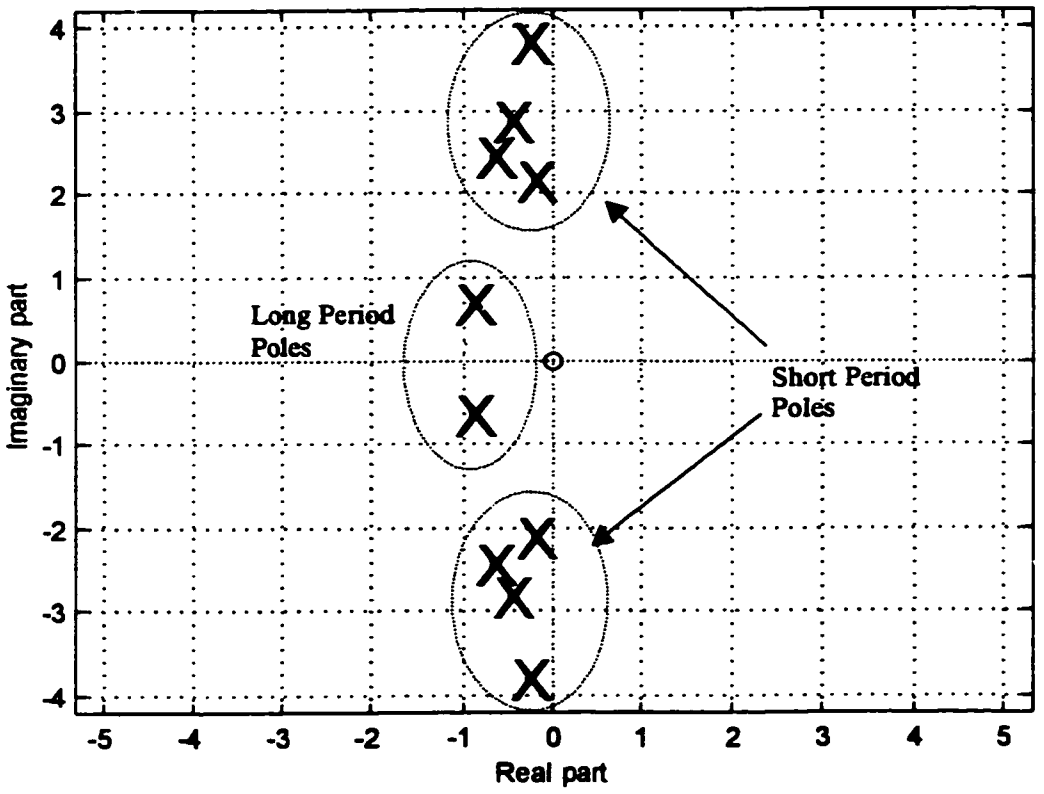

Figure 8.2 Poles of the experimental model

are present in the roots of the experimental model. The grouping of four poles correspond

to the short period mode while the lone pole closer to the x-axis relates to the slow pole of velocity.

8.3.2 Model Validation

Once a set of data has been processed through the RLS algorithm and a model emerges, it is necessary to evaluate the validity. Model validation can be accomplished in several ways. The first method is to simulate the model using the same data to which the model was developed. Computer simulations were done using Matlab [31]. Figure 8.3 shows the actual output data that was used to create the sub-model in pitch compared to the modeled data when simulated with the same input. There is a good correlation between the model and experimental data, indicating an acceptable model for this phase of validation.

Another method of validation is to simulate the model with an alternate set of data. Due to non-linearities in the aircraft, the alternate data set should be taken from a similar flight condition to that which the model was developed. In both cases, the aircraft was in straight level flight at the nominal operating conditions as mentioned previously. Figure 8.4 demonstrates that the sub-model in pitch is valid when compared to a different section of data.

An error analysis was conducted on the experimental and modelled data using:

$$error = \frac{\sum \sqrt{(y - \hat{y})^2}}{n}. \tag{8.61}$$

It was found that the average error for the simulation with modelled data was 0.38 *deg* and the simulation with validation data resulted in an average error of 0.16 *deg*. The magnitude of these values tend to validate the developed model.

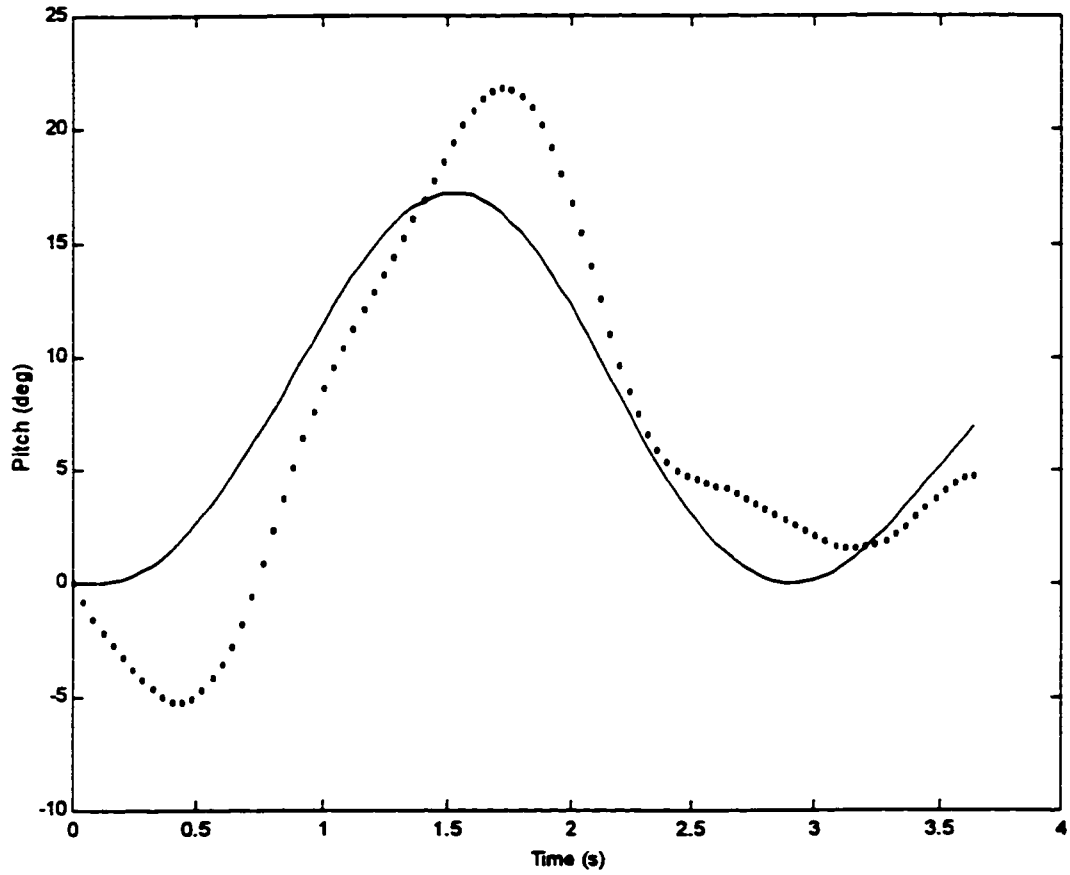

Figure 8.3 Actual and experimental pitch with modelling pitch data (model = solid, experimental = dashed)

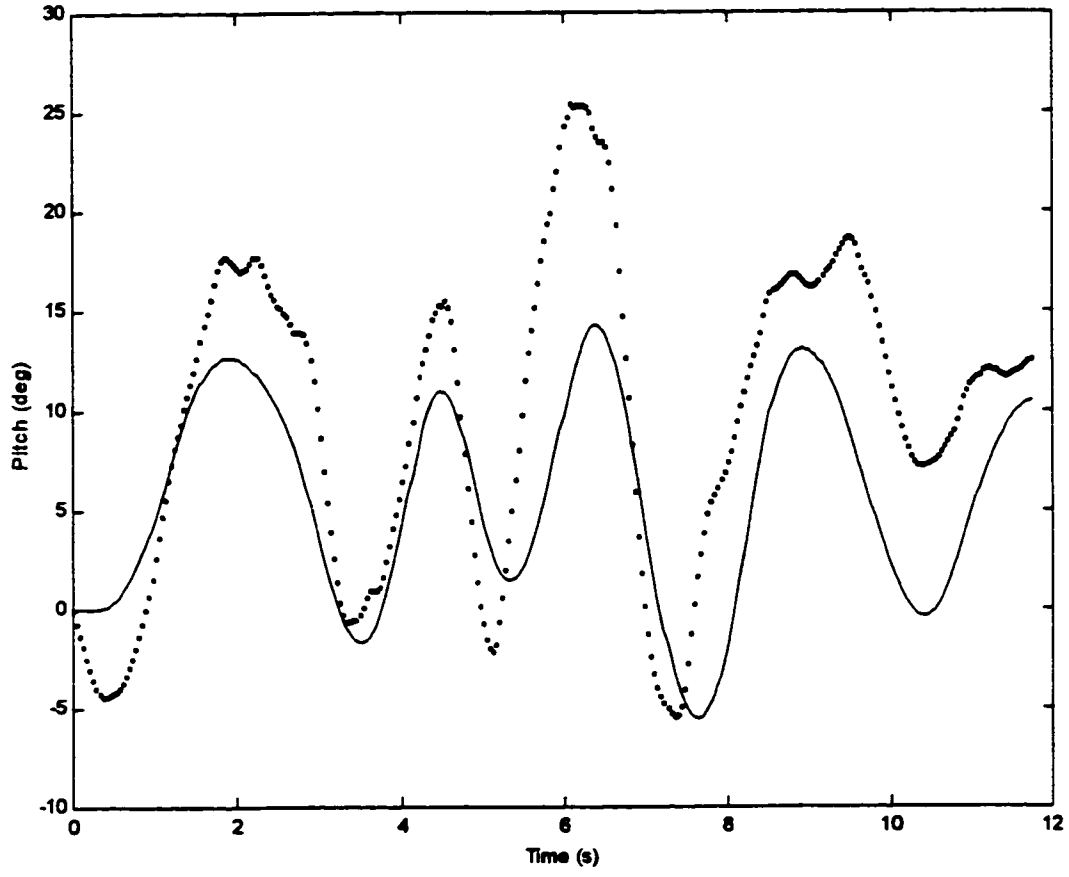

Figure 8.4 Actual and experimental pitch with validation data (model = solid, experimental = dashed)

The final method of validation uses the modified Dommasch Model. A comparison can be made between the theoretical and experimental models. Figure 8.5 depicts the frequency response of the two models in pitch. The breakpoints shown (Dommasch model $\Rightarrow$ 0.66 $rads/s$, Experimental model $\Rightarrow$ 1.0 rad/s) correspond to the phugoid mode and are very similar for both the theoretical and experimental plots. The roll-off is also comparable for the two models at -40 $dB/decade$.

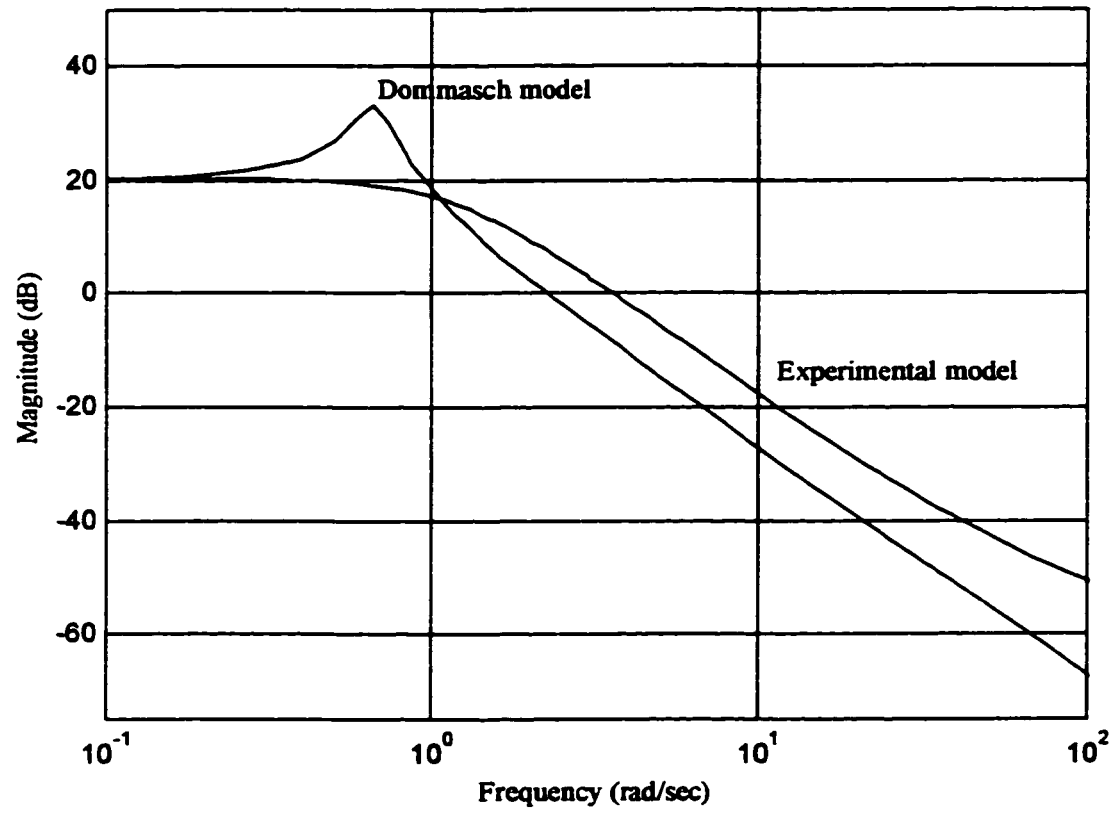

Figure 8.5 Velocity Frequency response of modified Dommasch and experimental model

The fifth order theoretical model and tenth order experimental model are shown to be quite comparable in the frequency domain.

8.3.3 State Estimator

The tenth order experimental model developed above does not permit state output. Therefore, an observer must be incorporated to allow state feedback. The measured outputs of the system are velocity, angle of attack, pitch, pitch rate, and altitude, but the states are unknown quantities at this time.

The Kalman filter is a form of state estimator. It extrapolates the state information from the output data which then allows for the use of standard state feedback controllers. Figure 8.6 shows a schematic diagram of how the state estimator fits into the standard feedback loop.

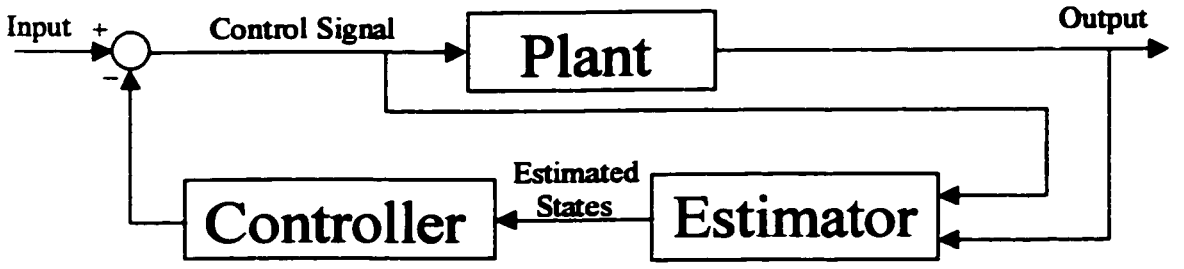

Figure 8.6 State estimation diagram

Given the state space system:

$$\dot{x} = Ax + Bu \tag{8.62}$$

$$y = Cx + Du \tag{8.63}$$

the Kalman filter is of the form

$$\dot{x}_e = Ax_e + Bu + L(y - Cx_e - Du) \tag{8.64}$$

where x_e is the state estimate and L is the Kalman estimator gain. The estimator gain L is found by solving the Riccati equation

$$AP + PA^T - PC^T R_n^{-1} CP + BQ_n B^T = 0 \tag{8.65}$$

for P where R_n and Q_n are respectively the measurement noise variance and process noise variance. The Kalman estimator gain L is obtained from

$$L = -R_n^{-1} CP \tag{8.66}$$

The state estimate x_e is then used as the input to the controller.

8.3.4 Implementation

The Kalman state estimator was then implemented in software on the computer controller. A simulation was conducted to ensure stability of the dynamic state observer. It was found that the optimal state estimator had poles that were faster than the 25 Hz sample rate, i.e. the time constant of at least one of the estimator poles was shorter than the sample period. The experimental estimator could not reproduce these fast poles. The result is that the implemented estimator did not function as designed and therefore went unstable. Next, the discrete Kalman filter was designed which would compensate for the slow sample rate. The discrete time version would not generate poles faster than the actual system could handle. The optimal discrete time Kalman filter was found to be too slow in the on-line simulation. The 25 Hz sampling rate again proved to be the culprit. The slow sampling rate forced the discrete time Kalman filter to have slow poles that were under-

damped and very slow to converge to the actual states. The dynamics of the state estimator caused too great a time delay in the system which again went unstable. The solution lies in simplicity; develop an experimentally estimated model which uses state output and would have no need for an observer.

8.3.5 4th Order Experimental Model

In the summer of 1999, a new set of flight experiments were conducted. Modifications were made to the sensors and instrumentation to give more accurate flight data (see Chapter 3). This new data was used to generate the experimental model developed in this section. The RLS parameter estimation scheme as described in Section 8.2 is used to generate the mathematical model. A single input single output (SISO) system with four poles and one zero was developed using the elevator control signal as the input and one of the sensor signals as the output.

Four discrete time transfer functions were formed from the outputs: Pitch, Pitch-rate, Angle of attack, and Altitude of the form

$$\frac{y(q)}{u(q)} = G(z) = \frac{\Gamma(q)}{\Phi(q)} \tag{8.67}$$

where u and y are respectively the input and output signals and Γ and Φ are the estimated transfer function polynomials. Each SISO system is then transformed to a state space realization to satisfy the equations

$$x_{k+1} = \Phi x_k + \Gamma u_k \tag{8.68}$$

$$y_k = C x_k + D u_k \tag{8.69}$$

where

$$\Phi = \begin{bmatrix} a_1 & a_2 & a_3 & a_4 \\ 1 & 0 & 0 & 0 \\ 0 & 1 & 0 & 0 \\ 0 & 0 & 1 & 0 \end{bmatrix}, \Gamma = \begin{bmatrix} 1 \\ 0 \\ 0 \\ 0 \end{bmatrix} \tag{8.70}$$

$$C = \begin{bmatrix} c_1 & 0 & 0 & 0 \end{bmatrix}, D = 0. \tag{8.71}$$

The four individual systems must be combined to one fourth order single input four output system.

The SISO systems are joined into one single input four output system because the eigenvalues of the four estimated systems were almost identical (within a 5 % error bound). The Φ matrix for pitch was used as the new combined Φ matrix because it gave the most consistent results. The Γ matrix is identical for all the systems so the combined Γ matrix is unchanged. The combined C matrix is a combination of all the component systems as follows

$$C = \begin{bmatrix} c_1 & 0 & 0 & 0 \\ 0 & c_2 & 0 & 0 \\ 0 & 0 & c_3 & 0 \\ 0 & 0 & 0 & c_4 \end{bmatrix}. \tag{8.72}$$

Adjustments for DC gain levels for the individual systems were made by multiplying the elements of the C matrix by the appropriate scale factor to normalize the system.

The composite system is then transformed to a state output system to aid the controller design. Otherwise an observer is required to determine the system states. A similarity transform is required to set C as an identity matrix resulting in a state output system. The transform matrix

$$T = C^{-1} \tag{8.73}$$

is chosen giving $C_t = TC = I$. The composite Φ and Γ matrices are transformed as follows

$$\Phi_t = T^{-1}\Phi T \tag{8.74}$$

$$\Gamma_t = T^{-1}\Gamma \tag{8.75}$$

resulting in a state output system for a single operating condition.

The estimated system at a flight velocity of 15 m/s is as follows:

$$\Phi_t = \begin{bmatrix} 2.121 & -0.204 & 0.004600 & 0.1750 \\ 6.000 & 0 & 0 & 0 \\ 0 & 0.1750 & 0 & 0 \\ 0 & 0 & 0.4762 & 0 \end{bmatrix}, \Gamma_t = \begin{bmatrix} 0 \\ 0 \\ 0 \\ 0.001000 \end{bmatrix}, C = I_{5x5}, D = 0 \tag{8.76}$$

The above state output system results in a $\omega_n = 0.97\ rad/s$ and a $\zeta = 0.30$. These values result in a system very similar to the Dommasch model developed in Chapter 4. The period of oscillation of the estimated model is 6.5 seconds which is close to the analytical model and even closer to the observed period of oscillation of 7.5 seconds. The damping is higher in the experimental model (analytical model $\zeta = 0.11$) which is again apparent in experimental observations. Therefore the above evidence clearly indicates the validity of the four order state output experimental model.

8.4 Summary

The OHS aircraft is modeled using the RLS parameter estimation algorithm. A tenth order model is developed with elevator as the input and velocity, angle of attack, pitch, pitch rate, and altitude as the outputs. The model is verified by comparing the dynamics

with the analytical model developed in Chapter 4. There is a definite correlation in the low frequency behavior of the two models as shown in Figure 8.5. In addition, both the theoretical and the experimental model predicted a set of fast and a set of slow poles corresponding to the short and long period modes respectively. These modes are also found to be stable according to both of the models.

A state estimator is developed for the 10th order estimated model and both are simulated to verify stability on the experimental setup. The observer is found to be unstable when implemented in software. A discrete observer is tried with unsuccessful results. A fourth order parameter estimated model employing state feedback is then developed. The fourth order state output model is then verified by comparing the dynamics of the analytical and experimental models. The fourth order experimental model is similar to the analytical model while resembling experimental observations.

Chapter 9
Adaptive Control

9.1 Introduction

The non-conventional configuration of the OHS aircraft results in nonlinear longitudinal dynamics varying with the flight condition. Fixed gain controllers are unable to provide satisfactory performance in all the flight regimes. This may have been a cause of failure in previous flight experiments such as those in Chapter 5. A variable gain controller is necessary to provide optimal stability and handling qualities throughout the entire flight.

Gain scheduling is widely used in the military aircraft industry to cope with the problem of variable plant dynamics [1]. A look-up table of controller gains is constructed from a multitude of flight test data. The aircraft flight control computer selects appropriate gains depending on the flight condition. A major drawback to this technique is the rigorous amount of testing and data collection required to build the gain schedule [45]. A more desirable method would involve on-line model identification and control design.

Adaptive control eliminates most of the prior knowledge and flight testing and gives potentially optimal flight performance in most flight regimes. This chapter follows the development and implementation of an optimal adaptive gain scheduled controller on a remotely controlled OHS model aircraft. First, a description is given of the controller design followed by computer simulation and experimental implementation of the controller.

9.2 Controller Design

The aircraft controller is constructed using a discrete time LQR structure based on a parameter estimated model of the aircraft. The OHS aircraft, as is common with other aircraft, has strong non-linear longitudinal dynamics with respect to airspeed. Therefore, a fixed gain controller gives sub-optimal performance when the aircraft is not operating at the nominal condition at which the controller was designed. A variable gain controller is required to compensate for these non-linearities.

The controller is a form of gain scheduling with the ability to generate and regenerate itself during flight operation. This "adaptive" quality has two major benefits. The first is that the controller can be designed on-line in real-time without the need for extensive flight testing. The second is the ability of the controller to make necessary corrections to the gain schedule in case of both expected and unexpected variations in the aircraft dynamics. Expected variations could include changes in mass and/or center of gravity due to differing fuel levels or deployment of weapons stores. An unexpected variation could include damage to a control surface or some part of the aircraft during flight. All of these variations will cause some degree of change in the dynamics of the aircraft. Subtle changes should be compensated by a robust controller, but extreme alterations in the aircraft dynamics will result in sub-optimal performance and even uncontrollable characteristics.

The computer controller uses the RLS parameter estimation scheme from Section 8.2 to generate the fourth order state feedback model developed in Section 8.3.5. The estimation algorithm was conducted in Labview. The model was updated when there was enough plant excitation to provide sufficiently rich data for the RLS estimation algorithm.

It was found, through extensive testing, that an elevator signal with a peek value equivalent to one half the full scale deflection, resulted in the necessary excitation for a suitable plant model. As the magnitude of the difference, between two consecutive iterations, of the estimated parameters approached zero, (value used $\Rightarrow 10^{-4}$), the estimation algorithm was halted and the current plant model was realized. The coefficients of the plant model were transferred over to Matlab where the discrete time LQR algorithm generated the necessary control gains. A q/r ratio of five was used for the LQR controller design. The control gains for the particular flight regime, airspeed, was mapped to a text file to be used as the raw data for the gain schedule.

Several plants were estimated in-flight at different airspeeds. The gain schedule was developed on-line using the generated control gains. A second order polynomial fit on the gain data results in the gain schedule shown in Figure 9.1. The data was fit using three data points for each of the outputs: Pitch, Pitch rate, Angle of attack, and Altitude. The controller reads the continuous data from the gain schedule equation resulting in smooth controller adjustments with changing airspeed.

9.3 Computer Simulation

The controller was simulated on a computer using Matlab [31] to verify the stability of the controller. The simulations were conducted using experimentally modelled plants at relatively low and high airspeeds. Figure 9.2 shows the dominant open loop system poles varying with airspeed plotted on the z-plane. An increase in airspeed results in an increase in the natural frequency and a slight increase in damping.

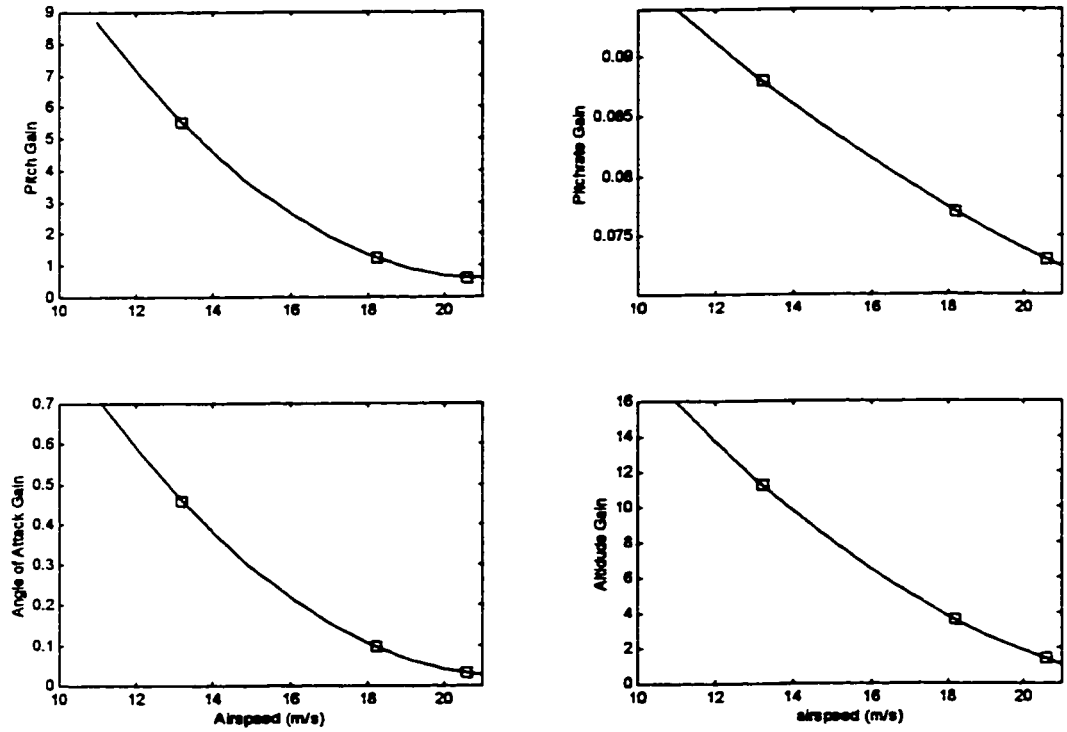

Figure 9.1 Gain schedule with varying airspeed

Figure 9.3 shows the open loop response of the experimentally modelled system at an airspeed of 13.3 m/s. The input signal is an elevator doublet signal of magnitude one corresponding to the maximum positive and negative deflection of 20 degrees for a total period of 1.5 seconds. The response is stable and moderately damped with a settling time of 12.5 seconds following the doublet signal. The aircraft has a natural oscillation period of 6.5 seconds for the low speed flight regime.

Figure 9.4 also shows the open loop response to the elevator doublet of magnitude one. The first observation is the increase in amplitude of the response. This indicates that the elevator control is more effective at the higher airspeeds. The aircraft system has a

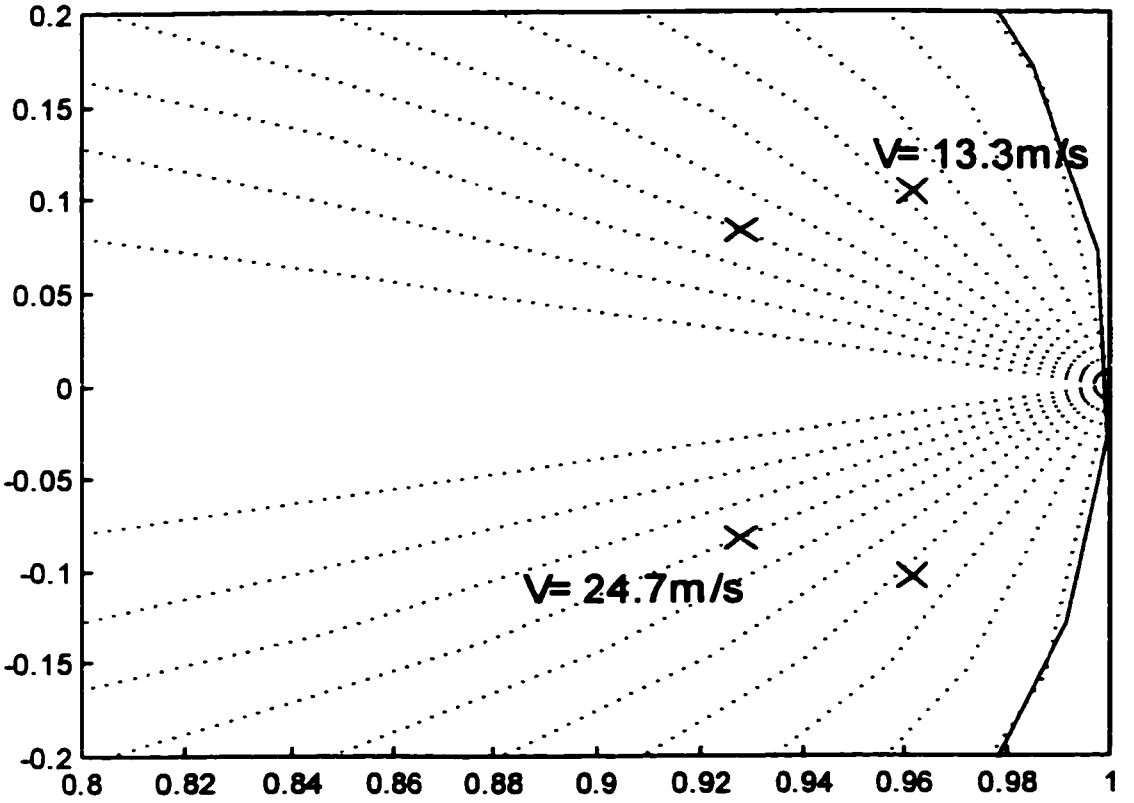

Figure 9.2 Open loop long period mode poles varying with airspeed

quicker response with a settling time of 7.5 seconds following the excitation signal. The system damping has increased from 0.30 for the low speed plant to 0.62 for the high speed plant.

The closed loop simulations were conducted using the discrete time LQR controllers developed for the aircraft with the appropriate model. A controller was designed for the aircraft model at the flight condition of 13.3 m/s. The closed loop response of the system is shown in Figure 9.5. The simulation involves an open loop and a closed loop phase.

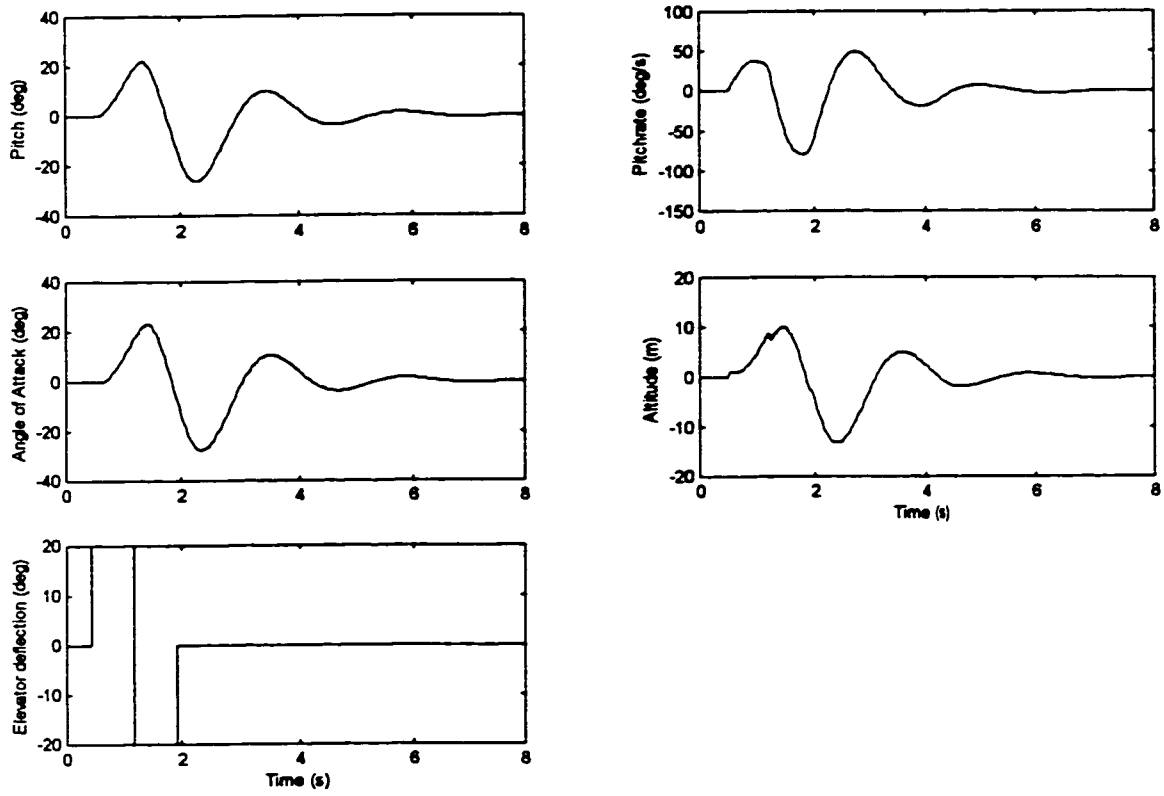

Figure 9.3 Open loop simulation at 13.3 m/s

During the elevator doublet, the system is left in open loop to excite the aircraft. Upon completion of the excitation signal, the feedback loop is closed. This method was used to achieve consistent initial conditions for the closed loop response. Otherwise, tests done with varying control gains could not be comparable if the aircraft was excited in closed loop.

The aircraft response at 13.3 m/s with LQR feed back is very quick. The system reaches steady state almost immediately following the instigation of the controller. A

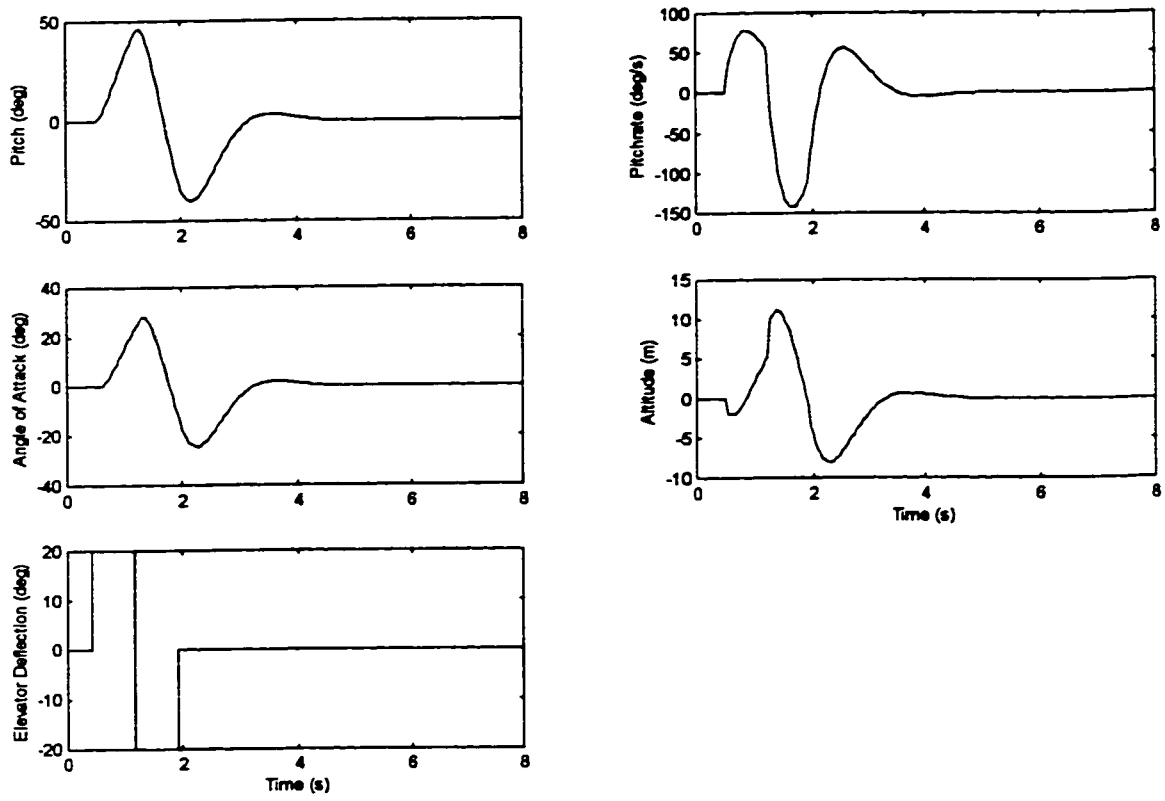

Figure 9.4 Open loop simulation at 24.7 m/s

moderate amount of control action is required at the low speed condition as the elevators are less effective.

A similar simulation was conducted at a higher speed to analyze the effect of how the control action must be adjusted with airspeed. Figure 9.6 shows the closed loop response of the simulated model to the same elevator excitation signal at a speed of 24.7 m/s. Again, the system responds very quickly once the controller is activated. The difference is the amount of control action used. The higher airspeed results in a much smaller set of control gains and correspondingly smaller control action.

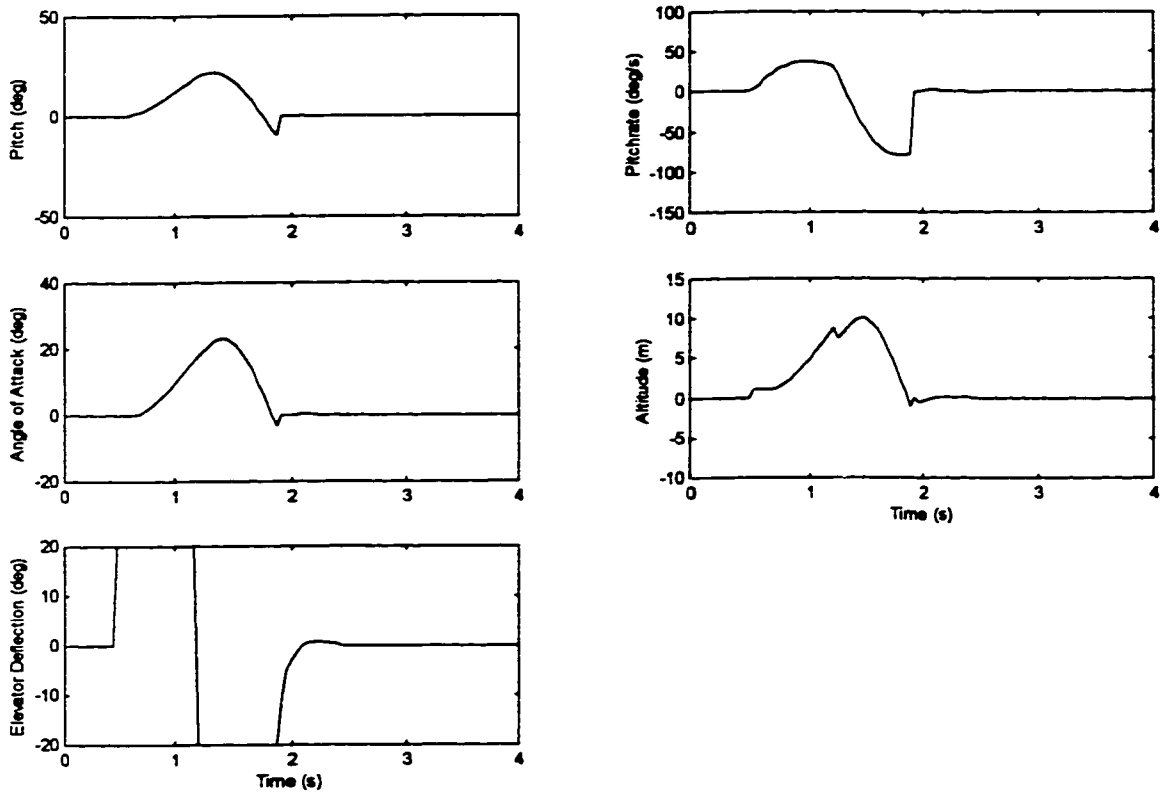

Figure 9.5 Closed loop simulation at 13.3 m/s

Figure 9.7 portrays the motion of the long period mode poles with increasing amounts of control. The initial open loop poles for the low and high speed cases are farthest to the right of the graph. As the control gains are increased, the poles migrate to the left of the graph resulting in increased stability and a quicker response time. Note that the damping of the low speed poles remain almost constant while the damping of the higher speed poles increases with increasing control gains. This is most likely due to aerodynamic effects. At slower airspeeds, the elevator can only apply a limited amount of pitching moment control

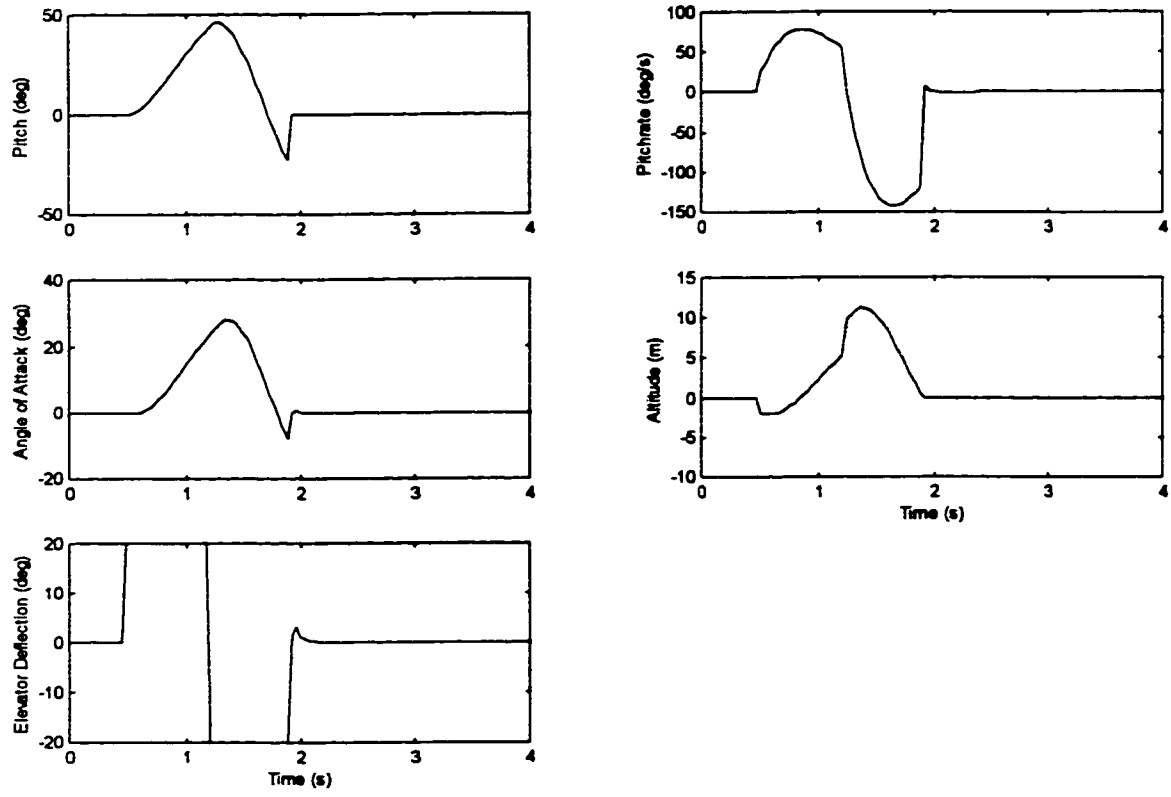

Figure 9.6 Closed loop simulation at 24.7 m/s

while at higher speeds, the increased airflow over the tail surfaces result in a much larger amount of pitching moment control with less elevator deflection.

9.4 Experimental Results

Following from the computer simulations, a similar set of experiments were carried out on the remote controlled OHS aircraft. The input or excitation signal was an elevator doublet of near full scale deflection. An angle of ± 20 degrees was used as the elevator

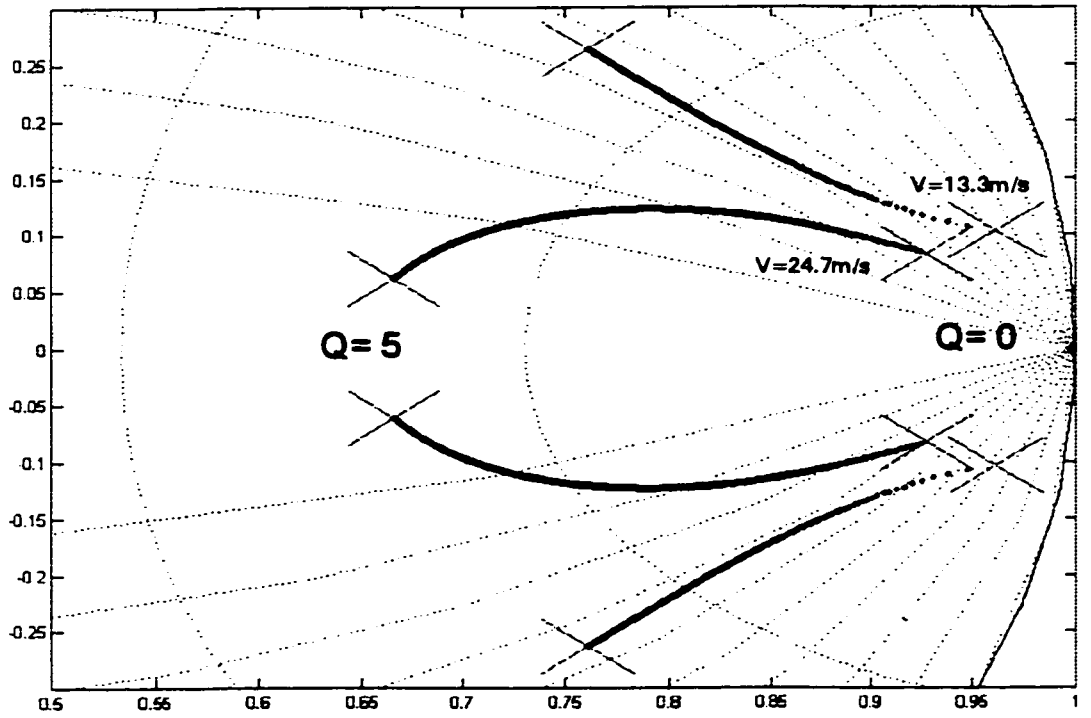

Figure 9.7 Long period mode root locus for varying $Q = q \cdot I$ for both low and high speed plants (control increases from right to left)

excitation amplitude for a total period of 1.5 seconds. During the flight experiments the excitation signal was performed in an open loop control configuration. The LQR controller was deactivated for the duration of the elevator doublet to ensure similar initial conditions for all the flight experiments. The computer simulations were conducted in the same manner.

The time constant of the velocity sensor is too slow to pick up the quick changes in velocity during the closed loop experiments. The anemometer is a propeller driven DC motor with an output voltage signal proportional to airspeed. The aerodynamic and inertial

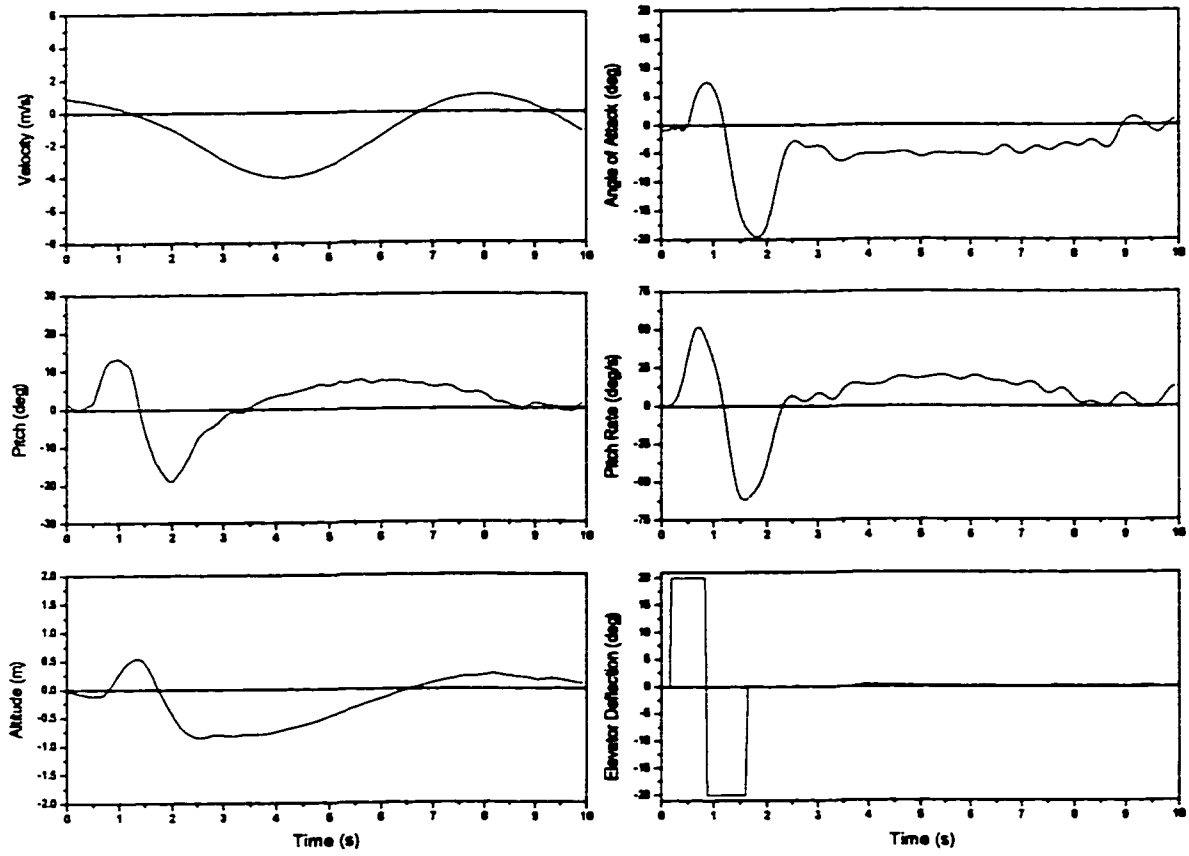

Figure 9.8 Experimental open loop response at 15 m/s

effects slow the response of the motor-propeller system and is therefore unable to detect the relatively fast changes in airspeed.

Figure 9.8 depicts the open loop response to the elevator doublet excitation signal. A long period mode of about 7.5 seconds is close to the simulated open loop dominant mode, with a similar airspeed, of 6.5 seconds. The damping is slightly higher in the physical

aircraft. Oscillatory motions are almost fully damped out shortly after the first full post excitation cycle.

The closed loop flight tests used the gain scheduled controller. During the flight, the controller was put into learning mode where it created the gain schedule. The OHS aircraft was excited with the elevator doublet at various airspeeds. The RLS parameter estimation algorithm was run on the data in-flight to give a plant model at the particular airspeed. The LQR controller design scheme was used to find the optimal gains for several plant models. The set of control gains were then formed into the data set for the gain schedule. A second order polynomial function was fitted to the data points for each state (see Figure 9.1). The aircraft flight computer was then switched to operation mode where it utilized the gain schedule on a continuous basis. The control gains were automatically adjusted during flight to give optimal performance at the full range of flight speeds.

Figure 9.9 shows the aircraft response to the elevator doublet at a speed of nominally 15 m/s. This is considered the low speed case similar to the 13.3 m/s plant. The OHS aircraft responds very quickly reaching steady state in 2.5 seconds following the excitation signal. The velocity measurement is an exception to this as the anemometer response time is much too slow to track the changes. The control action is fairly large (30 % full scale deflection) due to the slow speed and relatively large control gains. This result matches with the computer simulation from Section 9.3.

The high speed closed loop response of the OHS aircraft is depicted in Figure 9.10. The overall response is remarkably similar to the low speed response. The system reaches steady state in 2.7 seconds following the completion of the excitation signal as compared

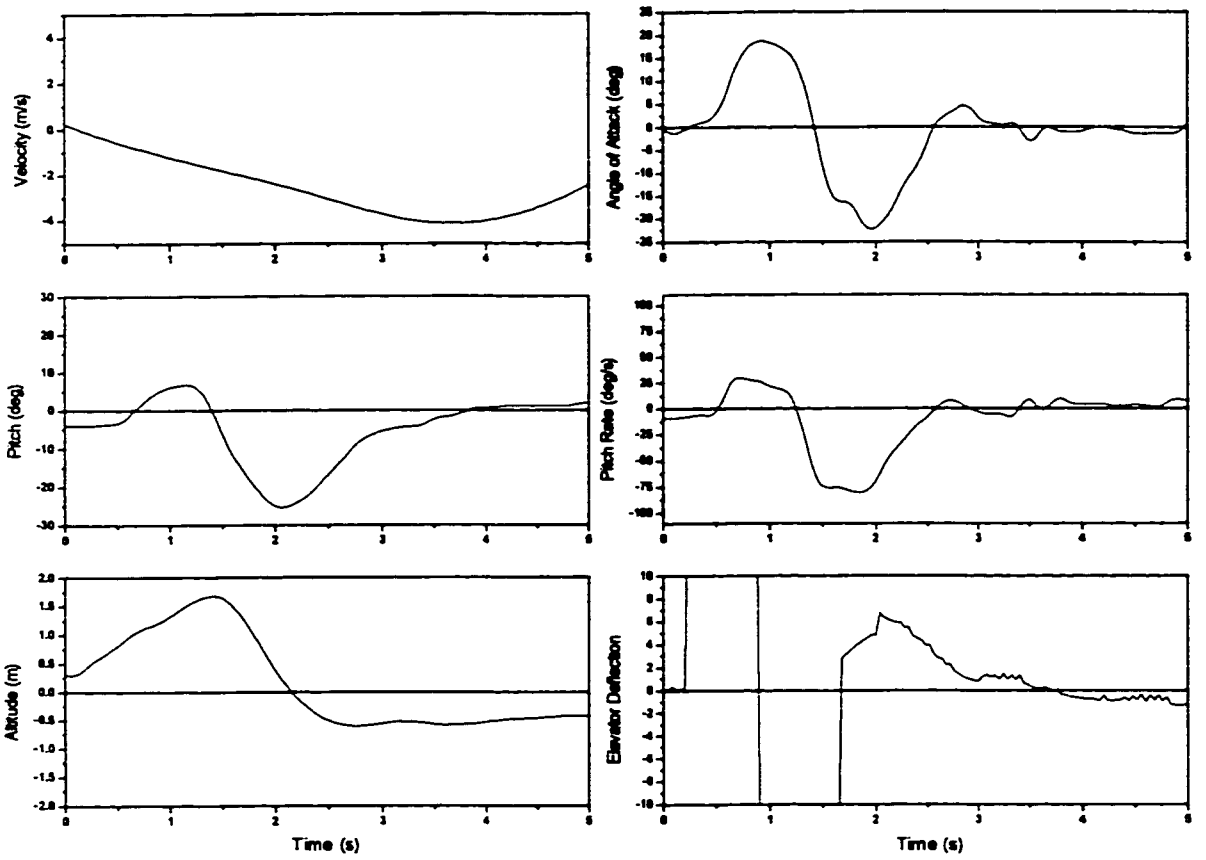

Figure 9.9 Closed loop experimental adaptive gain schedule response at 15 m/s

to the 2.5 second response time in the low speed test. The major exception is the amount of control action utilized. The higher speed resulted in less control action to maintain optimal performance. An elevator deflection of only five percent of the full scale range was required to control the OHS aircraft at an airspeed of 20 m/s.

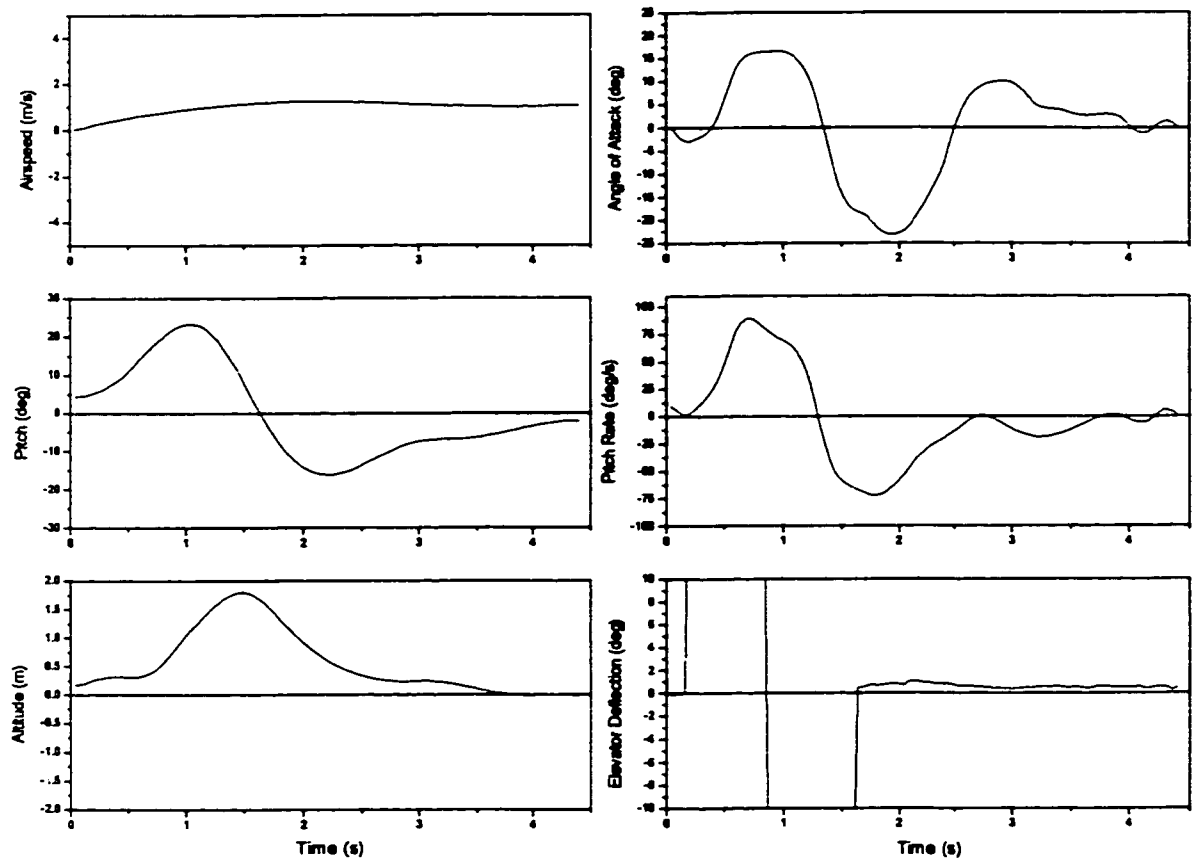

Figure 9.10 Closed loop experimental adaptive gain schedule response at 20 m/s

9.5 Summary

An optimal adaptive gain scheduled controller is developed for a non-conventional remote controlled aircraft. A fourth order plant model with elevator as the input and pitch, pitch-rate, angle of attack, and altitude as the outputs is constructed using a RLS parameter estimation scheme from experimental data at several airspeeds. A Linear Quadratic Optimal controller is designed for each of the plant models resulting in an optimal gain

schedule. Open and closed loop computer simulations are conducted to analyze the response of the estimated models and to aid in the controller design. Finally, the variable gain controller is implemented on the physical aircraft in a series of open and closed loop experiments.

Overall, the experimental results are in correspondence with the theoretical analysis of the estimated models. The theoretical and experimental results show a dependence of the controller gains with respect to airspeed. The higher the airspeed, the lower the required control gains to maintain optimal performance.

Table 9.1 shows the calculated cost function for the simulated and experimental data. The simulation results indicate a much higher cost function in the slow airspeed plant than in the higher airspeed plant. Conversely, the experimental values are very close to one another despite the differences in the control action (see Figure 9.9 and Figure 9.10). Noise in the experimental data could attribute to the deviation from the simulated trend.

Airspeed	Simulated	Experimental
Slow	4.591	19309
Fast	0.006	14770

Table 9.1 Cost function J for the adaptive controller in slow and high speed flight

Chapter 10
Summary and Conclusions

10.1 Summary

The Outboard Horizontal Stabilizer aircraft is a non-conventional aircraft with an unusual tail arrangement. This particular tail configuration provides effective lifting surfaces that increase the overall efficiency of the aircraft. It is suitable for many research and military applications such as environmental high altitude research platforms and aerial surveillance. A control system study on the aircraft was undertaken to improve the overall flight characteristics and gain insight into this innovative design.

An OHS RC model aircraft, previously used as the University of Calgary entry into the 1995 SAE Aero Design Competition, was fitted with various hardware and electronics as part of a real-time feedback control system. Several aerodynamic and inertial sensors were attached to the aircraft along with a telemetry transmitter. A ground based receiver and data acquisition system retrieved the telemetry data and passed it to a computer controller. The computer controller was implemented in Labview on a Microsoft Windows 95 operating system. The computer controller took the pilot stick inputs along with the telemetry data and returned a modified input based on a specified control strategy.

The longitudinal dynamics of the OHS aircraft were modelled and analyzed as the first step in the control system design process. It was found that strong non-linearities existed with respect to the pitching moment. The aircraft model also showed an increase

in longitudinal stability as compared to conventional aircraft but with this came the issue of a strong coupling between the pitching moment and the airspeed.

Several control strategies were attempted on the OHS aircraft. Initially, a simple proportional and a proportional plus derivative feedback controller were applied. The resulting flight response was, however, unsatisfactory. Further development of a PD controller would have led to an improvement in performance but this avenue was not taken in favor of a more advanced control structure.

A LQR controller was designed for the aircraft based on the analytical model previously developed. The controller was simulated on a computer and then implemented on the experimental aircraft. The response displayed a dramatic increase in flight performance that corresponded well with the simulated data.

An attempt to eliminate some of the states in an effort to reduce the complexity of the controller and the number of sensors was undertaken. The computer simulations gave encouraging results although the experimental results did not concur.

A RLS parameter estimated model was developed using available experimental flight data. First, a tenth order model was developed in which the dynamics resembled the analytical model. The implementation of the LQR controller design about this model was not successful. The model required an observer because the states were not available in the outputs. The Kalman filter that was developed added too much delay into the overall system and therefore caused the controller to become unstable. A fourth order state output system consisting of angle of attack, pitch, pitch rate and altitude was then developed. This

model proved successful in accurately depicting the dynamics of the OHS aircraft and had no need of a state observer.

An adaptive controller was developed for the OHS aircraft to compensate for the varying dynamics with changes in airspeed. The adaptive LQR gain scheduled controller that emerged gave optimal flight performance with changes in airspeed. The overall handling qualities of the aircraft were dramatically improved no matter what part of the flight envelope the aircraft was in.

A cost function analysis was also conducted on all of the simulated and experimental data. In most cases, the trends of the experimental data coincided with the simulation results. Noise, along with non-zero steady-states in the experimental data could have contributed to the differences in magnitudes of the simulation and experimental cost functions.

The contributions of this dissertation include: the experimental study on a non-conventional aircraft design; the development of the telemetry, hardware and control system for the OHS RC model aircraft; the development of a mathematical model for the OHS aircraft; experimental research and control analysis on the OHS aircraft; and the development of an adaptive LQR gain scheduled controller for the OHS RC model aircraft.

10.2 Conclusions

The OHS aircraft design is very different from a conventional aircraft. The unique tail configuration allows for a decrease in the overall drag of the aircraft with the efficient utilization of the energy discarded by the wing tip vortices. This tail configuration also adjusts the longitudinal dynamics associated with the pitching moment. There is a stronger

relationship between the pitching moment and the angle of attack (or lift coefficient) that requires attention when dealing with multiple flight regimes.

The development of the adaptive gain scheduled controller for the OHS RC model aircraft was successful in achieving the goals of improved flight performance. The adaptive nature of the controller avoids the strenuous experimental testing of conventional gain schedule controllers. The LQR algorithm implemented results in dramatically improved handling qualities. The variable gain control provides substantially improved performance in the higher flight speed regime. Previously, the OHS aircraft was very difficult to handle at airspeeds above 20 m/s. With the addition of the adaptive gain scheduled controller, the aircraft was as controllable as in the slower flight regimes.

References

1. Amato, F., and G. Ambrosino, "Design and Robustness analysis of Gain-Scheduled Control System for Parabolic Flight", *Journal of Guidance Control, and Dynamics*, Vol. 19, No. 2, Mar-Apr 1996, pp 430-437.

2. Ambegaonkar, P., and A. Ellis, "Microprocessor Based Digital Autopilot", Proceedings of the National Electronics Conference, Vol. 34, Oct 1980, pp 437-441.

3. Anderson, B.D.O., and J.B. Moore, *Optimal Control, Linear Quadratic Methods*, Prentice Hall, 1990.

4. Ashley, S., "Robot Spy Planes Peer Over the Horizon", Mechanical Engineering, ASME, Mar 1996, pp 84-89.

5. Åström, K. J., and B. Wittenmark, *Adaptive Control*, Second Edition, Prentice Hall, 1995

6. Åström, K. J., and B. Wittenmark, *Computer-controlled Systems*, Third Edition, Prentice Hall, 1997

7. Coleman, R., and A.J. Robins, "Mini-RPV Research", *Aeronautical Journal*, Vol. 85, No. 481, Feb 1981, pp 39-47.

8. Crossbow Technologies Inc. 41 E. Daggett Drive, San Jose, Ca 95134

9. Dommasch, D.O., S.S. Sherby, and T.F. Connolly, *Airplane Aerodynamics*, U.S. Naval Academy, 1968.

10. Drela, M., "X-foil", Aerodynamic Simulation Program, MIT

11. Dunn, H.J., "Realizable Optimal Control for a Remotely Piloted Research Vehicle", NASA Technical Paper, May 1980.

12. Fluent Inc., Centerra Resource Park, 10 Cavendish Court, Lebanon, NH 03766-1442.

13. Frangos, C., and Y. Yavin, "Design Methodology for Linear Optimal Control Systems", *Journal of Guidance, Control, and Dynamics*, Vol. 15, No. 5, Sep-Oct 1992, pp 1302-1304.

14. Hartley, G.A., "Pitch Axis Control System Design for QF-4 Full-Scale Aircraft Target", SAE Technical Paper Series, 1986, p 14.

15. Hill, M.L., "Electrical Disturbances Near Thunderstorms Observed by Means of Small Remotely Piloted Aircraft Stabilized with Respect to the Local Field Vector", 7th International Conference on Atmospheric Electricity, 1984, pp 272-278.

16. Hopkin D., and M. Davies, "Aerodynamics and Control of A Remotely-Piloted Underwater Towed Vehicle", *Canadian Aeronautics and Space Journal*, Vol. 36, No. 3, Sept. 1990, pp 122-129.

17. Kailith, T., *Linear Systems*, Prentice Hall, 1980

18. Kentfield, J.A.C. "Aircraft Configurations with Outboard Horizontal Stabilizers", *Journal of Aircraft*, Vol. 28, No. 10, 1991,pp 670-672.

19. Kentfield, J.A.C. "Influence of Aspect ratio on the Performance of Outboard-Horizontal-Stabilizer Aircraft", *Journal of Aircraft*, Vol. 37, No. 1, pp 62-67.

20. Kentfield, J.A.C. "The Flight Characteristics of a Commuter Aircraft Employing Outboard Horizontal Stabilizers", SAE Paper 965610, Oct., 1996.

21. Kentfield, J.A.C. "Operational Structural Loading of OHS Aircraft Relative to Comparable Conventional Designs", AIAA Paper 2000-0909, 38th AIAA Aerospace Sciences Meeting and Exhibit, Reno, Navada, 2000.

22. Krutova, I.N., and V.Y. Rutkovskii, "Robustness of Control Systems with Nonlinear Parameter Correction of Some Disturbances", *Automation and Remote Control*, Feb 1992, Vol. 52, No. 9, pp 1293-1303.

23. Labview Version 5.1, National Instruments Corp., 1998.

24. Larsen, T.L., "Remotely Piloted Vehicle Technology Development using the XQM-103 Research Test Vehicle", SAE Preprints, Nov 1975.

25. Levine, W.S., and M. Athans, "On the Determination of the Optimal Output Feedback Gains for Linear Multivariable Systems", IEEE Trans. Auto. Control, vol AC-15, no. 1, 1970, pp 44-48.

26. Lin, C.E., and W.G. Wen, "State Estimation for Random Error Reduction in Avionic Measurement Applications", IEE Instrumentation and Measurement Technology Conference, Apr 1989, pp 388-393.

27. Linehan, R.D., K.J. Burnham, and D.J.G. James, "Optimal Control Strategy for a Surveillance RPV", IEE Colloquium, Jun 1995, pp 7/1-7/4.

28. Linehan, R.D., K.J. Burnham, and D.J.G. James, "4-Dimensional Control of a Remotely Piloted Vehicle", IEE Conference Publication, Sept. 1996, pp 770-775.

29. Ljung, L., *System Identification - Theory for the User*, Prentice Hall 1999

30. Math Works, *Using Matlab*, Ver. 4, 1996

31. Matlab Version 5, The Math Works Inc., 1996.

32. Maxim Integrated Products,120 San Gabriel Drive, Sunnyvale, CA 94086

33. Mizell, D.W., "Algorithms and Architectures Needed for Future Autonomous Military Systems", IEEE Electronics and Aerospace Systems Convention, 1984, p 221.

34. Montoya, R.J., and A.R.Jai, "Application of a Ground Based Minicomputer System for Real Time, Closed Loop Control of Remotely Piloted Aircraft Models Used in Stall/Spin Research", National Bureau of Standards, Special Publication, Jan 1979, pp 167-172.

35. Mook, D.J., and I. Shyu, "Nonlinear Aircraft Tracking Filter Utilizing Control Variable Estimation", *Journal of Guidance, Control, and Dynamics*, Vol. 15, No. 1, Jan-Feb 1992, pp 228-237.

36. Mudge, S.K., and R.J. Patton, "Enhanced Assessment of Robustness for an Aircraft's Sliding Mode Controller", *Journal of Guidance, Control, and Dynamics*,Vol. 11, No. 6, Nov-Dec 1988, pp 500-507.

37. Mukherjee, J.S., and W.C. Pitstra, "An Adventure in Heavy Lift", SAE Aero Design Competition Report, 1995

38. Neidhoefer, J.C., and K. Krishnakumar, "Immunized Neurocontrol for a Remotely Piloted Aircraft", Artificial Neural Networks in Engineering-Proceedings, Nov 1994, pp 943-948.

39. Pieper, J.K. and K.R. Goheen, "Analysis of Discrete Optimal Output feedback with Helicopter Control System Design Application", Proceeding of the Winter Simulation Conference, Honalulu, 1993.

40. Pineiro, L.A., and D.J. Biezad, "Real-Time Parameter Identification Applied to Flight Simulation" IEEE Transactions on Aerospace and Electronic Systems, Vol. 29, No. 2, 1993

41. Postlethwaite, I., and D.G. Bates, "Robust Integrated Flight and Propulsion Control (IFPC) System Design for the VAAC Harrier STOVL Aircraft", IEE Conference Publication, 1998, pp 1516-1521.

42. Redling, T.J., "Derivation of S-Domain Aircraft Models", Proceedings of the IEEE International Conference on Engineering of Complex Computer Systems, Nov 1995, pp 187-190.

43. Roger, K. L., "Airplane Math Modeling Methods for Active Control Design", AGARD Conference Proceedings, Apr 1977, pp 1-11.

44. Scaled Composites, 1624 Flight Line, Mojave, CA 93501-1663

45. Shamma, J.S., and J.R. Cloutier, "Gain-scheduled missile autopilot design using linear parameter varying transformations", *Journal of Guidance, Control, and Dynamics*, Vol. 16, No. 2, Mar-Apr 1993, pp 256-263.

46. Skogestad, S., and I. Postlethwaite, *Multivariable Feedback Control*, John Wiley and Sons, 1996

47. Stevens, B.L., and F.L. Lewis, *Aircraft Control and Simulation*, John Wiley & Sons, Inc., New York 1992

48. Tomlins, G.F., "Some Considerations in the Design of Low Cost Remotely-Piloted Aircraft for Civil Remote Sensing Applications", Canadian Surveyor, Vol. 37, No. 3, Autumn 1983, pp 157-167.

49. Vandersteen, A.D., "Avionics for the Small Remotely Piloted Vehicle", Proceedings-IEEE/AIAA 7th Digital Avionics Systems Conference, 1996, pp 475-482.

50. Watson Industries, 3041 Melby Road, Eau Claire, WI 54703

51. Wigdorowitz, B., "Application of Linearization Analysis to Aircraft Dynamics", *Journal of Guidance Control, and Dynamics*, Vol. 15, No. 3, May-Jun 1992, pp 746-750.

52. Xie, W., and B. Liu, "Design Features of Automatic Control System of D-4 RPV", *Journal of Northwestern Polytechnical University*, Vol. 4, No. 2, Apr 1986, pp 217-226.

Appendix A
Labview Program

The Labview computer controller program is given in this appendix. The front panel is the user interface and the wiring diagrams are the computer code or programing language. The program consists of the main diagram and many sub programs contained within. The main diagram is broken up into four figures as shown in Figure 10.1. The "get data" subprogram is also shown to illustrate how the data is decoded from, and encoded to the serial connection.

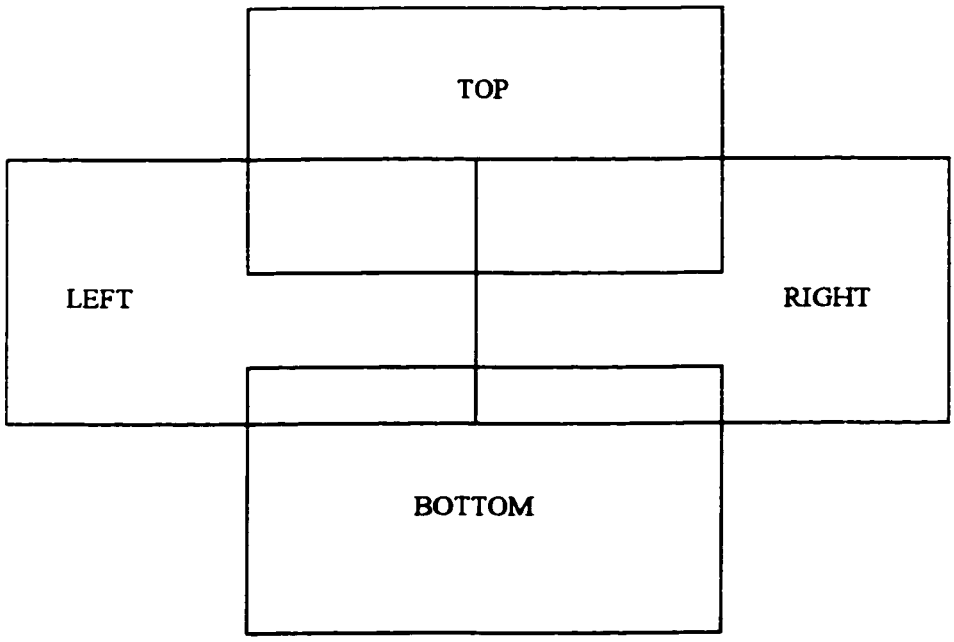

Figure 10.1 Labview wiring diagram layout

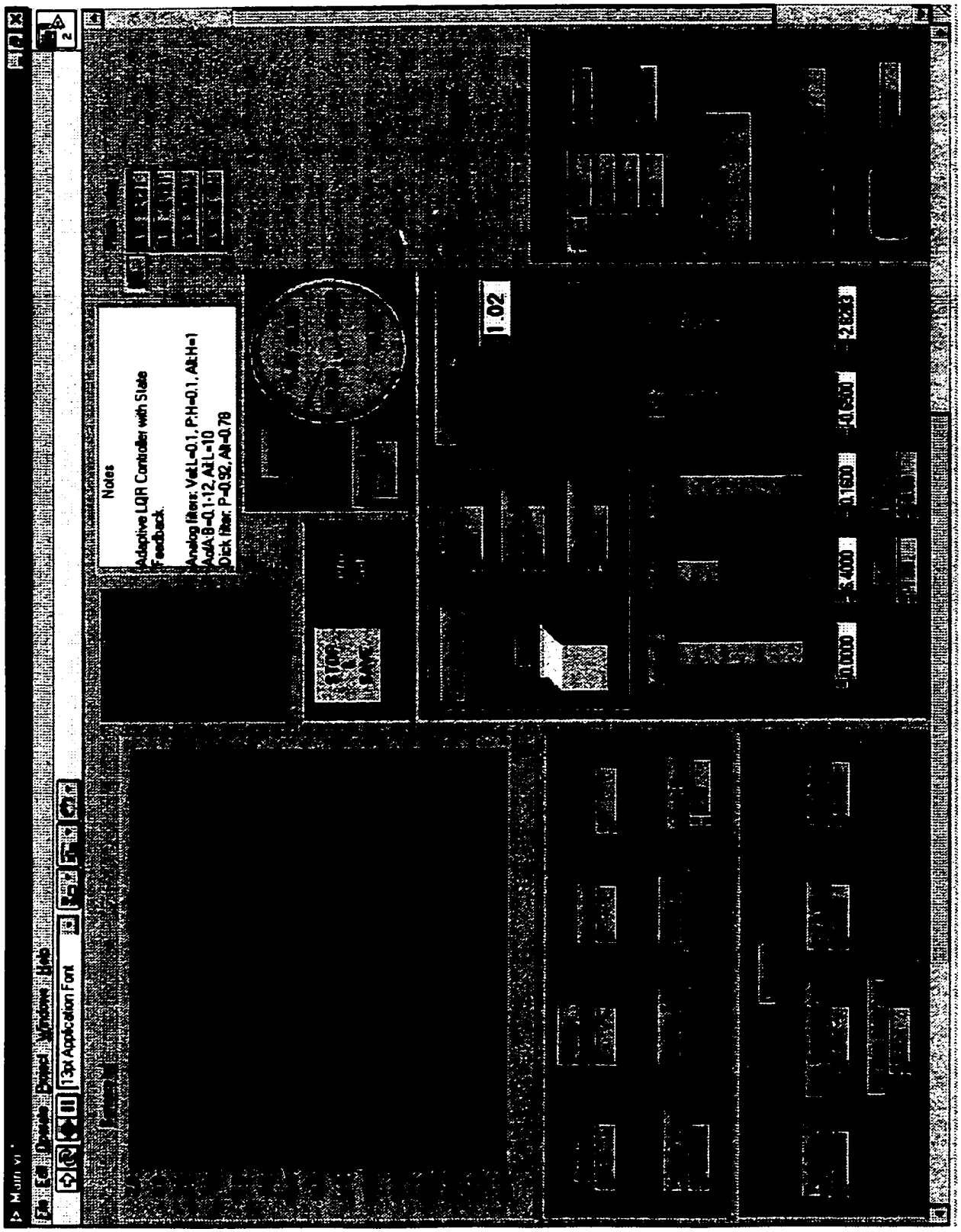

Figure 10.2 Labview front panel

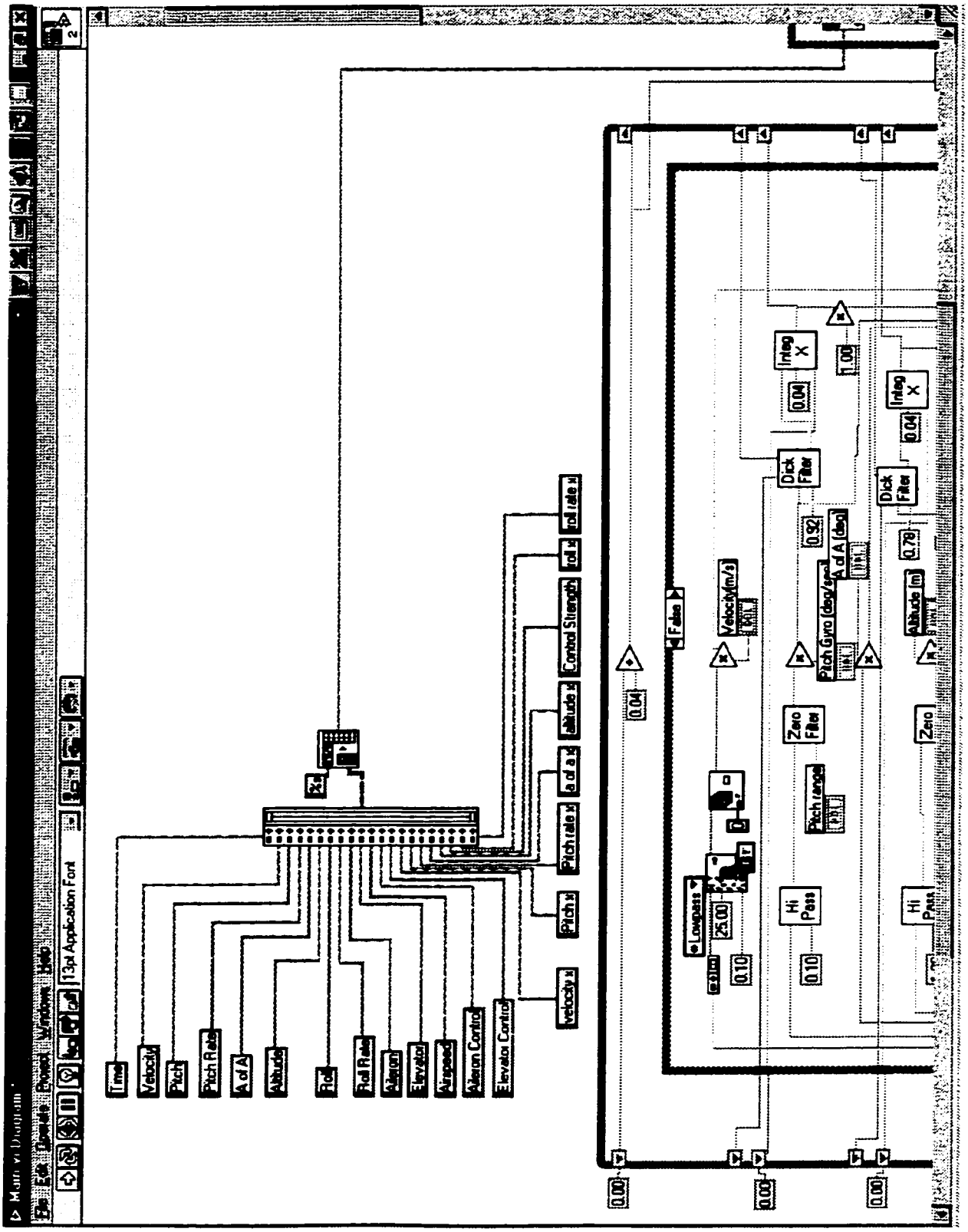

Figure 10.3 Main program wiring diagram (top)

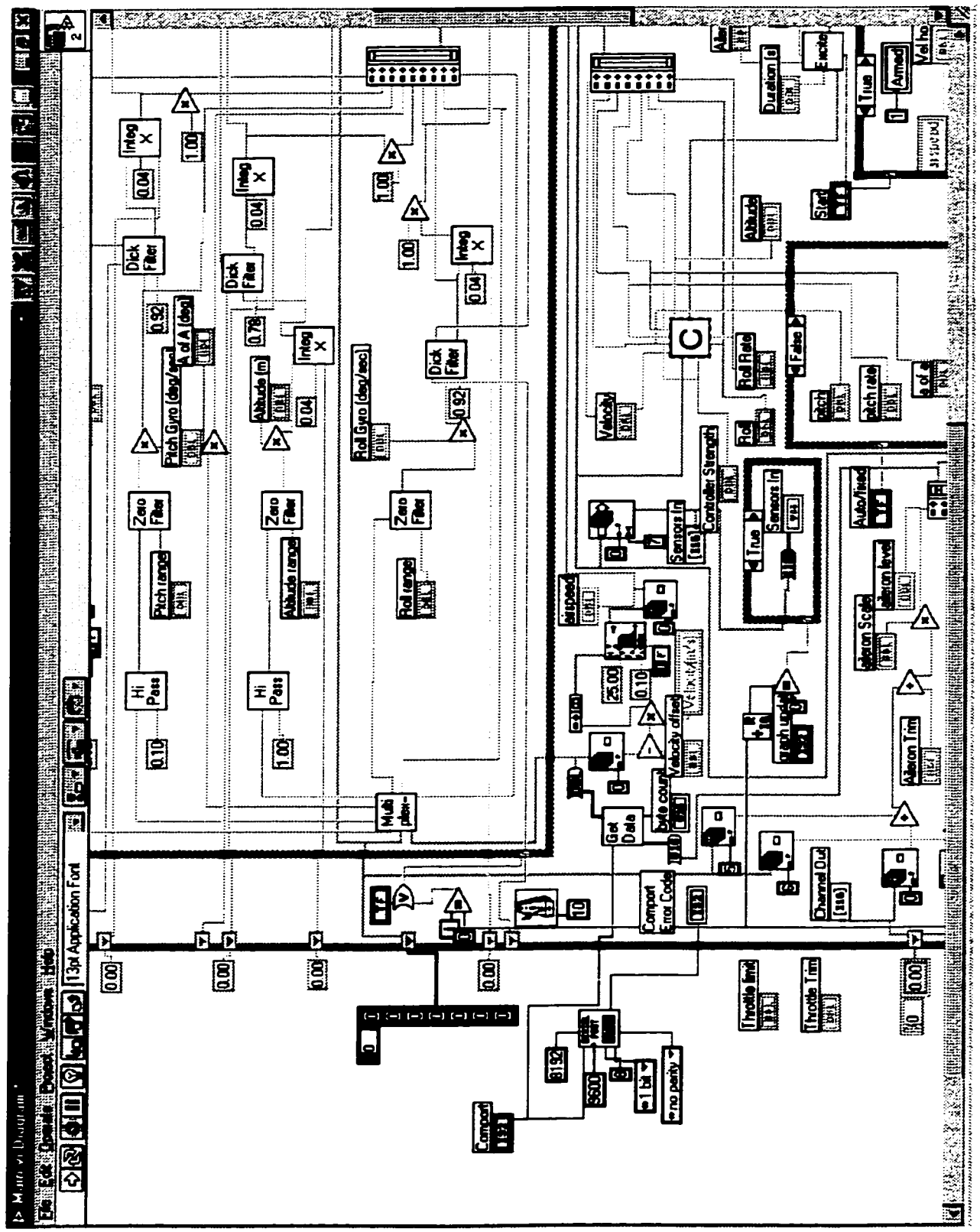

Figure 10.4 Main program wiring diagram (left)

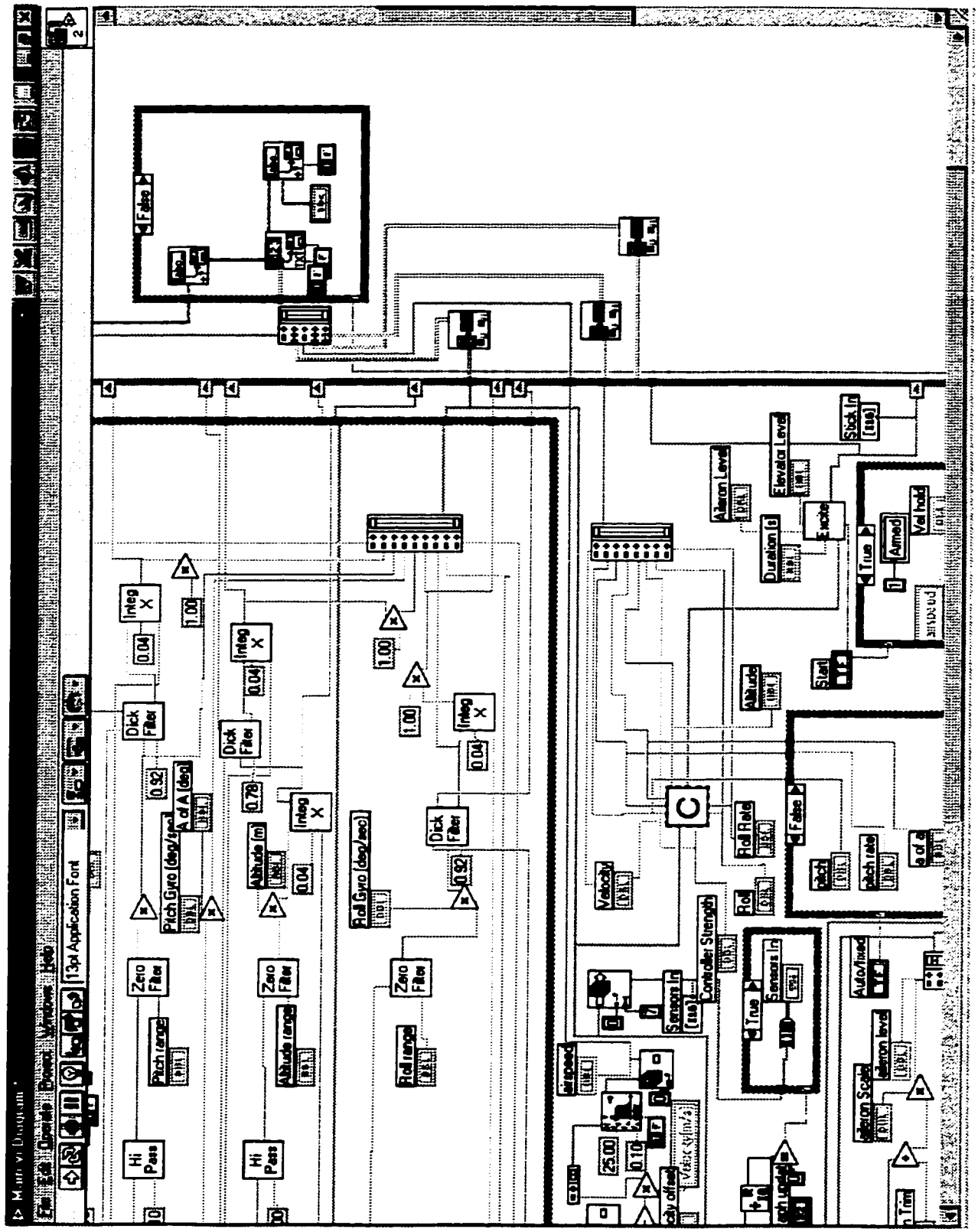

Figure 10.5 Main program wiring diagram (right)

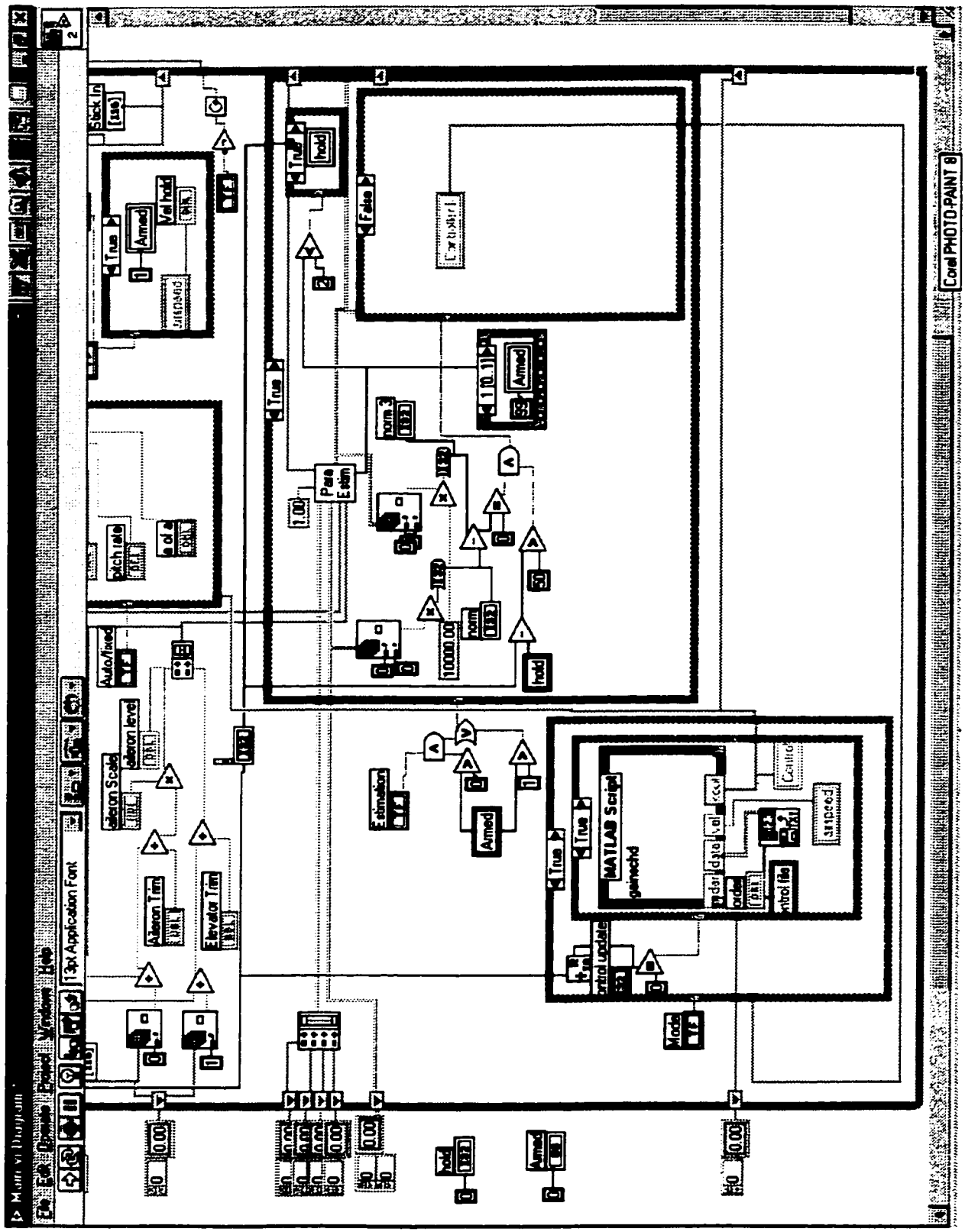

Figure 10.6 Main program wiring diagram (bottom)

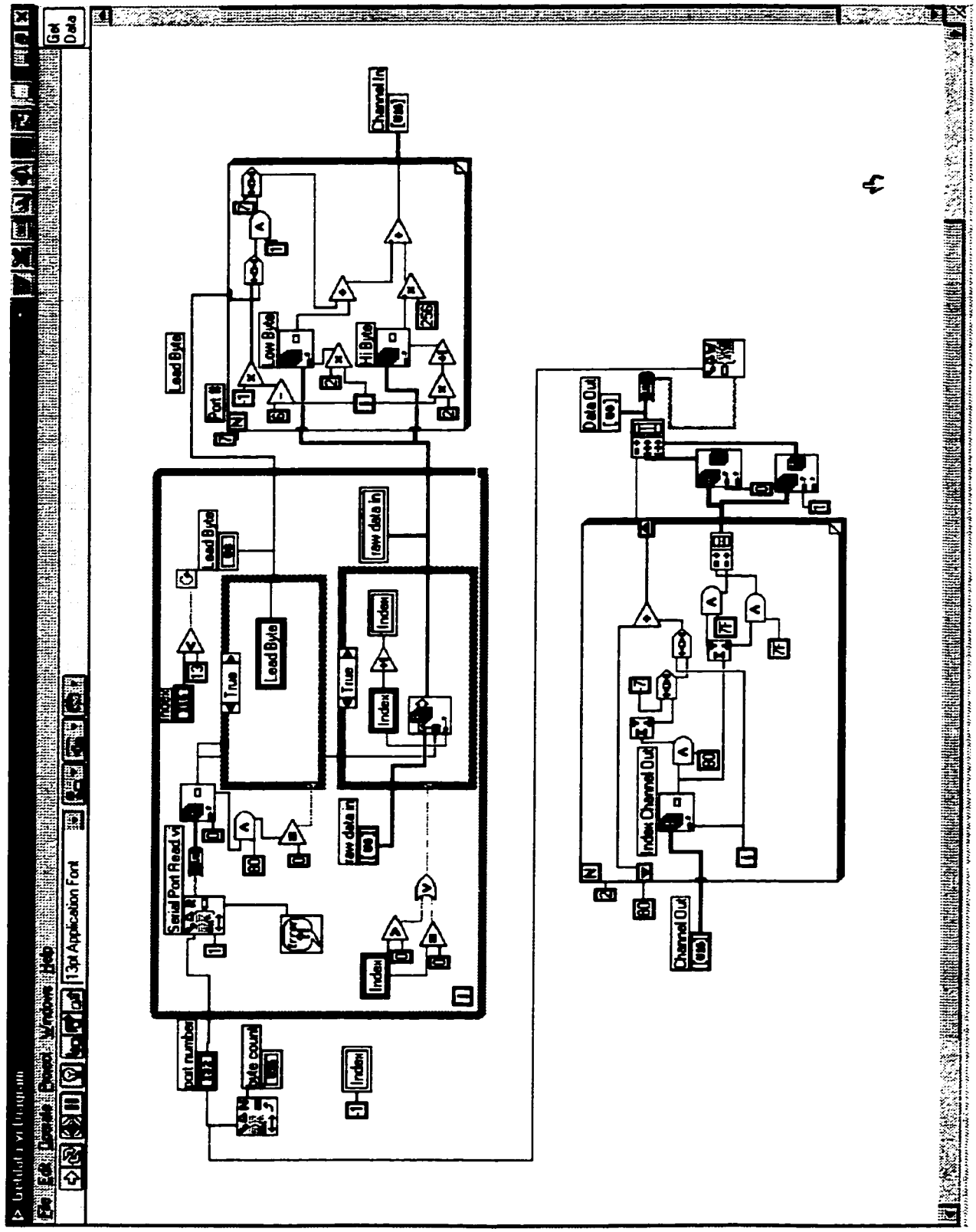

Figure 10.7 Getdata sub-program